UNIVERSIDADE FEDERAL DE MINAS GERAIS

SCHOOL OF ENGINEERING

GRADUATE PROGRAM IN CHEMICAL ENGINEERING

DOCTORAL THESIS

Author: Renata Braga Soares

Advisor (UFMG): Profª. Drª. Vanessa De Freitas Cunha Lins

Co-advisor (Texas A & M): Profª. Drª. Hong Liang

Corrosion and tribocorrosion resistance of supermartensitic stainless steels used in petroleum and gas industry

Belo Horizonte

Aug/2016

UNIVERSIDADE FEDERAL DE MINAS GERAIS

ESCOLA DE ENGENHARIA

PROGRAMA DE PÓS-GRADUAÇÃO EM ENGENHARIA QUÍMICA

Renata Braga Soares

Resistência à corrosão e à tribocorrosão de aços inoxidáveis
supermartensíticos utilizados na indústria de petróleo e gás

Tese de doutorado apresentada ao Programa de Pós-Graduação em
Engenharia Química da Universidade Federal de Minas Gerais

Linha de pesquisa: Corrosão e Engenharia de Superfície

Orientadora (UFMG): Profª. Drª. Vanessa De Freitas Cunha Lins
Co-orientador (Texas A & M): Profª. Drª. Hong Liang

Belo Horizonte

Aug/2016.

"CORROSION AND TRIBOCORROSION RESISTANCE OF SUPERMARTENSITIC STAINLESS STEELS USED IN PETROLEUM AND GAS INDUSTRY"
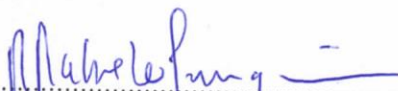
Renata Braga Soares

Tese submetida à Banca Examinadora designada pelo Colegiado do Programa de Pós-Graduação em Engenharia Química da Escola de Engenharia da Universidade Federal de Minas Gerais, como parte dos requisitos à obtenção do título de **DOUTORA EM ENGENHARIA QUÍMICA**.

24ª TESE APROVADA EM 26 DE AGOSTO DE 2016 POR:

Prof. Dr. Luís Frederico Pinheiro Dick
UFRGS

Pesquisadora Dra. Marília Mendonça de Lima
Vallourec

Pesquisador Dr. Wagner Reis da Costa Campos
CDTN

Profa. Dra. Rosa Maria Rabelo Junqueira
UFMG

Profa. Dra. Vanessa de Freitas Cunha Lins
Orientadora - DEQ/UFMG

"Talvez não tenha conseguido fazer o melhor, mas lutei para que o melhor fosse feito. Não sou o que deveria ser, mas Graças a Deus, não sou o que era antes".
(Marthin Luther King)

SUMMARY

PAPER 3: Electrochemical and electronic properties of passive film formed on supermartensitic stainless steel in a chloride medium

LIST OF TABLES

PAPER 3: Electrochemical and electronic properties of passive film formed on supermartensitic stainless steel in a chloride medium

ABSTRACT

Supermartensitic stainless steels have recently been introduced in the oil and gas industries to substitute more expensive duplex stainless steels for onshore and offshore tubing applications. This work aimed at evaluating the corrosion and tribocorrosion behavior of supermartensitic steels for application in oil and gas industry in aqueous media containing chlorides. The steel microstructure was characterized using optical microscopy (OM), scanning electron microscopy (SEM), energy dispersive spectroscopy (EDS), interferometry, X-ray diffraction (XRD), Mössbauer and electron backscattered diffraction (EBSD). The electrochemical characterization on steel surface supermatensitic stainless steel has been studied using potentiodynamic anodic polarization, cyclic potentiodynamic polarization, electrochemical impedance spectroscopy (EIS), Mott-Schottky and scanning vibrating electrode technique (SVET).

A tribocorrosion setup was configured in order to study the triboelectrochemical behavior of a supermartensitic steel. Wear analysis indicated that three-body abrasion was the dominant wear mechanism. Due to the synergetic effect of wear and corrosion, the concentration of pits was higher with rubbing but the pit propagation was inhibited. The smallest abrasive particles promoted the highest pit growth inhibition. The effect of larger diamond particles on tribocorrosion of supermartensitic steel would be less harmful than the effect of smaller abrasive particles. Coarse cuboidal TiN particles were identified on the steel surfaces of all samples. The TiN inclusions showed microvoids and a nucleous containing magnesium, aluminum and calcium oxides. Mössbauer analysis identified 0.7, 0.5 and 0.9% of retained austenite in SMSS samples as-quenched and tempered at 600°C and 640°C, respectively. The sample tempered at 600°C showed the lowest grain size, evaluated by using EBSD technique, and the

highest localized corrosion resistance in a saline medium. The SMSS sample tempered at 640^oC showed no electrochemical activity after 3600s of immersion in a saline solution by using a SVET technique, but after 86400s, a pit was detected. SVET analysis showed the association of a localized corrosion sites with the TiN inclusion on the steel surface. The 0.6 mol/L NaCl aqueous solution was the less aggressive electrolyte to the supermartensitic stainless steel (SMSS). The SMSS tempered at 600°C exhibited the highest corrosion resistance in two electrolytes. Furthermore, the capacitance study shows that the passive films formed on supermartensitic steel behave as p-type semiconductors below the flat band potential.

RESUMO

Os aços inoxidáveis supermartensíticos foram recentemente introduzidos nas indústrias de petróleo e gás para substituir os aços inoxidáveis duplex, mais caros, para aplicações em tubulações de instalações onshore e offshore. Este trabalho teve como objetivo avaliar o comportamento frente à corrosão e tribocorrosão de aços supermartensíticos para aplicação na indústria de petróleo e gás em soluções aquosas contendo cloretos. A microestrutura do aço foi caracterizada por microscopia óptica (MO), microscopia eletrônica de varredura (MEV), espectroscopia de energia dispersiva (EDS), interferometria, difração de difração de raios-X (DRX), Mössbauer e difração de elétrons retroespalhados (EBSD). A caracterização eletroquímica da superfície dos aços inoxidáveis supermatensiticos foi realizada usando polarização anódica potenciodinâmica, polarização potenciodinâmica cíclica, espectroscopia de impedância eletroquímica (EIS), análise de Mott-Schottky e a técnica do eletrodo vibratório de varredura (SVET).

Uma configuração para estudo da tribocorrosão foi projetada e construida de modo a estudar a resistência à tribocorrosão do aço supermartensítico. A análise indicou que o desgaste por abrasão a três corpos era o mecanismo de desgaste dominante. Devido ao efeito sinérgico do desgaste e da corrosão, a concentração de pites foi maior com o desgaste, mas a propagação de pites foi inibida. As partículas abrasivas de menor tamanho promoveram a inibição mais efetiva do crescimento de pites. O efeito de maiores partículas de diamante sobre o comportamento frente à tribocorrosão do aço supermartensítico foi menos nocivo do que o efeito de pequenas partículas abrasivas. Partículas cuboides grosseiras de carbonitreto de titânio foram identificadas nas superfícies de aço de todas as amostras. As inclusões de carbonitreto de titânio

apresentaram microvazios e um núcleo contendo óxidos de magnésio, de alumínio e de cálcio. A espectroscopia Mössbauer identificou 0,7, 0,5 e 0,9% de austenita retida, em amostras do aço austenitizado e temperado em água, e revenido a 600°C e 640°C, respectivamente. A amostra revenida a 600°C apresentou o menor tamanho de grão, avaliado através da técnica de EBSD, e a maior resistência à corrosão localizada em um meio salino. A amostra revenida a 640°C não revelou nenhuma atividade electroquímica após 3600s de imersão numa solução salina utilizando a técnica SVET, mas depois de 86400s, foram identificados pites na superfície do aço. A análise por SVET mostrou a associação dos locais de corrosão localizada com a inclusão de TiN na superfície do aço. A solução de 0,6 mol/L de cloreto de sódio foi o eletrólito menos agressivo ao aço inoxidável supermartensítico (SMSS). O aço revenido a 600°C exibiu a mais elevada resistência à corrosão nos dois eletrólitos estudados, de cloreto de sódio neutro e acetato e cloreto de sódio com pH ácido. Além disso, a análise de Mott Schottky mostrou que os filmes passivos formados no aço supermartensítico se comportaram como semicondutores do tipo p abaixo do potencial de banda plana.

ORGANIZATION OF THE WORK

This document is organized in:

Chapter 1 - Introduction;

Chapter 2 - Objectives;

Chapter 3 – Corrosion;

Chapter 4 – Tribocorrosion;

Chapter 5 - Materials and Methods, Results and Discussion. This chapter presents

the materials and methods, results and discussion in the scientific paper format.

Chapter 6 - Final Considerations and Suggestions for future studies.

CHAPTER 1 - Introduction

Introduction

The supermartensitic stainless steels have been widely used in the oil and gas industry due to their good mechanical properties, good weldability and corrosion resistance acceptable in environments containing chlorides, CO_2 and H_2S [1, 2]. Thus supermartensitic steels have increasingly replaced the duplex stainless steel that has a high cost of production in many onshore and offshore applications. In the oil and gas industry supermatensitic steels have been used primarily in the manufacture of seamless steel pipe for use in drilling oil and gas [3-6].

Compared to conventional martensitic stainless steels, the supermartensitic steel contains up to 3% (wt.) more in molybdenum (Mo) and up to 6% (wt.) more of nickel (Ni). Molybdenum is added to improve corrosion resistance of steel, while Ni is added to stabilize austenite (γ) at elevated temperatures while avoiding the formation of δ-ferrite. Levels of carbon (C) reduced to 0.01% (w/w) contribute to improve the weldability [3]. Heat treatments are often used to provide higher values of tensile strength and hardness of martensitic steels, and it also modifies the retained austenite content in their final microstructure [7, 8].

Corrosion is usually a spontaneous process and is responsible for the degradation of metals and alloys, causing them to lose their properties and generating huge financial or personal damage. The problems associated with corrosion are common and occur in various industries such as chemical, oil, petrochemical, shipbuilding, construction, etc. [9]. In this context, it is noted the great importance of the study of mechanisms to mitigate corrosion, especially in engineering.

In many situations, stainless steel can be subjected to the combined actions of corrosion and wear, such as in offshore, mining, biomedical, and food processing applications, where the stainless steel are subjected to abrasion, scratching, erosion, and other forms of wear damaging in a corrosive environment. Being of great interest the understanding of the tribocorrosion or corrosive-wear behavior of materials under combined chemical, electrochemical and mechanical actions [9].

Literature on the corrosion of supermartensitic steel is still scarce and addresses topics such as analysis of corrosion of supermartensitic steel in aerated and CO_2-saturated synthetic seawater [10], evaluation of susceptibility to intergranular corrosion in supermartensitic stainless steel weldments [11], and analysis of microelectrochemical corrosion of supermartensitic welds in chloride-containing media [12]. Study of the semiconducting properties of the passive layer of supermartensitic steels using the Mott-Schottky technique are reported in the literature [13]. This work aims to contribute to the study of the corrosion and tribocorrosion of supermartensitic steel mechanism using electrochemical and tribocorrosion tests.

References

[1] LIU, Yu-rong, YE, Dong, YONG, Qi-long, SU, Jie, ZHAO, Kun-yu, JIANG, Wen, Effect of Cu addition on microstructure and mechanical properties of 15%Cr super martensitic stainless steel, Mater. Des. 41 (2012) 16-22.

[2] ZOU, De-ningl, HAN, Ying, ZHANG, Wei, FANG, Xu-dong, Influence of Tempering Process on Mechanical Properties of 00Cr13Ni4Mo Supermartensitic Stainless Steel, J. Iron Steel Res. Int. 17 (2010) 50-54.

 [3] C.A. Della Rovere, C.R. Ribeiro, R. Silva, L.F.S. Baroni, N.G. Alcântara, S.E. Kuri, Microstructural and mechanical characterization of radial friction welded supermartensitic stainless steel joints, Mater. Sci. Eng. A 586 (2013) 86-92.

[4] X.P. Ma, L.J. Wang, C.M. Liu, S.V. Subramanian, Role of Nb in low interstitial 13Cr super martensitic stainless steel, Mater. Sci. Eng. A 528 (2011) 6812-6818.

[5] X.P. Ma, L.J. Wang, C.M. Liu, S.V. Subramanian, Microstructure and properties of 13Cr5Ni1Mo0.025Nb0.09V0.06N supermartensitic stainless steel, Mater. Sci. Eng. A 539 (2012) 271-279.

[6] C.A.D. Rodrigues, P.L.D. Lorenzo, A. Sokolowski, C.A. Barbosa, J.M.D.A. Rollo, Titanium and molybdenum content in supermartensitic stainless steel, Mater. Sci. Eng. A 460-461 (2007) 149-152.

[7] I. Calliari, M. Zanesco, M. Dabala, K. Brunelli, E. Ramous, Investigation of microstructure and properties of a Ni-Mo martensitic stainless steel, Mater. Des. 29 (2008) 246-250.

[8] T.J. Mesquita, E. Chauveau, M. Mantel, N. Bouvier, D. Kosche, Corrosion and metallurgical investigation of two supermartensitic stainless steels for oil and gas environments, Corr. Sci. 81 (2014) 152-161.

[9] Y. Sun, V. Rana, Tribocorrosion behaviour of AISI 304 stainless steel in 0.5 M NaCl solution, Mater. Chem. and Phys. 129 (2011) 138-147.

[10] N. Anselmo, J.E. May, N.A. Mariano, P.A.P. Nascente, S.E. Kuri, Corrosion behavior of supermartensitic stainless steel in aerated and CO_2-saturated synthetic seawater, Mater. Sci. Eng. A 428 (2006) 73-79.

[11] J.M. Aquino, C.A. Della Rovere, S.E. Kuri, Intergranular corrosion susceptibility in supermartensitic stainless steel weldments, Corr. Sci. 51 (2009) 2316-2323.

[12] M.D. Pereda, C.A. Gervasi, C.L. Llorente, P.D. Bilmes, Microelectrochemical corrosion study of super martensitic welds in chloride-containing media, Corr. Sci. 53 (2011) 3934-3941.

[13] HAN, Xiao-chen, LI, Jun, ZHAO, Kun-yu, ZHANG, We, SU, Jie, Effect of Chloride on Semiconducting Properties of Passive Films Formed on Supermartensitic Stainless Steel in $NaHCO_3$ Solution, J. Iron Steel Res. Int. 20 (2013) 74-79.

CHAPTER 2 - Objectives

Objectives

General objective

This work aimed at evaluating the corrosion and tribocorrosion behavior of supermartensitic steels for application in oil and gas industry in aqueous media containing chlorides.

Specific objectives

- To develop a novel in situ methodology to characterize surface under triboelectrochemical conditions.

- To study effects of hard particles and pitting on passivation to understand mechanisms of pitting and passivation under triboelectrochemical conditions.

- To determine the pitting potential of steel using the potentiodynamic anodic polarization.

- To determine the pitting potential and evaluate the repassivation ability using the technique of cyclic potentiodynamic polarization.

- To elucidate the mechanism of corrosion using the technique of electrochemical impedance spectroscopy (EIS).

- To evaluate the semiconducting properties of passive films by Mott-Schottky analysis.

- To determine the maps of the current density on surfaces of supermartensitic steels using scanning vibrating electrode technique (SVET).

- To perform characterization tests on steel surface before and after corrosion and tribocorrosion tests using optical microscopy (OM), scanning electron microscopy

(SEM), energy dispersive spectroscopy (EDS), interferometry, X-ray diffraction (XRD),

Mössbauer and electron backscattered diffraction (EBSD).

CHAPTER 3 - Corrosion

Corrosion

Supermartensitic stainless steel

Martensitic stainless steels have been increasingly applied in oil and gas application due to their good corrosion resistance and mechanical properties [1-2].

Stainless steels are alloys with at least 11 wt% chromium. At this Cr level, an adherent, self-healing chromium oxide can form on the steel surface in oxidizing environments. The stainless steels, besides Cr, also contain a host of other alloying elements whose presence enhances specific properties. Mo is added for enhancing resistance against pitting and Ni for obtaining austenite, for instance. Three main types of microstructures exist in stainless steels, i.e., ferritic, austenitic and martensitic. These microstructures may be obtained by properly adjusting steel chemistry [3].

Compared to conventional martensitic stainless steels, the supermartensitic steel contains up to 3 wt% more in molybdenum and up to 6 wt% more in nickel [4]. The supermartensitic stainless steels have good mechanical properties, good weldability and corrosion resistance acceptable in environments containing chlorides, CO_2 and H_2S [5,6]. Thus, supermartensitic steels have increasingly replaced the duplex stainless steel that has a high cost of production in many onshore and offshore applications [2, 4, 7, 8].

Influence of the main alloying elements

Chromium is a ferrite stabilizer which has the property of being able to protect itself with a passive oxide film and to contribute this property to other metals with which it is

alloyed. Stainless steels owe therefore their corrosion resistance to chromium and a minimum of 10.5 wt% of this element is required to generate a thin, adherent, continuous oxide film on the surface of the alloy [9, 10].

Low carbon stainless steels have either a ferritic or martensitic, possibly semi-ferritic, microstructure depending on composition. When the chromium content is below 12 wt% it is possible to obtain a martensitic microstructure since the steel can be made fully austenitic at elevated temperatures. A chromium content greater than 14 wt% gives a completely ferritic stainless steel over the whole temperature range corresponding to the solid state and hence cannot be hardened on quenching [9, 10].

The addition of molybdenum reduces the general corrosion rate, improves the resistance to localized corrosion at elevated temperatures and also reduces sulfide stress-corrosion cracking susceptibility. The molybdenum stabilizes the passive layer, with the formation of molybdates. However, being a strong ferrite stabilizing element, it must be balanced by the addition of austenite stabilizing elements such as carbon, nitrogen or nickel to maintain the completely martensitic microstructure in the presence of molybdenum [9, 10].

Manganese is added to substitute the nickel which has a very high cost and is also an austenite former element. When present in steels with a low carbon content can combine with oxygen to form manganese oxide avoiding formation of processing bubbles. However, its concentration may not exceed 2% (wt.) as in the presence of sulfur form inclusions and increasing its content, the ductility tends to decrease [9, 10].

Silicon is a strong ferrite former, essential as a deoxidizer during refining of the steel [9, 10]. Sulphur is generally kept at low levels as it can form sulfide inclusions. It reduces corrosion resistance, ductility, and fabrication properties, such as weldability and formability [9, 10].

The phosphorus dissolves in the ferrite which becomes harder with a lager grain size, causing cold fragilization. It also has the characteristic of improving the machinability of steels with a lower carbon content [9,10].

Martensite is the desired predominant phase in martensitic stainless steels. Its presence is a consequence of the diffusion less transformation of austenite during cooling to room temperature. Due to the large strain associated with the martensitic transformation, in order to better accommodate the shape deformation, the martensite tends to adopt a thin-plate shape. In alloys containing less than about 0.6 wt% C, the martensite form is laths which are aligned parallel to one another. The laths are grouped into larger structural entities, called blocks and packets (Fig. 1). The tetragonal strain caused by carbon trapped in the structure renders dislocation motion difficult and therefore martensite is harder than austenite. Martensite hardness increases with the carbon content, but with a low wt% C, supermartensitic stainless steel is relatively soft [9, 10].
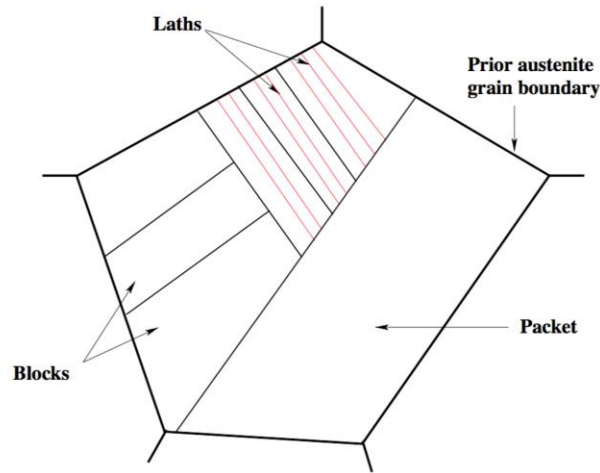
Fig. 1: Schematic illustration of the microstructural features of lath martensite (Adapted from [9]).

Austenite (Fig. 2) might be present in supermartensitic stainless steels as a result of two different processes. As mentioned before, the addition of substitutional elements depresses temperature, and, consequently, cooling from the austenitic field might lead to uncomplete martensitic transformation. On the other hand, austenite can be retained in the microstructure as a result of an intercritical annealing treatment i.e. carried out above the temperature of the onset of austenite formation on heating. In this case the stability of the reverted austenite is dependent upon the heat-treatment duration and temperature [9, 10]. This residual austenite is enriched in alloying elements due to the diffusional transformation, which strongly depresses martensitic transformation temperature and the austenite remain stable after cooling to room temperature [9, 10].
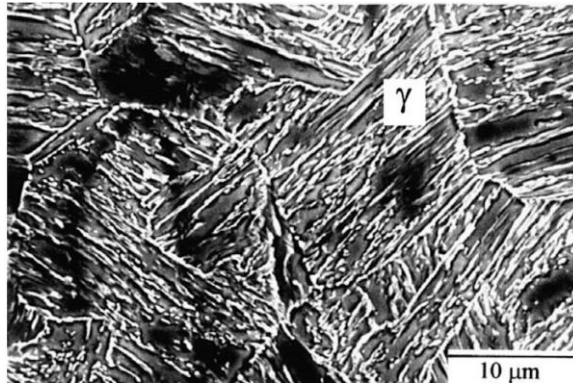
Fig. 2: Austenite particles (white particle-platelets) in a ferrite matrix (gray/black areas) for 13CrNiMo steels (Adapted from [11]).

Bilmes et al. [11] reported that the retained austenite which results from the applied heat treatments has a beneficial effect on the pitting corrosion resistance of 13CrNiMo stainless steels. According to Carrouge [9] in titanium free supermartensitic alloys containing 0.02 wt% C, the retention of austenite formed during intercritical annealing is beneficial to corrosion resistance. This is attributed to the dissolution of chromium and molybdenum carbonitrides in the favor of austenite formation. Since there is no chromium and molybdenum loss in the matrix the corrosion resistance is improved. Similarly, sulfide stress-corrosion cracking improvements were reported in a titanium stabilized supermartensitic steel containing austenite. It is believed that austenite absorbs hydrogen from martensite and thus contributes to lower its concentration [9].

The presence of δ-ferrite in the microstructure of martensitic stainless steels is undesirable. The effect that δ-ferrite has on the sulfide stress cracking resistance of tempered unstabilised supermartensitic stainless steel parent materials was recently studied. Cracking occurs at the δ-ferrite/martensite interface due to the chromium depletion associated with the precipitation of chromium carbonitrides during tempering [9].

Corrosion

Corrosion occurring by an electrochemical mechanism is the simultaneous transfer of mass and charge across a metal/solution interface, that usually occurs not by direct chemical reaction of a metal with its environment but rather through the operation of coupled electrochemical half-cell reactions (oxidation and reduction reactions) [12].

- Anodic Reactions

The loss of metal occurs as an anodic reaction. An example of an anodic reaction is the oxidation of iron (Eq. 1).

$$Fe_{(s)} \rightarrow Fe^{2+}{}_{(aq)} + 2e^{-} \tag{1}$$

In the anodic reaction occurs an increase in the oxidation number of the species that oxidizes and there a loss of electrons at the anodic site (electrons are produced by the reaction) [12].

- Cathodic Reactions

In the cathodic reaction there is a decrease in its oxidation number. There is a gain of electrons at the cathodic site (electrons are consumed by the reaction). An example of a cathodic reaction is the reduction of hydrogen ions to form hydrogen gas, which occurs predominant cathodic reaction in acidic solutions (Eq. 2).

$$2H^+{}_{(aq)} + 2e^- \rightarrow H_{2\,(g)} \qquad\qquad (2)$$
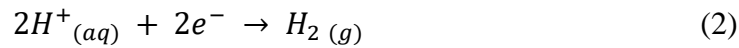
Another common cathodic reaction is the reduction of dissolved oxygen to hydroxyl ions, which occurs in neutral or basic aerated solutions (Eq. 3)

$$O_{2(g)} + 2H_2O + 4e^- \rightarrow 4OH^-{}_{(aq)} \qquad\qquad (3)$$
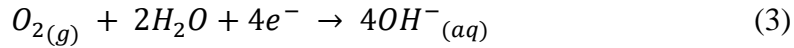
On a corroding metal surface, anodic and cathodic reactions occur in a coupled manner at different places on the metal surface. Some conditions are necessary for corrosion to occur, these are an anodic reaction, a cathodic reaction, a conductive path of contact between anodic and cathodic sites and the presence of an electrolyte. The most common electrolyte is the water containing dissolved ions [12].

Pitting corrosion

Pitting corrosion is a type of localized corrosion. In pitting corrosion, the metal is attacked at certain sites on the metal surface where the otherwise protective oxide film breaks down locally, usually due to the action of chloride ions [12].

On the steel surface submitted to a corrosion mechanism, pits were nucleated and propagated according to an autocatalytic mechanism that produces conditions for continued pit´s growth.

One mechanism of pit initiation is the penetration mechanism, where chlorides are transported through the oxide film to the metal surface and a localized dissolution of metal occurred. McCafferty and MacDonald [12, 13] have developed a point defect model (Fig. 3) for the breakdown of passivity. As the metal dissolution, cation

vacancies migrate from the oxide/electrolyte interface and accumulate at the metal/oxide interface, the resulting voids which form due to vacancy condensation lead to stresses within the oxide film and to pit nucleation [13]. In the film rupture mechanism, chloride ions penetrate the passive film through cracks in the oxide layer [13]. Chloride ions attack the passive film at localized points generating Fe^{2+} which attract chloride ions, producing $FeCl_2$:

$$Fe_{(s)} \rightarrow Fe^{2+}_{(aq)} + 2\bar{e} \qquad (4)$$

$$Fe^{2+}_{(aq)} + 2Cl^-_{(aq)} \rightarrow FeCl_{2(s)} \qquad (5)$$
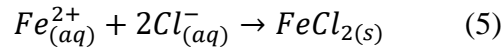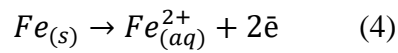
Accumulated metal cations and the iron chloride undergo hydrolysis, and a local acidity develops within the pit, accelerating the attack to steel [13]:

$$FeCl_{2(s)} + 2H_2O_{(l)} \rightarrow Fe(OH)_{2(aq)} + 2H^+_{(aq)} + 2Cl^-_{(aq)} \qquad (6)$$

$$Fe_{(s)} + HCl_{(aq)} \rightarrow FeCl_{2(aq)} + H_{2(g)} \qquad (7)$$
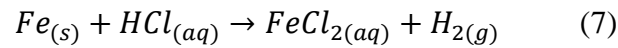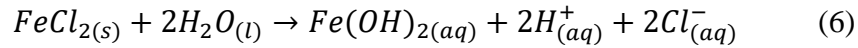
The Fig. 3 shows the various stages in pit nucleation, according to the model proposed by MacDonald [13].
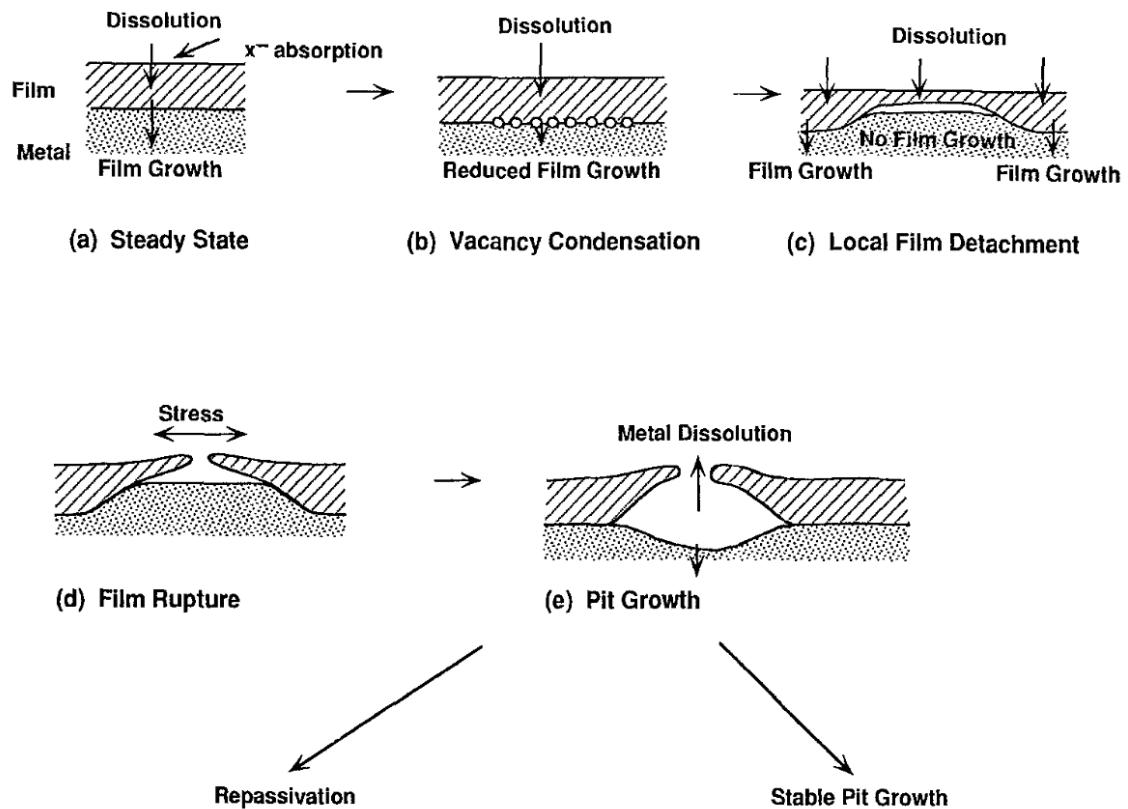
Fig. 3: Various stages of pit nucleation according to the point defect model for the breakdown of passivity (Adapted from [13]).

References

[1] LI, C.X.; BELL, T. "Corrosion properties of plasma nitrided AISI 410 martensitic stainless steel in 3.5% NaCl and 1% HCl aqueous solutions". Corr. Sci., 48 (2006) 2036-2049.

[2] T.J. Mesquita, E. Chauveau, M. Mantel, N. Bouvier, D. Kosche, Corrosion and metallurgical investigation of stainless steels for oil and gas environments, Corr. Sci. 81 (2014) 152-161.

[3] K.H. Lo, C.H. Shek, L J.K. L.Lai, Recent developments in stainless steels, Mater. Sci. and Eng. R, 65 (2009) 39-104.

[4] C.A.D. Rodrigues, P.L.D. Lorenzo, A. Sokolowski, C.A. Barbosa, J.M.D.A. Rollo, Titanium and molybdenum content in supermartensitic stainless steel, Mater. Sci. Eng. A 460-461 (2007) 149-152.

[5] X.P. Ma, L.J. Wang, C.M. Liu, S.V. Subramanian, Role of Nb in low interstitial 13Cr super martensitic stainless steel, Mater. Sci. Eng. A 528 (2011) 6812-6818.

[6] X.P. Ma, L.J. Wang, C.M. Liu, S.V. Subramanian, Microstructure and properties of 13Cr5Ni1Mo0.025Nb0.09V0.06N supermartensitic stainless steel, Mater. Sci. Eng. A 539 (2012) 271-279.

[7] I. Calliari, M. Zanesco, M. Dabala, K. Brunelli, E. Ramous, Investigation of microstructure and properties of a Ni-Mo martensitic stainless steel, Mater. Des. 29 (2008) 246-250.

[8] Y. Sun, V. Rana, Tribocorrosion behaviour of AISI 304 stainless steel in 0.5 M NaCl solution, Mater. Chem. and Phys. 129 (2011) 138-147.

[9] D. Carrouge, Transformations in Supermartensitic Stainless Steels, Thesis (PHD), Department of Materials Science and Metallurgy, University of Cambridge, 2002.

[10] George E. Totten, Steel Heat Treatment Handbook: Metallurgy and Technologies, 2th Ed. Editedby, CRC Press, 2007.

[11] P. D. Bilmes, C. L. Llorente, C.M. Méndez, C.A. Gervasi, Microstructure, Heat Treatement and Pitting Corrosion of 13CrNiMo Plate and Weld Metals, Corr. Sci. 51 (2009) 876-881.

[12] E. McCafferty, Introduction to Corrosion Science, Springer: New York, 2010.

[13] D.D. MacDonald, The Point Defect Model for the Passive State, Journal of Electrochemical Society, 139 (1992) 3434-3449.

CHAPTER 4 - Tribocorrosion

Tribocorrosion

Tribocorrosion is a multidisciplinary research area that has played important roles in many applications due to its practical and economical relevance. A metallic material submitted to a tribocorrosion condition undergoes simultaneous physico-chemical and mechanical surface interactions in a tribological contact resulting in an irreversible degradation [1, 2].

In passive materials, the origin of tribocorrosion is closely related to the presence of a protective oxide film on material surfaces [1, 3-8]. The tribocorrosion behaviour of passive materials such as stainless steels has been studied by Ponthiaux et al. [3], Ben Saada et al. [4], López et al. [5], Jun Chen et al. [6]. It is well known that these passive materials form a protective layer, which is mostly composed by oxides as a consequence of a spontaneous reaction when immersed in aqueous solutions [1, 3-8].

Two main mechanisms contribute to material removal from the surface of the material under tribocorrosion conditions: wear accelerated corrosion and mechanical removal from the sliding contact [7, 8]. Materials degradation may occur under a variety of conditions. Two body or three body contacts between sliding surfaces are a common cause of tribocorrosion [2, 9-16].

In many situations, stainless steel can be subjected to the combined actions of corrosion and wear, such as in offshore, mining, biomedical, and food processing applications, where the stainless steels are subjected to abrasion, scratching, erosion, and other forms of wear damaging in a corrosive environment. It is of great interest the understanding of

the tribocorrosion or corrosive-wear behavior of materials under combined chemical, electrochemical and mechanical actions [17].

Researchers have developed various tribocorrosion setup based on the specific objectives of their study. The tribological systems consisting of mechanical devices containing metallic parts that are in contact with counterparts and exhibiting a relative movement in a corrosive environment. The selection of a setup for a specific study will depend of the contact conditions and mechanical parameters in relation to applications [3, 18-23]. One of the challenges in tribocorrosion research is the lack of standard test systems. A standard tribocorrosion setup would be helpful in improving yield reliable results.

Wear mechanisms

According to DIN 50320 [24] four basic wear mechanisms or any combination of them are involved in the wear processes: adhesion, abrasion, fatigue and tribochemical (Fig. 1).
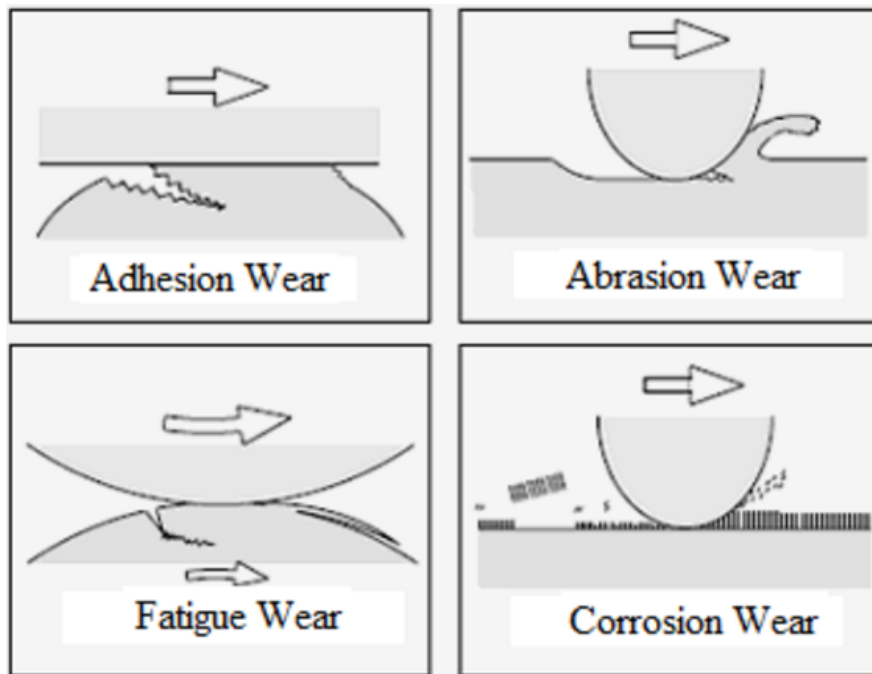
Fig. 1: Schematic figures of four types of wear [25].

Adhesive wear

Adhesive wear occurs when the adhesive bond between the surfaces is strong enough to resist sliding. As a result of high pressure subsequent reaction between the contact surfaces, adhesion is formed of a localized junction due to plastic deformation caused by dislocation movement and of the sliding surfaces [26]. The relative sliding between the contact surfaces causes the rupture of these joints often by crack growth and material transfer from one surface to another [27].

Abrasive wear

In abrasive wear, material is removed or displaced from a surface by hard particles, or sometimes by hard protuberances on a counterface, forced against and sliding along the surface. Several qualifying terms can be used in describing abrasion. A distinction is

often made between two-body abrasive wear, illustrated in Fig. 2 (a), and three-body abrasive wear, shown in Fig. 2 (b). Two-body wear is caused by hard protuberances on the counterface, while in three-body wear hard particles are free to roll and slide between two, perhaps dissimilar, sliding surfaces [26].

(a) Two-body abrasion

(b) Three-body abrasion
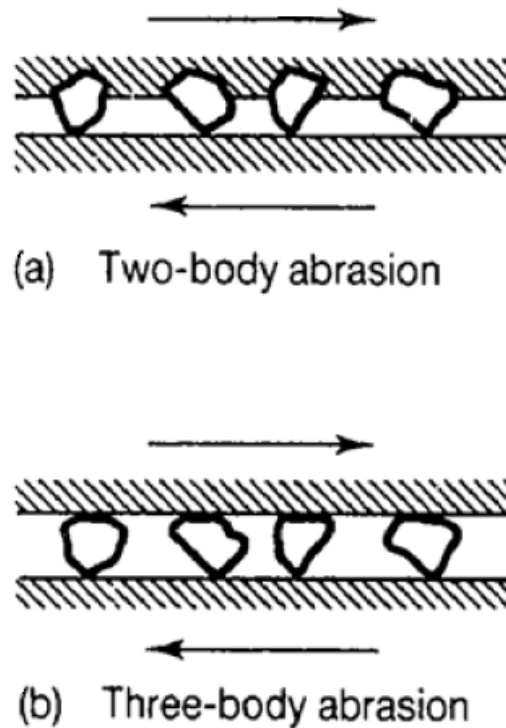
Fig. 2: Illustration of the differences between (a) two-body abrasion and three-body abrasion [26].

Fatigue wear

Fatigue wear can be characterized by crack formation and flaking of material caused by repeated alternating loading of solid surfaces. The rolling and/or sliding contact of solids or impacting contact of solids and/or liquids can result in cyclic surface stressing [28].

Tribochemical wear

Tribochemical wear can be characterized by rubbing contact between two solid surfaces that react with the environment. The corrosive environment may be gaseous or liquid. The wear process proceeds by continual removal and new formation of reaction layers on the contacting surfaces. In the presence of atmospheric oxygen, worn debris consist largely of oxides which have formed upon the surfaces and been removed by rubbing [28].

References

[1] M.T. Mathew, T. Uth, N.J. Hallab, R. Pourzal, A. Fischer, M.A. Wimmer, Construction of a tribocorrosion test apparatus for the hip joint: Validation, test methodology and analysis, Wear 271 (2011) 2651-2659.

[2] D. Landolt, S. Mischler, M. Stemp, Electrochemical methods in tribocorrosion: a critical appraisal, Electrochim. Acta 46 (2001) 3913-3929.

[3] P. Ponthiaux, F. Wenger, J.-P Celis. Tribocorrosion: Material Behavior Under Combined Conditions of Corrosion and Mechanical Loading, Corrosion Resistance, InTech, 2012.

[4] F. Ben Saada, Z. Antar, K. Elleuch, P. Ponthiaux, On the tribocorrosion behavior of 304 L stainless steel in olive pomace/tap water filtrate, Wear 328 (2015), 509-517.

[5] A. López, R. Bayón, F. Pagano, A. Igartua, A. Arredondo, J.L. Arana, J.J. González, Tribocorrosion behaviour of mooring high strength low alloy steels in synthetic seawater, Wear 338-339 (2015) 1-10.

[6] Jun Chen, Qing Zhang, Quan-an Li, San-ling Fu, Jian-zhang Wang, Corrosion and

tribocorrosion behaviors of AISI 316 stainless steel and Ti6Al4V alloys in artificial seawater, Trans. Nonferrous Met. Soc. China 24 (2014) 1022-1031.

[7] Jun Chen, Feng-yuan Yan, Tribocorrosion behaviors of Ti–6Al–4V and Monel K500 alloys sliding against 316 stainless steel in artificial seawater, Trans. Nonferrous Met. Soc. China 22 (2012) 1356-1365.

[8] D. Landolt, S. Mischler, M. Stemp, S. Barril, Third body effects and material fluxes in tribocorrosion systems involving a sliding contact, Wear 256 (2004) 517-524.

[9] S.B. Joo and H. Liang, In Situ Characterization of Tribo-Electrochemical Effects on Topography of Patterned Copper Surfaces, J. Electronic Matls. 42 (2013) 979-987.

[10] S. Joo and H. Liang, Mechanisms of Step Height Reduction in Copper Chemical Mechanical Polishing (CMP), Microelectronic Engineering 98 (2012) 12-18.

[11] F. Gao and H. Liang, Effects of Potential and Mechanical Stimulation on Oxidation of Tantalum during Electrochemical-Mechanical Polishing, J. Elec. Matls. 41 (2012) 624-631.

[12] F. Gao and H. Liang, Transformable Oxidation of Tantalum in Electrochemical-Mechanical Polishing of Tantalum, J. Electro. Matls. 40 (2011) 134-140.

[13] K. Wang, Z. Liu, T. Cruz, M. Salmeron, and H. Liang, In Situ Spectroscopic Observation of Activation and Transformation of Tantalum Suboxides, J. Phys. Chem. A, A, 114 (2010) 2489–2497.

[14] F. Gao and H. Liang, Material Removal Mechanisms in Electrochemical-Mechanical Polishing of Tantalum, Electrochim. Acta 54 (2009) 6808-6815.

[15] F. Gao and H. Liang, In Situ Observation of Friction-Induced Electrochemical Reactions and Impedance in Tantalum-ECMP, J. Elecchem. Soc. 156 (2009) H80-H86.

[16] P. Kar, P. Asthana, and H. Liang, Formation and Characterization of Tribofilms, J. Tribo. 130 (2008) 04201-042306.

[17] Y. Sun, V. Rana, Tribocorrosion behaviour of AISI 304 stainless steel in 0.5 M NaCl solution. Mater. Chem. and Phys. 129 (2011) 138-147.

[18] P. Kar, K. Wang, and H. Liang, Force-Dominated Non-Equilibrium Oxidation Kinetics of Tantalum, Electrochim. Acta 53 (2008) 5084-5091.

[19] P. Kar, K. Wang, and H. Liang, Oxidation of Tantalum with Mechanical Force, Electrochem. & Solid-State Lett. 11 (2008) C13-C17.

[20]   F. Gao, S. Joo, and H. Liang, Ch. 4.2. Tribology and CMP and Case Studies on Tantalum in Tribocatalysis, Tribochemistry, and Tribocorrosion, Ed. K. Hiratsuka and C. Kajdas, Pan Stanford Publishing, 2015.

[21] S. Joo and H. Liang, Ch. 23, Tribology in Chemical-Mechanical Planarization, Tribology for Scientists and Engineers, Ed. P.L. Menezes, S. Ingole, M. Nosonovsky, S.V. Kailas, and M.R. Lovell, Springer Science+Business Media, NY, 2013.

[21] H. Liang, Chemical-Mechanical Polishing, ed. Q. Wang and YW Chang, Springer, 2012.

[22] M. Kulkarni, F. Gao, and H. Liang, Chemical-mechanical Polishing (CMP): a Controlled Tribocorrosion Process, Tribocorrosion of Passive Metals and Coatings, Edi. Dieter & Mischler, Woodhead Publishing, 2011.

[23] M. Kulkarni, F. Gao, and H. Liang, Ch. 18, Chemical Mechaical Polishing, Tribocorrosion of Passive Metals and Coatings, Ed. D. Landolt and S. Mischler, Woodhead Publishing, 2011.

[24] DIN 50320: Verschleiß-Begriffe, Systemanalyse Von Verschleißvorgängen, Gliederung des Verschleißgebietes; Benth Verlay, Berlin, 1979.

[25] K. Kato, K. Adachi, Ch. 22, Wear Mechanisms, Modern Tribology Handbook, Ed. CRC Press LLC, 2001.

[26] I. M. Hutchings, Tribology; Friction and wear of engineering materials. London: Edward Arnold, 1992.

[27] B. Bhushan, Modern Tribology handbook CRC Press LLC, Florida, 2001.

[28] K.H. Zum-Garh, Microstructure and wear of materials, Tribology Series, Elsevier, 1987.

CHAPTER 5 - Materials and Methods, Results and Discussion.

CHAPTER 5

PAPER 1: An in situ approach to study abrasion and passivation of a supermartensitic stainless steel
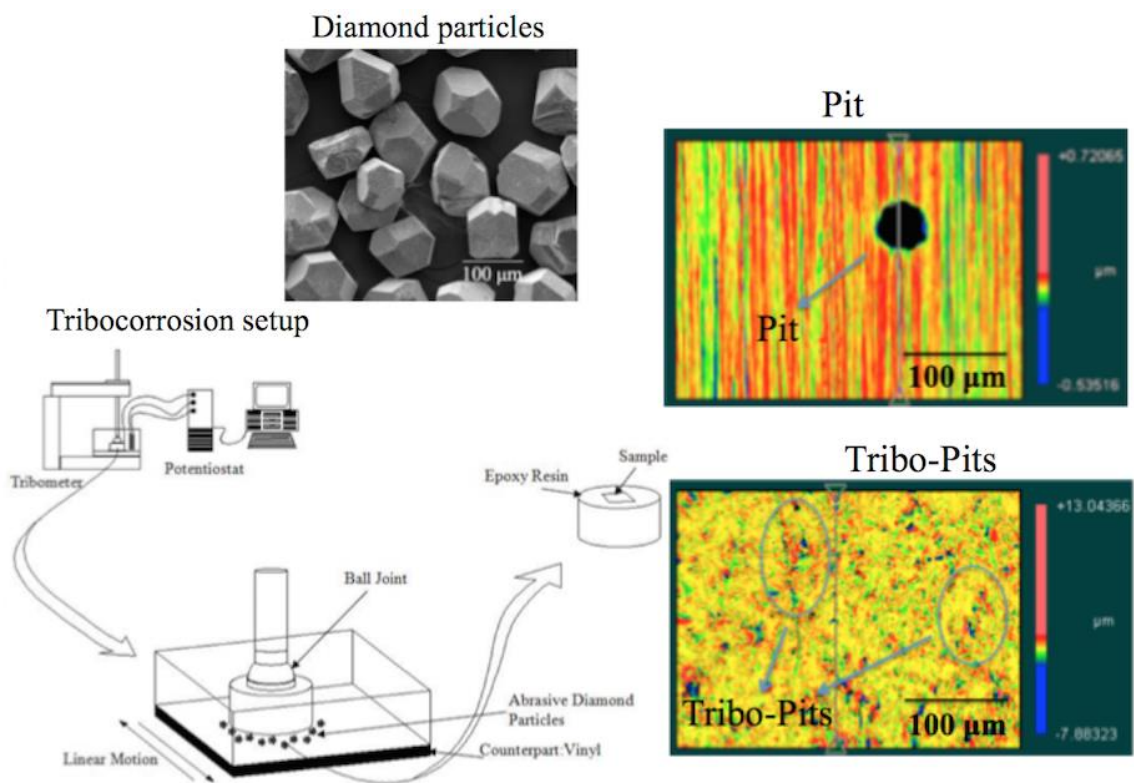
Abstract

We developed an in situ method to characterize metal surfaces in a triboelectrochemical process. A setup configured with a potentiostat and a tribometer was developed in order to analyze the synergistic interactions of corrosion and wear. This system is found to be effective in revealing the influence of mechanical abrasion on corrosion. A supermartensitic steel, commonly used in petroleum and gas industry, was studied. Wear analysis indicated that three-body abrasion was the dominant wear mechanism. Due to the synergetic effect of wear and corrosion, the concentration of pits was higher with rubbing but the pit propagation was inhibited. The smallest abrasive particles promoted the highest pit growth inhibition. The effect of larger diamond particles on tribocorrosion of supermartensitic steel would be less harmful than the effect of smaller abrasive particles.

Key-words: sliding wear; three-body abrasion; steel; diamond, ultra-hard materials; wear testing; corrosion-wear.

Introduction

Tribocorrosion plays important roles in many applications due to its practical and economical relevance. A metallic material exhibits irreversible degradation when submitted to a tribocorrosion condition, where mechanical and chemical interaction took place [1, 2, 3].

In passive materials, a protective oxide film is closely associated which the tribocorrosion phenomenon [1, 4-9]. Tribocorrosion of passive materials such as stainless steels has been studied by several researchers [4, 5, 6, 7]. It is well known that these passive materials form a protective layer, which is mostly composed by oxides or hydroxides as a consequence of a spontaneous reaction when immersed in aqueous solutions or exposed to an oxidant environment [1, 4-9]. The wear due to sliding contact and accelerated corrosion is the mechanism involved in tribocorrosion process [8, 9]. Material degradation may occur under a variety of conditions. Tribocorrosion can occur when three-body or two body contacts operate between sliding surfaces in a corrosive environment [2, 10-17].

Supermartensitic stainless steels have been widely used in the oil and gas industry due to their favorable mechanical properties, weldability and acceptable corrosion resistance in environments containing chlorides, CO_2 and H_2S [18, 19]. Thus, supermartensitic steels have increasingly replaced duplex stainless steels with a higher cost of production in many onshore and offshore applications. In the oil and gas industry, supermartensitic steels have been used primarily in the manufacture of seamless steel pipes for drilling oil and gas [20-23].

Stainless steels are submitted, in their industrial applications, to wear damage (erosion, abrasion, scratching) in a corrosive medium. It is of great interest in understanding the tribocorrosion or corrosive-wear of materials under combined chemical, electrochemical and mechanical actions [24]. It has been reported that about wear and tribocorrosion behavior of austenitic stainless steels [24, 25, 26, 27]. However, the tribocorrosive behavior of supermartensitic stainless steels is not well understood.

Researchers have developed various tribocorrosion setups according to their specific studies. In general, tribological setups exhibit metallic parts with a relative movement in a corrosive medium. The application conditions determine the selection of the tribocorrosion device [4, 28-34].

The objective of this work is to develop a tribocorrosion configuration to study the effect of mechanical abrasion on the corrosion of supermartensitic steels used in petroleum and gas industry. Subsequently, a brief review in existing tribocorrosion test systems used is provided. A potentiodynamic anodic polarization study was performed to evaluate the electrochemical behavior of supermartensitic steel in tribocorrosive processes. To the best of our knowledge, tribocorrosion behavior of supermartensitic steels has not been reported before.

Materials and Methods

A brief review in approaches in tribocorrosion

Most reported experiments on tribocorrosion integrate a tribometer and an electrochemical unit. Prior research has been reported on various specific objectives [35-38]. The application parameters determine the selection of the adequate setup [4]. Some setups used for tribocorrosion studies are listed in Table 1.

Table 1: Types of tribocorrosion test systems in literature.

Tribocorrosion system	Source	Interest of the study	Materials studied
Ball on plate	Azzi and Szpunar [35]	Biomedical	Ti and TiN
	Guadalupe Maldonado et al. [36]	Industrial application	Stellite alloy
	Martin et al. [37]	Industrial application	Ti_6Al_4V
	Naghibi et al. [38]	Biomedical	Ti/TiN PVD coating and 316L stainless
	López et al. [6]	Application in offshore industry	Low alloy steels
	Siva Rama Krishna et al. [39]	Industrial application: Oxide film	Rutile film
	García et al. [40]	Industrial application: Oxide film	AISI 316 stainless steel
Cylinder on bar	Pourzal and Fischer [41]	Biomedical	CoCrMo alloy
Microabrasion	Salasi et al. [42]	Industrial application	High-chromium cast irons
	Sharifi et al. [43]	Dental application	Y-TZP
	Stack et al. [44]	Biomedical	Mild steel
Pin on ball	Wimmer et al. [45]	Biomedical	CoCrMo alloy
Pin on disc	Oliveira et al. [46]	Dental application	TiO_2 anodic films
	Andrew Emge et al. [47]	Effect of sliding velocity	Copper
	Stack and Chi [48]	Effects of applied load and velocity	Steel and alumina
	Ribeiro et al. [49]	Biomedical	Boride coating
	Baxi et al. [50]	Biomedical	Alumina coatings
	Sun and Vipul Rana [24]	Industrial application	AISI 304 stainless steel
	Jemmely et al. [51]	Industrial application	Fe–17Cr stainless steel
	Stachowiak and Zwierzycki [52]	Industrial application	AISI304 steel
Ring on disk	Serre et al. [53]	Industrial application	Graphite and Ti alloy
Ring on block	Jun Chen and Feng-yuan Yan [8]	Industrial application: Behavior of passive metal	Ti–6Al–4V and monel K500 alloys
Rod on flat	Medvedovski et al. [54]	Industrial application	Boride-based coatings
Special type of set-up	Mathew et al. [1]	Biomedical	CoCrMo alloy
	Gant et al. [55]	Industrial application	WC–Co hard metals
	Barril et al. [56]	Biomedical	Ti_6Al_4V alloy
	Royhman et al. [57]	Biomedical	CoCrMo and Ti_6Al_4V alloy
	Sun et al. [58]	Biomedical	Cast CoCrMo alloy

The main advantage of using these tribometers is to control the tribological parameters

for the experiment, but synchronizing and the correlation of the corrosion and

tribological results are weakness aspects of this tribometers [1].

Materials

Measurements were performed on supermartensitic stainless steel samples with the chemical composition shown in Table 2. The supermartensitic steel was developed for applications in oil and gas industry. Its average hardness was 275.43±2.36 (HV 300 gf).

Table 2: Chemical composition of the supermartensitic stainless steel from SENAI-CETEF/Itaúna.

Element	C	Cr	Ni	Mo	Si	Mn	P	S	N	Al	Ti
Content (wt%)	<0.01	12.2	5.63	1.86	0.21	0.52	0.023	0.004	0.026	0.015	0.17

The microstructure of the supermartensitic stainless steel samples consists of martensite (Fig. 1).
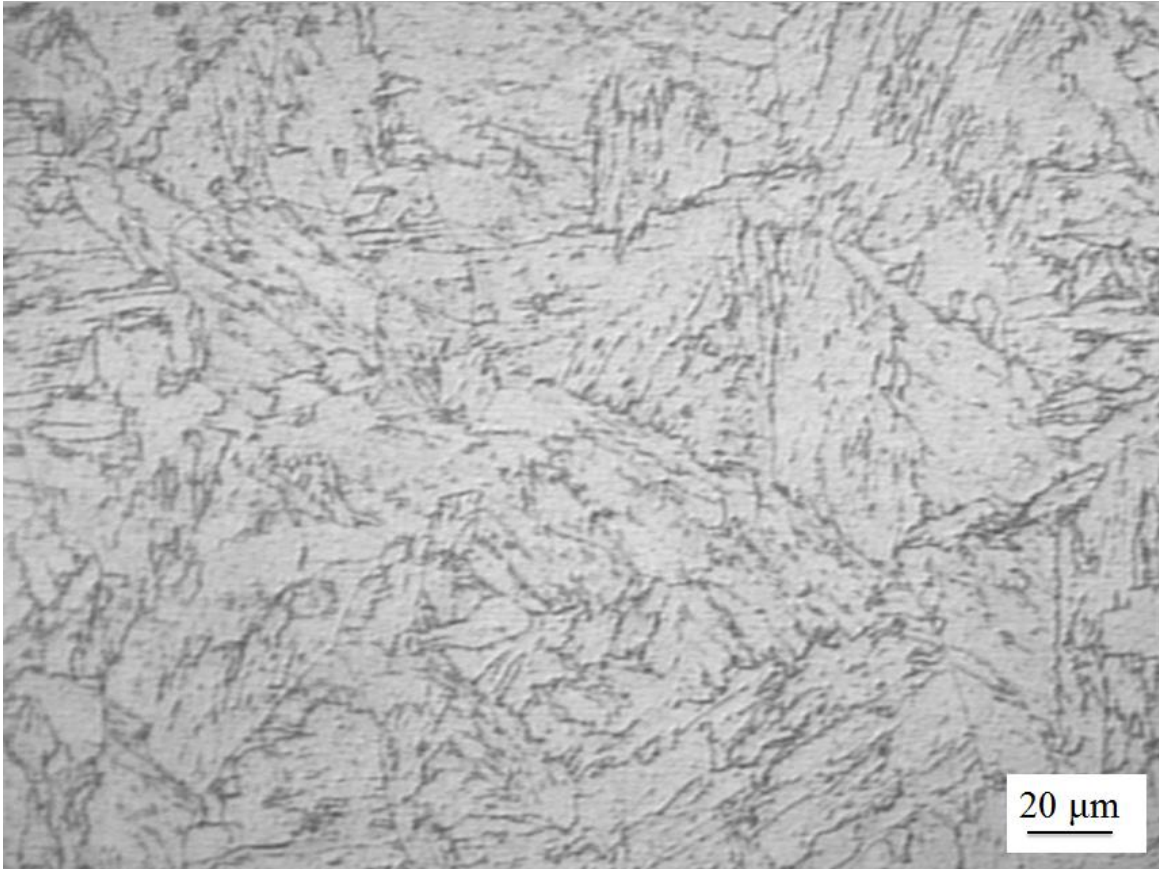
Fig. 1: Optical micrograph of the supermartensitic stainless steel microstructure.

For the tribocorrosion experiments, abrasive diamond particles of size range 10-20 µm, 30-40 µm, 40-60 µm, and 140–170 µm were used. To study the effect of hard particle size on passivation steel behavior, the same number of particles were used for each size particle. The morphology of the diamond particles is shown in Fig. 2.
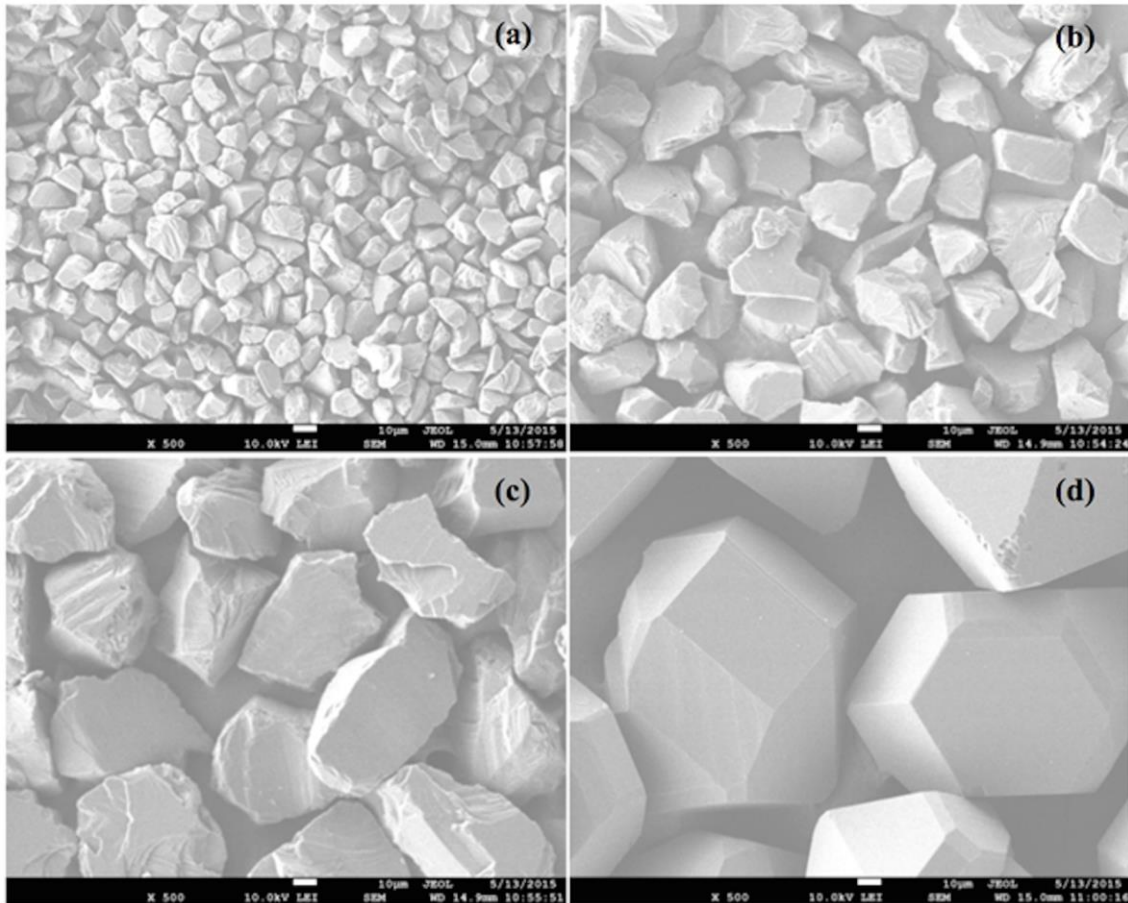
Fig. 2: Morphology of the diamond particles of size range (a) 10-20 μm,

(b) 30-40 μm, (c) 40-60 μm, (d) 140–170 μm.

Tribocorrosion setup

In this work, a novel in situ methodology to characterize surface under triboelectrochemical conditions was developed (Fig. 3).
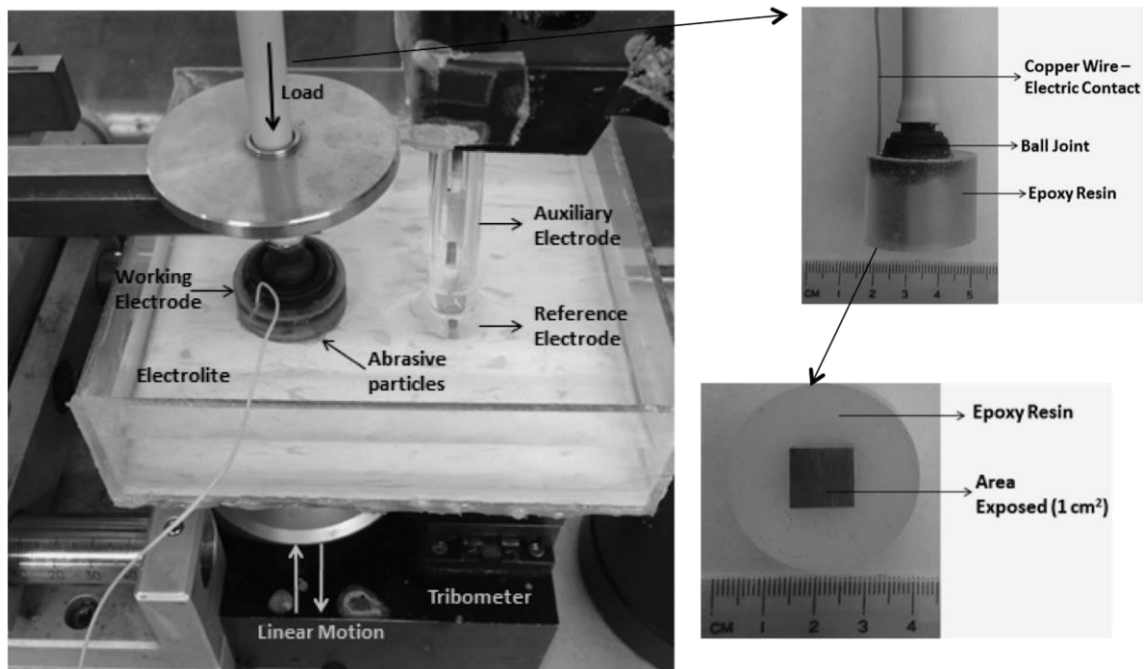
Fig. 3: Overview of the tribocorrosion setup.

The electrical contact was made possible by welding a copper wire directly on the sample. The steel samples were embedded in an epoxy resin and were polished using 180, 400, 800 and 1200 grit papers.

In this setup, a tribometer was coupled to a three-electrode cell, generating a controlled wear simultaneously to the electrochemical measurements.

This new setup has a vinyl counter part and produces a third-body abrasive wear mechanism and linear motion and. To produce a third-body wear mechanism, abrasive diamond particles and a system with a ball joint connected to sample were used (Fig. 4).
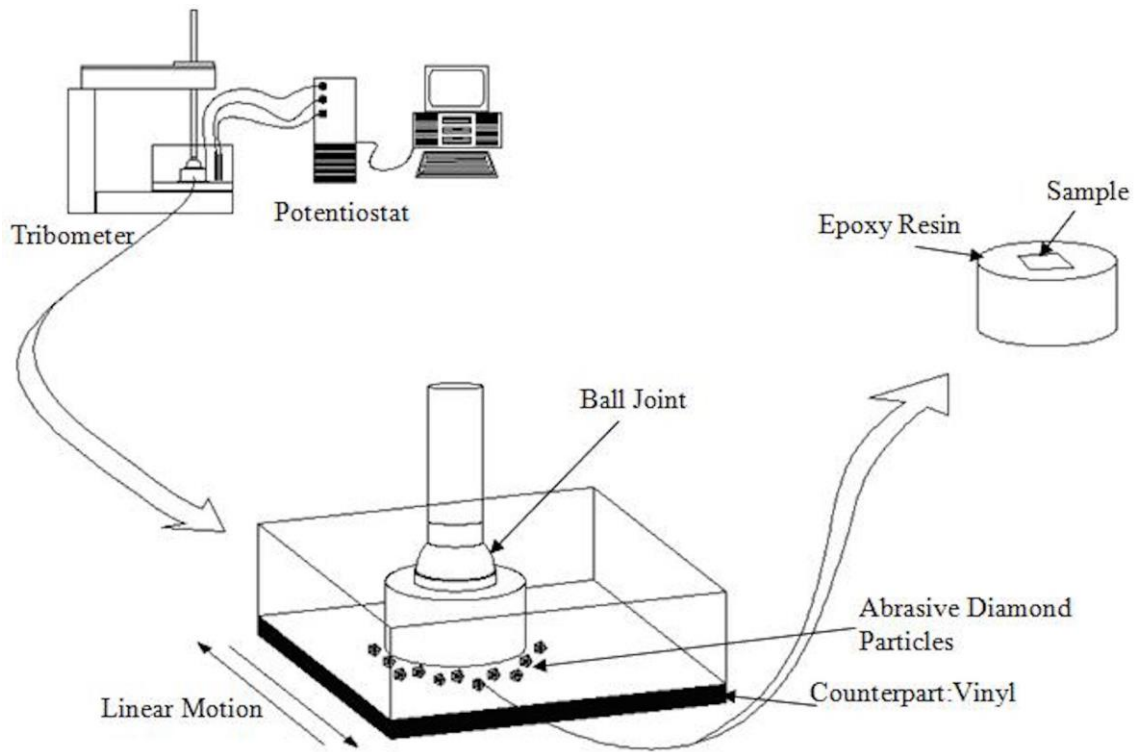
Fig. 4: Schematic of the triboelectrochemical setup.

The triboelectrochemical tests were performed at a normal load of 1N, speed of 0.6 cm/s, and a total sliding distance of 10 mm. The working electrode (supermartensitic stainless steel) was immersed in the electrolyte of 35g/L of sodium chloride aqueous solution for 1h before testing in order to ensure that the steady state was achieved.

Potentiodynamic polarization

Potentiodynamic polarization experiments were carried out to study the corrosion and tribocorrosion behavior of the supermartensitic stainless steel. The potentiodynamic polarization curves were measured under tribocorrosion and corrosion conditions.

Potentiodynamic polarization experiments were conducted using a potentiostat (Gamry Reference 600). A three electrodes cell was used. Working electrodes were made of

supermartensitic stainless steel, with an exposed area of 1 cm^2. The reference electrode was a Ag/AgCl (saturated KCl) with a platinum mesh as the counter electrode. The tests were performed at room temperature.

The open circuit potential (OCP) measurements in a 35 g/L NaCl aqueous solution was performed for 1h. The potentiodynamic polarization curves were obtained at a fixed scan rate (0.167 mV/s) from -30 mV below the observed open circuit potential. The experiments stopped when the current reached 1mA/cm^2. The measurements were performed in three replicates.

Results and discussion

Details of the setup

Potentiodynamic testing was conducted with the purpose to evaluate the overall corrosion and tribocorrosion behavior of the supermartensitic stainless steel in the test solution. Fig. 5 shows the polarization curves obtained under tribocorrosion and corrosion conditions, using 140–170 μm abrasive diamond particles.
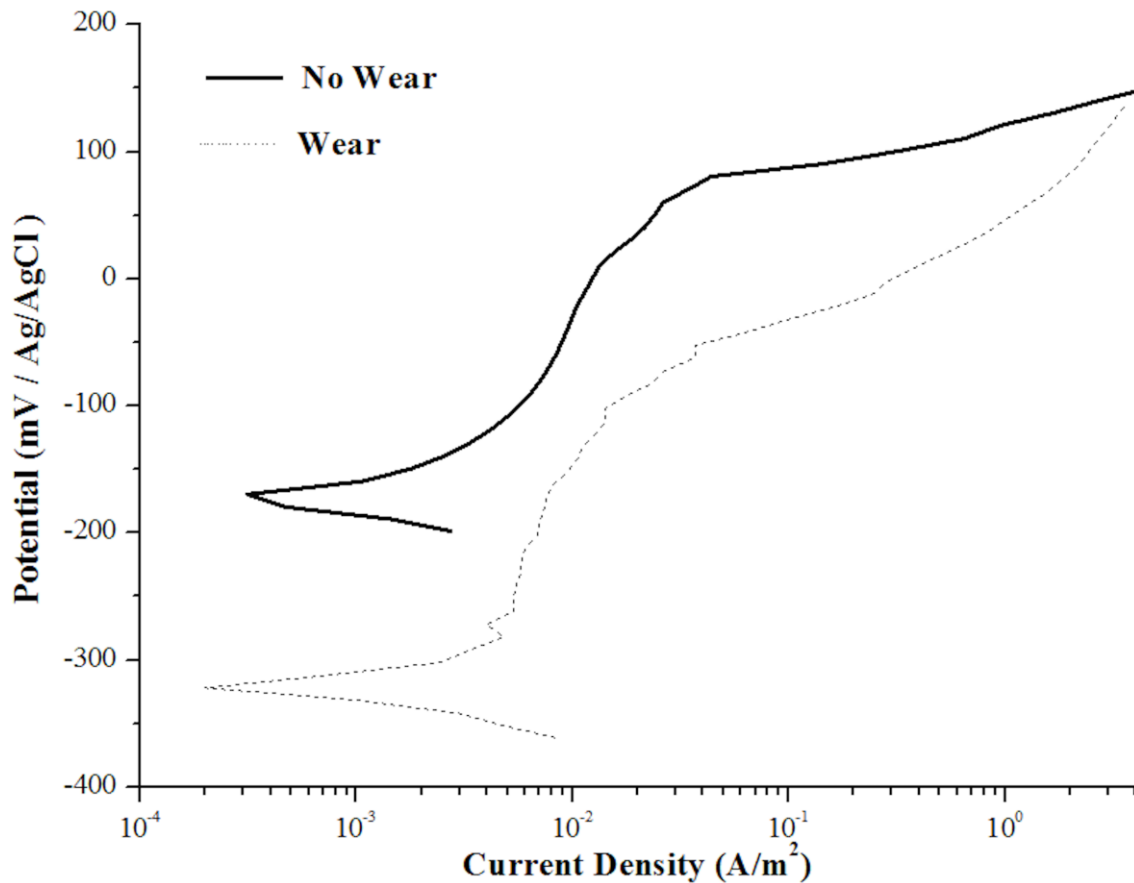
Fig. 5: Potentiodynamic experiments for supermartensitic stainless steel samples under tribocorrosion condition using 140–170 μm abrasive diamond particles and corrosion condition in a saline solution.

During tribocorrosion, the corrosion potential was found to be shifted cathodically from -170 mV to -321 mV, similar to the reported data [3, 24, 59, 60]. Mischler [3] reported that under tribocorrosion conditions, the corrosion potential of the passive titanium alloys shifts to lower values (cathodic shift). The corrosion potential under tribocorrosion conditions reflects the galvanic coupling of two surface states of the alloy: the passive metal (unworn area), and the partially bare metal (worn area) [60]. Ponthiaux et al. [61] reported that the corrosion potential of active metals is not significantly affected by rubbing. Literature [61] cited that the ratio between worn and unworn areas, the relative position of worn and unworn areas, the intrinsic corrosion

potential of the worn and unworn surfaces, and mechanisms and kinetics of involved reactions affected the corrosion potential of metals under tribocorrosion conditions.

Sun and Rana [24] observed that under sliding condition, in the polarization curve of AISI 304 steel, the current density increases continuously and the abrupt increase of current density did not occur. In this work, the passivation and transpassivation regions were identified under tribocorrosion and corrosion conditions. The breakdown potential under tribocorrosion (-50 mV) was shifted to a lower value, compared with corrosion curve (83 mV). The passivation current density during the tribocorrosion condition $((9.91 \pm 0.13)$ mA/m2) was increased in relation the passivation current obtained during corrosion condition $((8.00 \pm 0.43)$ mA/m2), but the values are of the same magnitude order. The increase of the passivation current density under tribocorrosion conditions occurs due to the mechanical destruction of the protective film, leading to an nearly active state, and depends on the ratio between worn and unworn area of electrode, being proportional to this ratio [3]. If the ratio is low, any effect can be observed [61].

In order to understand the change in the coefficient of friction (COF) depending on the current densities registered, the potentiodynamic curve was superposed with the friction curve (Fig. 6). After corrosion took place, the COF decreases due to the development of the oxide film. The friction coefficient remained constant as the number of wear cycles increased, indicating that the contact area between the steel and the abrasive diamond particles remained approximately constant. The breakdown potential occurred after 53 wear cycles. The friction coefficient was similar in the passive and transpassive regions. In literature, a slight decrease in COF was observed as the current increases in transpassive region [24]. In the passive region, the depassivated areas were generated by

the action of the abrasive diamond particles while after the breakdown potential, in the transpassive region, the depassivated areas were produced by the abrasive particles, by the generation of tribo-pits or dissolution of oxide layer. However, the predominant effect was produced by the abrasion of diamond particles. This could be due to the fact that the tribo-pits are small and their propagation was inhibited in the tribocorrosion condition.

The values of roughness after the corrosion tests, Ra=(0.032±0.004) μm, and after the tribocorrosion tests, Ra=(0.306±0.001) μm, compared to the initial roughness, Ra=(0.017±0.003) μm, confirm the predominant effect of the abrasion of diamond particles on the friction coefficient compared to the effect of corrosion. These results suggest that the evolution of the depassivated area and the passive areas during wear action is constant which helps to maintain the friction coefficient constant. The formation of pitting resulted the increase in surface roughness of the wear track and would lead to increase friction coefficient. On the contrary, pitting reduces the real contact area inside the wear track and thus lead to reduce friction coefficient due to reduced contribution from adhesive junction shearing. These competing effects resulted that friction coefficient remained constant in transpassive region.
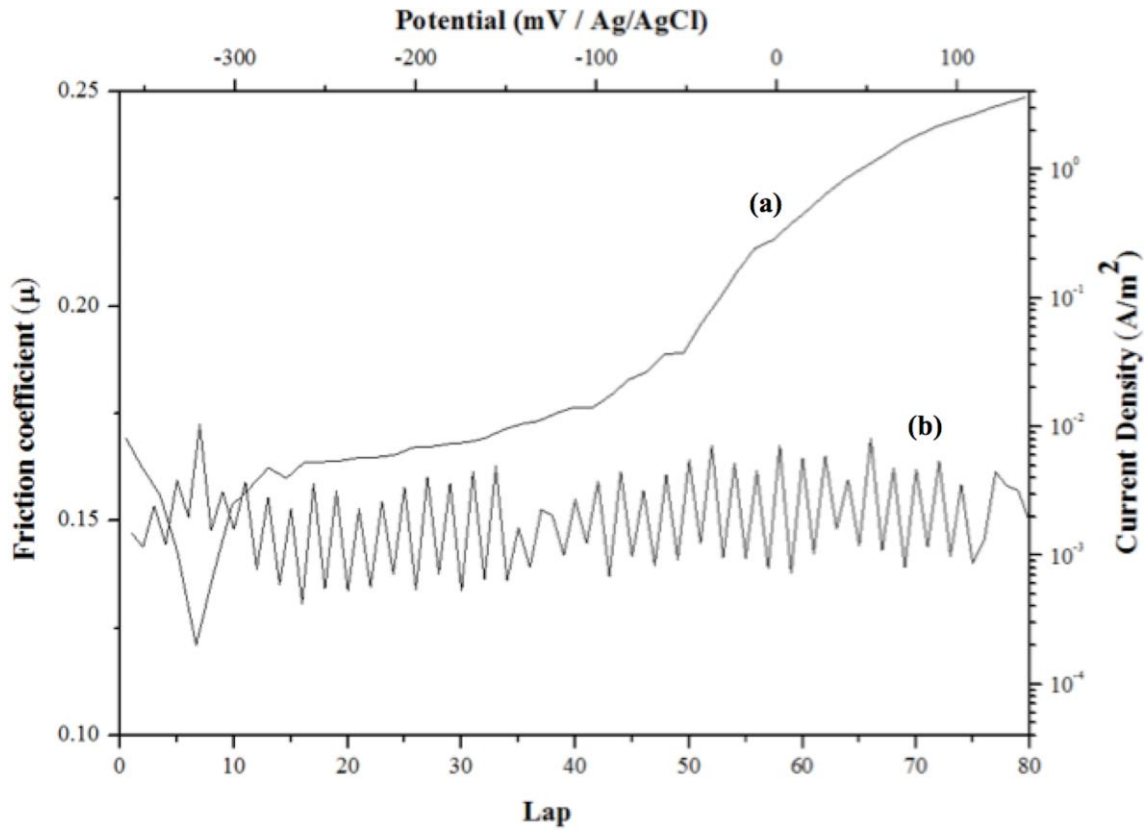
Fig. 6: Potentiodynamic (a) and friction coefficient (b) experiments for supermartensitic stainless steel samples under tribocorrosion condition using 140–170 μm abrasive diamond particles.

The morphology of supermartensitic stainless steel samples after polarization measurements under tribocorrosion and corrosion conditions was characterized using SEM analysis, and is shown in Fig. 7 (a, b).

Globular pits nucleated at the polishing scratches under corrosion condition (Fig. 7 (a)). Fig. 7 (b) shows the SEM morphology of a wear surface which was produced by three-body abrasive wear, and the scars produced after testing under tribocorrosion condition consists of multiple indentations on the surface produced by abrasives diamond particles in 35 g/L NaCl solution, indicating that three-body abrasion is the dominant wear mechanism (Fig. 7 (b)). The passive metal is the first body, with the diamond particles

are the second body. The counter body detaches wear particles from the steel that can be directly ejected from the contact or transferred into the third body [3]. The third body particle can adhere to the diamond particles or to the steel or can get fragmented in smaller particles [3]. Corrosion occurs on third-body particles during fragmentation and on the first body (steel) after particle detachment [3].
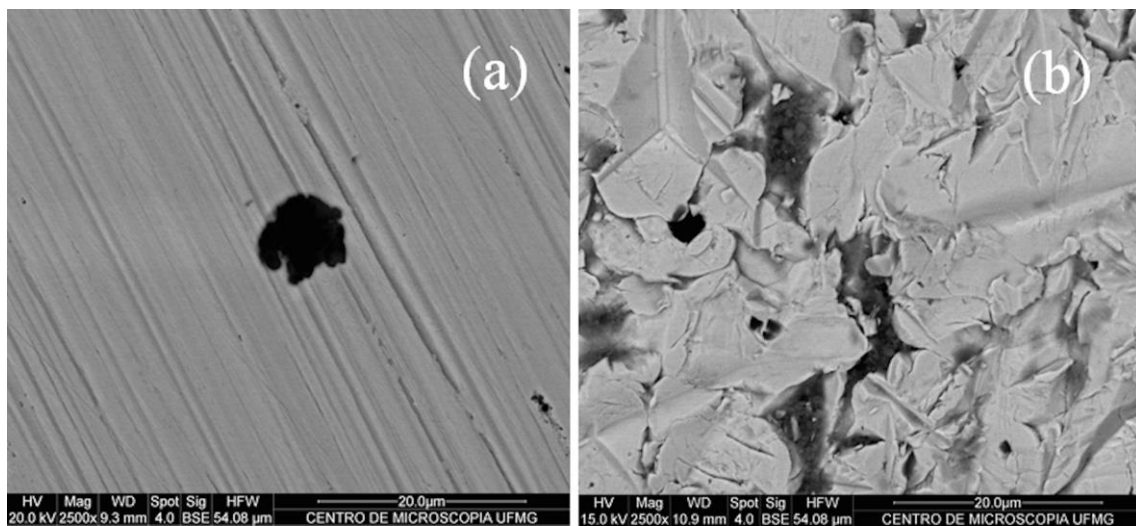
Fig. 7: Morphologies of supermartensitic stainless steel samples after polarization measurements under corrosion condition (a) and under tribocorrosion condition using diamond particles of 140-170 μm (b).

The Fig. 8 shows the sample profiles of supermartensitic stainless steel before (a) and after polarization measurements under corrosion (b) and under tribocorrosion condition (c).
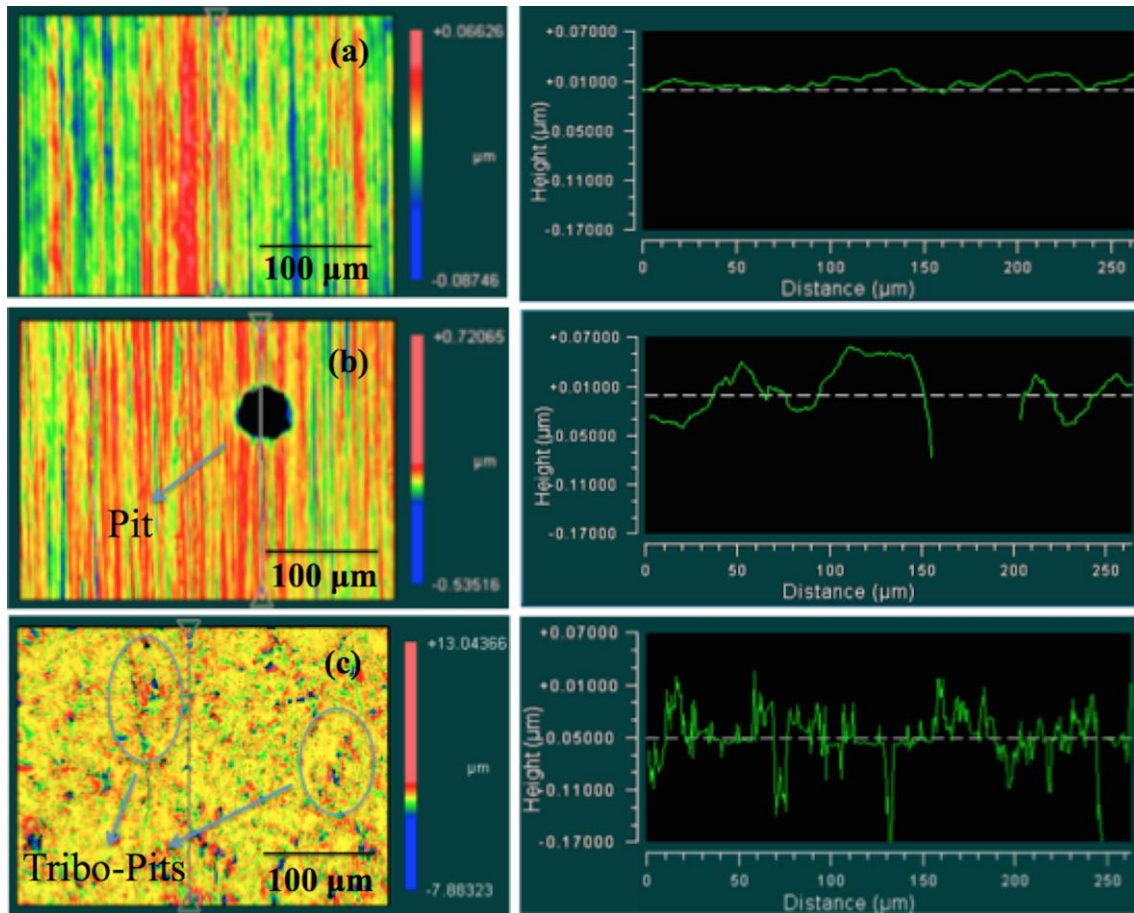
Fig. 8: Sample profiles of supermartensitic stainless steel before (a) and after polarization measurements under corrosion (b) and under tribocorrosion conditions using diamond particles of 140–170 μm (c).

The sample profiles (Fig. 8) exhibited different shapes of pits that were observed after polarization measurements under tribocorrosion and corrosion conditions. On the steel surface submitted to a corrosion mechanism, pits were nucleated and propagated according to an autocatalytic mechanism. One mechanism of pit initiation is the penetration mechanism, where chlorides were transported through the oxide film on to the surface metal and a localized dissolution of metal occurred. MacDonald et al. [62, 63] proposed a point defect model responsible for the breakdown of passivity. As the metal dissolution proceeds, cation vacancies migrate from the oxide/electrolyte

47

interface and accumulate at the metal/oxide interface, leading to pit nucleation [63]. In the film rupture mechanism, chloride ions penetrate the passive film through cracks in the oxide layer [63]. Chloride ions attack the passive film at localized points generating Fe^{2+} which attract chloride ions, producing $FeCl_2$:

$$Fe_{(s)} \rightarrow Fe^{2+}_{(aq)} + 2\bar{e} \quad \text{Eq. (1)}$$

$$Fe^{2+}_{(aq)} + 2Cl^{-}_{(aq)} \rightarrow FeCl_{2(s)} \quad \text{Eq. (2)}$$

Accumulated metal cations and the iron chloride undergo hydrolysis, and a localized acidity was developed inside a pit, accelerating the attack to steel [63]:

$$FeCl_{2(s)} + 2H_2O_{(l)} \rightarrow Fe(OH)_{2(aq)} + 2H^{+}_{(aq)} + 2Cl^{-}_{(aq)} \quad \text{Eq. (3)}$$

$$Fe_{(s)} + HCl_{(aq)} \rightarrow FeCl_{2(aq)} + H_{2(g)} \quad \text{Eq. (4)}$$
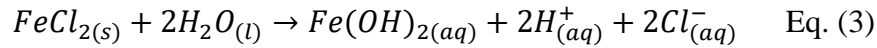
However, pits were nucleated on the steel surface submitted to a tribocorrosion mechanism, but at each abrasive cycle, more steel surface was exposed to the corrosive environment increasing the active area. More pits were nucleated (tribo-pits) on steel surface in tribocorrosion condition than in the corrosion condition but the pit propagation was inhibited. Sun and Rana [24] also reported many small pits mainly inside the wear track, with only few larger pits being found outside the wear track when studying tribocorrosion behavior of AISI 304 steel in 0.5M sodium chloride solution. After the tribocorrosion tests, an average of 646±51 pits were observed in an area of 1 μm^2, while an average of 11±2 pits were identified in the same area after the corrosion

tests. The higher concentration of pits after the tribocorrosion tests is due to the competition between pit growth and wear exposing more active area during the rubbing process. Results reported by Sun and Rana [24] demonstrated that the morphology of corrosion inside the wear track determines the dominance of the two synergistic components: when pitting corrosion occurs, as in this research, corrosion-induced wear becomes more dominant in the synergism. According to the model proposed by Jiang et al. [64], wear in tribocorrosion can be considered as a low cycle fatigue process, involving crack initiation and propagation. Under sliding condition, the passive film on real contact areas is removed or damaged after a single cycle or after some cycles of sliding, accelerating the electrochemical corrosion in the real contact areas and contributing to wear-induced corrosion [24]. The formation of pits inside the wear track can in turn affect the wear of steel. The formation of pits would reduce the real contact area for subsequent cycles and thus lead to higher contact stresses and then higher wear rates. Each pit can serve as a site for crack nucleation and a site of stress concentration, promoting crack initiation [24]. Sun and Rana [24] reported cracking and collapsing of material at the edge of pit to form wear debris. One explanation about the small size of pits inside the wear track was given by Sun and Rana [24]. There is a competition between pit growth and wear. One effect of wear is the decrease of the depth of the pits difficulting to maintain an aggressive solution inside the pit. Thus the rate of pit growth inside the wear track is reduced. According to Pistorius and Burstein [65], the critical condition for pit growth is that the pit stability product, Ir, must exceed a critical value (where I is the current density and r is pit radius). As the pit size is reduced due to wear and the current density is reduced due to the dilution of the solution inside the pit, the Ir value will drop below the critical value, and thus pit growth will be inhibited.

Effects of particle size

To study the abrasive size effect on tribocorrosion behavior of supermartensitic stainless steel, abrasive diamond particles of 10-20 μm, 30-40 μm, 40-60 μm, 140–170 μm size range were used. Fig. 9 shows the polarization curves obtained under corrosion condition and tribocorrosion condition using abrasive diamond particles of 10-20 μm, 30-40 μm, 40-60 μm, 140–170 μm size ranges.

During tribocorrosion, the corrosion potential was found to be shifted to a lower value when the diamond particle size decreases (Table 3). Stack et al. [59] studied the erosion-corrosion behavior of a Cr (11.8 wt.%) containing steel and also reported a decrease of corrosion potential as the erodent particle size decreases. The breakdown potential under tribocorrosion condition using diamond particles of a larger size (140–170 μm) is shifted to a lower value, compared with the corrosion curve and with the tribocorrosion condition using diamond particles of the smallest size (10-20 μm). The passivation current density of supermartensitic steel under the tribocorrosion condition using diamond particles of the smallest size increases in relation the passivation current obtained under corrosion and tribocorrosion condition using diamond particles of larger size, indicating a decreased of the passivation efficiency. Stack et al. [59] also reported the increase of passivation current density of a Cr-steel as the erodent particle size decreases. This result occurs due to a higher abrasion of diamond particles of smaller size, leading to a higher destruction of the protective film mechanically. The smaller particle size generates more electrochemical response (current) under the abrasion-corrosion [58]. The time for repassivation between particle impacts is reduced by a reduction in particle size [58]. Sun et al. [58] reported that reducing the particle size, the

wear induced corrosion current increased for the same amount of material removal, which implies a potentially higher metal ion release rate. Table 3 shows that decreasing the particle size, the passivation current density increased.

Considering the tribocorrosion mechanism, an advantage of the use of a supermartensitic steel is that the steel has a higher resistance to plastic deformation than the austenitic one. The presence of a plastic deformation induced by wear could accelerate the corrosion-wear rate of materials under sliding conditions [26]. Wear induces plastic deformation and increases the density of dislocations making the steel surface more active [24]. On the other hand, the supermartensitic steel has a lower chromium content than the austenitic steels (greater than 18% wt.), which would require a longer time to repassivation. Considering this hyphothesis, the effect of larger particles would be less harmful than the effect of smaller abrasive particles, because the time between sliding contacts is lower when the abrasive particle size is smaller. And this result was observed in this work as shown in Table 3 and Fig. 9.
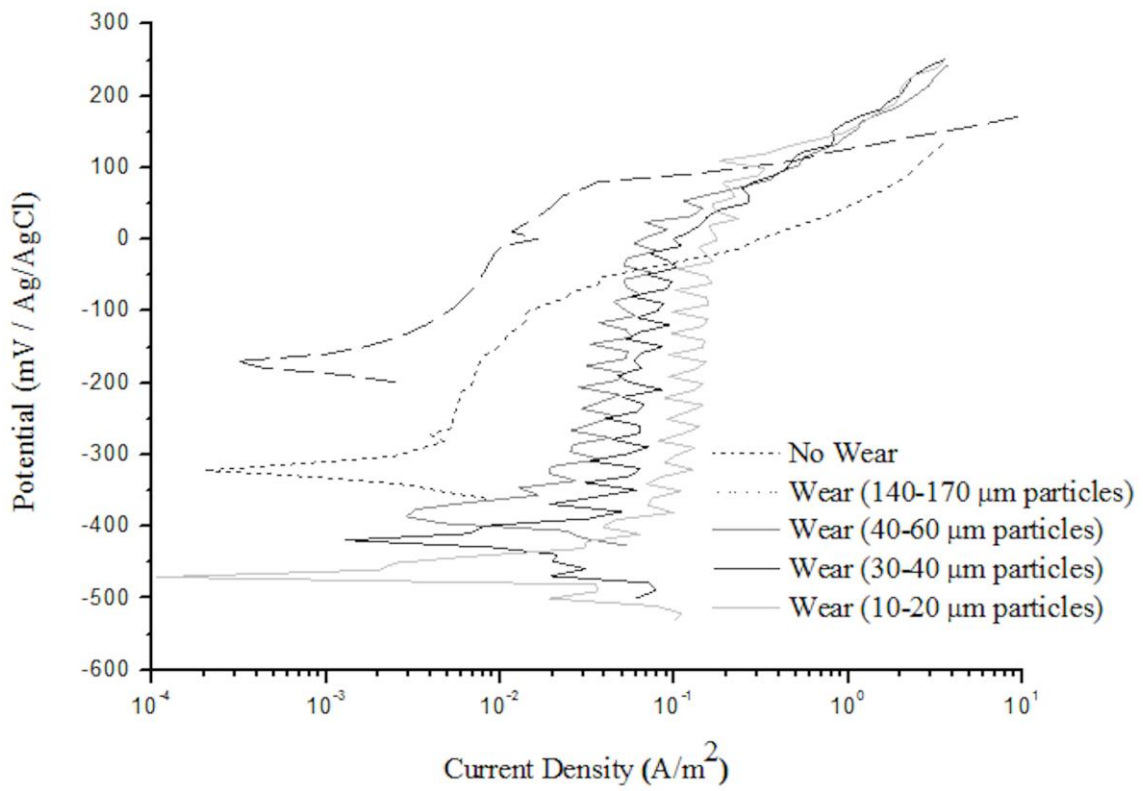
Fig. 9: Potentiodynamic polarization curves for supermartensitic stainless steel samples under corrosion (a) and under tribocorrosion condition using diamond particles of size range (b) 10-20 µm, (c) 30-40 µm, (d) 40-60 µm, (e) 140–170 µm.

Table 3 shows the electrochemical parameters obtained using potentiodynamic polarization tests.

Table 3: Electrochemical parameters obtained using potentiodynamic polarization of the supermartensitic stainless steel samples in 35 g/L NaCl solution.

Conditions	Corrosion potential E_{corr} (mV / Ag/AgCl)	Breakdown potential E_b (mV / Ag/AgCl)	Passivation current density i_{pass} (mA/m^2)
No Wear	-170	83	8.00±0.43
Wear (10-20 μm particles)	-470	104	140.55±21.71
Wear (30-40 μm particles)	-417	-10	69.60±5.66
Wear (40-60 μm particles)	-382	25	38.45±2.76
Wear (140-170 μm particles)	-321	-50	9.91±0.13

Fig. 10 shows the friction coefficient measured under tribocorrosion condition using diamond particles of (a) 10-20 μm, (b) 30-40 μm, (c) 40-60 μm, (d) 140–170 μm size range. Higher values of friction coefficient were obtained by using diamond particles of smaller sizes due to a higher contact area inside the wear track, compared to the friction coefficient values produced by diamond particles of larger sizes. Using particles of a smaller size, the time for repassivation is reduced.
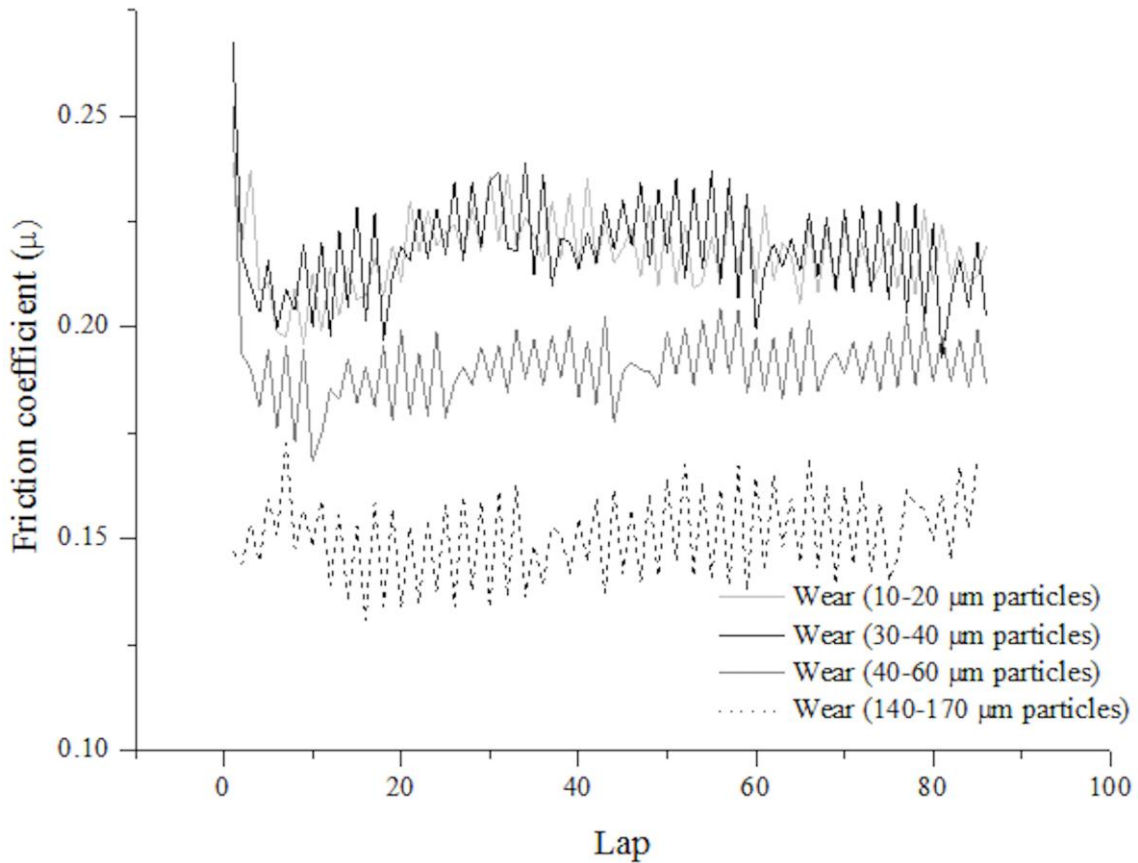
Fig. 10: Friction coefficient for supermartensitic stainless steel samples under tribocorrosion condition using diamond particles of (a) 10-20 μm, (b) 30-40 μm, (c) 40-60 μm, (d) 140–170 μm size range.

The morphology of supermartensitic stainless steel samples after polarization measurements under corrosion and under tribocorrosion condition using abrasive di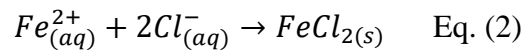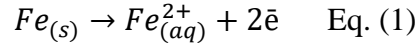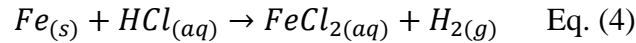amond particles of size range 10-20 μm, 30-40 μm, 40-60 μm, 140–170 μm were characterized using SEM analysis, as shown in Fig. 11 (a, b, c, d, e).

Under corrosion condition, globular pits nucleated at the polishing scratches (Fig. 11 (a)). Fig. 11 (b, c, d, e) shows the SEM morphology of a wear surface which was produced by abrasive wear of the diamond particles of size range 10-20 μm, 30-40 μm, 40-60 μm, 140–170 μm, and larger indentations was observed on the surface produced

after testing under tribocorrosion using diamond particles of larger size (140–170 μm). The smallest abrasive particles (10-20 μm) promoted the highest pit growth inhibition.
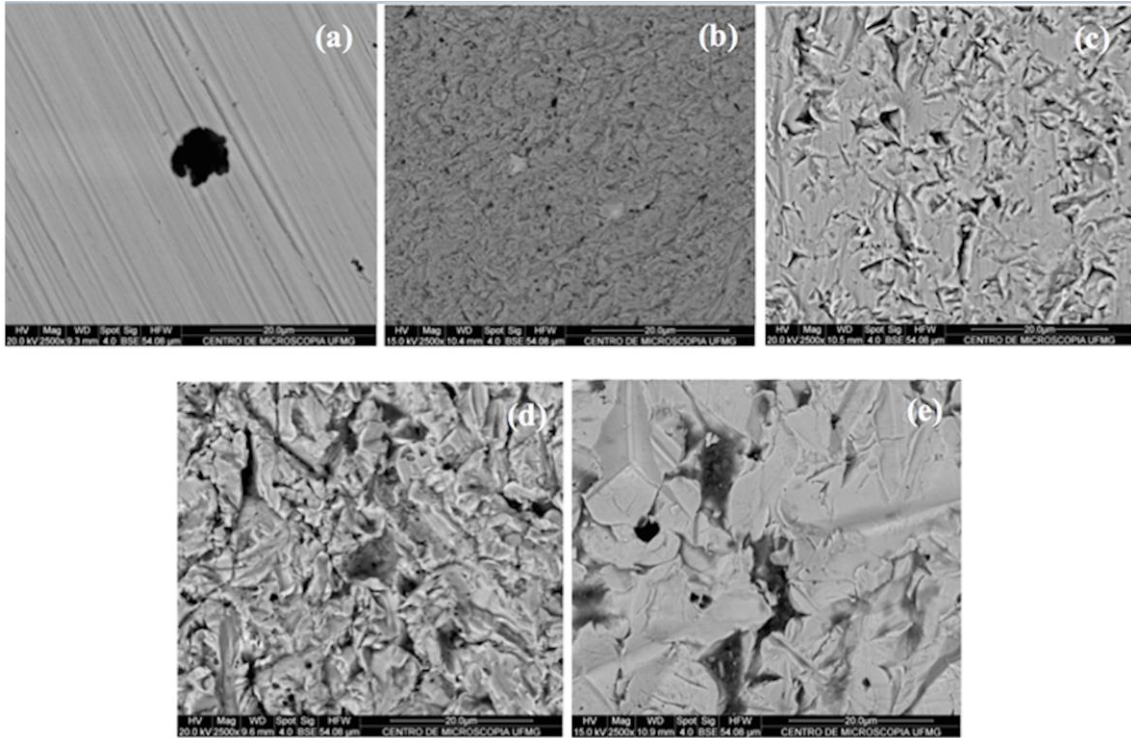
Fig. 11: Morphology of supermartensitic stainless steel samples after polarization measurements without wear (a) and under wear using diamond particles of size range (b) 10-20 μm, (c) 30-40 μm, (d) 40-60 μm, (e) 140–170 μm.

The values of roughness of steel samples after the tribocorrosion tests increased compared to the roughness after the corrosion tests (Fig 12). Higher values of roughness were observed after the tribocorrosion tests using diamond particles of larger sizes (40-60 μm, 140–170 μm), compared to the values of roughness after the tribocorrosion tests using diamond particles of smaller sizes (10-20 μm, 30–40 μm).
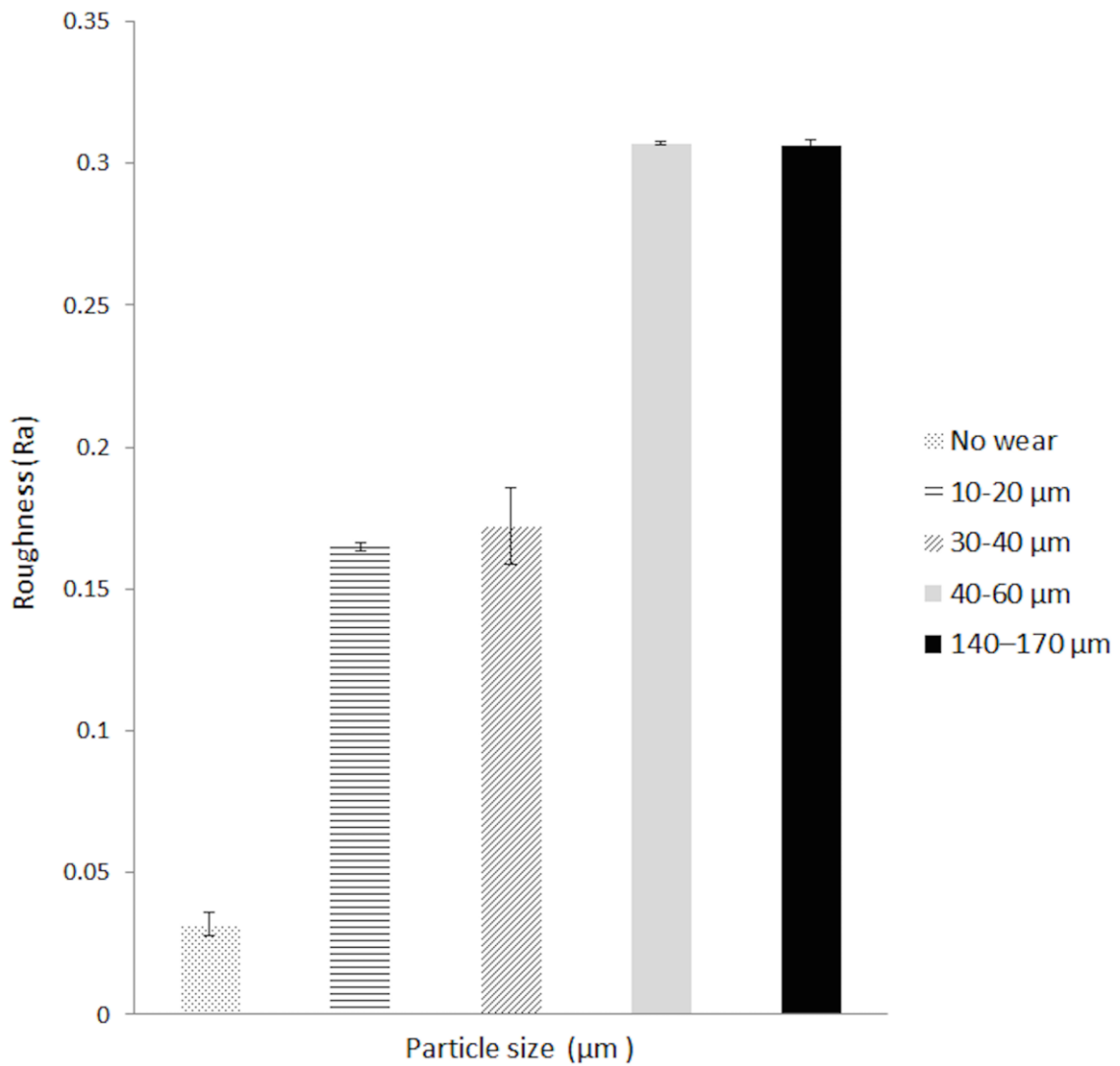
Fig. 12: Roughness of supermartensitic stainless steel samples after polarization measurements under corrosion and under tribocorrosion using diamond particles of size range (b) 10-20 μm, (c) 30-40 μm, (d) 40-60 μm, (e) 140–170 μm.

Conclusions

A tribocorrosion setup was configured in order to study the triboelectrochemical behavior of a supermartensitic steel. In this setup, the tribological contact was comprised a pin (vertical) in contact with a ball joint connected to sample, which underwent oscillatory linear motion. The configuration allowed synchronizing data of

corrosion and tribology.

The open circuit potential of supermartensitic steel in a saline solution is shifted to a lower value due to wear. The passivation current density increased as the abrasive particle size decreased. There is a trend to increase the breakdown potential as the particle size decreases.

Different shapes of pits were observed after polarization measurements under corrosion and under tribocorrosion conditions. The pit size on the steel surface submitting to a tribocorrosion mechanism was smaller and the pit concentration was higher than in the corrosion condition. The smallest abrasive particles (10-20 μm) promoted the highest pit growth inhibition.

The scars produced after testing indicating that three-body abrasion is the dominant wear mechanism.

The friction coefficient of supermartensitic steel was similar in the passive and transpassive regions. The breakdown potential occurred after 53 wear cycles. Higher values of friction coefficient were obtained by using diamond particles of smaller sizes due to a higher contact area inside the wear track, compared to the friction coefficient values produced by diamond particles of larger sizes.

Acknowledgments

the financial support for this research.

References

[1] M.T. Mathew, T. Uth, N.J. Hallab, R. Pourzal, A. Fischer, M.A. Wimmer, Construction of a tribocorrosion test apparatus for the hip joint: Validation, test methodology and analysis, Wear 271(2011) 2651-2659.

[2] D. Landolt, S. Mischler, M. Stemp, Electrochemical methods in tribocorrosion: a critical appraisal, Electrochim. Acta 46 (2001) 3913-3929.

[3] S. Mischler. Triboelectrochemical techniques and interpretation methods in tribocorrosion: A comparative evaluation, Tribology International 41 (2008) 573-583.

[4] P. Ponthiaux, F. Wenger, J.-P Celis. Tribocorrosion: Material Behavior Under Combined Conditions of Corrosion and Mechanical Loading, Corrosion Resistance, InTech, 2012.

[5] F. Ben Saada, Z. Antar, K. Elleuch, P. Ponthiaux, On the tribocorrosion behavior of 304 L stainless steel in olive pomace/tap water filtrate, Wear 328 (2015), 509-517.

[6] A. López, R. Bayón, F. Pagano, A. Igartua, A. Arredondo, J.L. Arana, J.J. González, Tribocorrosion behaviour of mooring high strength low alloy steels in synthetic seawater, Wear 338-339 (2015) 1-10.

[7] Jun Chen, Qing Zhang, Quan-an Li, San-ling Fu, Jian-zhang Wang, Corrosion and tribocorrosion behaviors of AISI 316 stainless steel and Ti6Al4V alloys in artificial seawater, Trans. Nonferrous Met. Soc. China 24 (2014) 1022-1031.

[8] Jun Chen, Feng-yuan Yan, Tribocorrosion behaviors of Ti–6Al–4V and Monel K500 alloys sliding against 316 stainless steel in artificial seawater, Trans. Nonferrous Met. Soc. China 22 (2012) 1356-1365.

[9] D. Landolt, S. Mischler, M. Stemp, S. Barril, Third body effects and material fluxes in tribocorrosion systems involving a sliding contact, Wear 256 (2004) 517-524.

[10] S.B. Joo and H. Liang, In Situ Characterization of Tribo-Electrochemical Effects on Topography of Patterned Copper Surfaces, J. Electronic Matls. 42 (2013) 979-987.

[11] S. Joo and H. Liang, Mechanisms of Step Height Reduction in Copper Chemical Mechanical Polishing (CMP), Microelectronic Engineering 98 (2012) 12-18.

[12] F. Gao and H. Liang, Effects of Potential and Mechanical Stimulation on Oxidation of Tantalum during Electrochemical-Mechanical Polishing, J. Elec. Matls. 41 (2012) 624-631.

[13] F. Gao and H. Liang, Transformable Oxidation of Tantalum in Electrochemical-Mechanical Polishing of Tantalum, J. Electro. Matls. 40 (2011) 134-140.

[14] K. Wang, Z. Liu, T. Cruz, M. Salmeron, and H. Liang, In Situ Spectroscopic Observation of Activation and Transformation of Tantalum Suboxides, J. Phys. Chem. A, A, 114 (2010) 2489–2497.

[15] F. Gao and H. Liang, Material Removal Mechanisms in Electrochemical-Mechanical Polishing of Tantalum, Electrochim. Acta 54 (2009) 6808-6815.

[16] F. Gao and H. Liang, In Situ Observation of Friction-Induced Electrochemical Reactions and Impedance in Tantalum-ECMP, J. Elecchem. Soc. 156 (2009) H80-H86.

[17] P. Kar, P. Asthana, and H. Liang, Formation and Characterization of Tribofilms, J. Tribo. 130 (2008) 04201-042306.

[18] ZOU, Dening, HAN, Ying, ZHANG, Wei, FANG, Xudong, Influence of Tempering Process on Mechanical Properties of 00Cr13Ni4Mo Supermartensitic Stainless Steel, J. Iron Steel Res. Int. 17 (2010) 50-54.

[19] YE, Dong, LI, Jun, JIANG, Wen, SU, Jie, ZHAO, Kunyu, Effect of Cu addition on microstructure and mechanical properties of 15%Cr super martensitic stainless steel,

Mater. Des. 41 (2012) 16-22.

[20] C.A. Della Rovere, C.R. Ribeiro, R. Silva, L.F.S. Baroni, N.G. Alcântara, S.E. Kuri, Microstructural and mechanical characterization of radial friction welded supermartensitic stainless steel joints, Mater. Sci. Eng. A 586 (2013) 86-92.

[21] X.P. Ma, L.J. Wang, C.M. Liu, S.V. Subramanian, Microstructure and properties of 13Cr5Ni1Mo0.025Nb0.09V0.06N supermartensitic stainless steel, Mater. Sci. Eng. A 539 (2012) 271-279.

[22] X.P. Ma, L.J. Wang, C.M. Liu, S.V. Subramanian, Role of Nb in low interstitial 13Cr super marttititensitic stainless steel, Mater. Sci. Eng. A 528 (2011) 6812-6818.

[23] C.A.D. Rodrigues, P.L.D. Lorenzo, A. Sokolowski, C.A. Barbosa, J.M.D.A. Rollo, Titanium and molybdenum content in supermartensitic stainless steel, Mater. Sci. Eng. A 460-461 (2007) 149-152.

[24] Y. Sun, V. Rana, Tribocorrosion behaviour of AISI 304 stainless steel in 0.5 M NaCl solution. Mater. Chem. and Phys. 129 (2011) 138-147.

[25] Santos et al., 2015. Abrasion–corrosion: New insights from force measurements 332-333 (2015), 1206-1214.

[26] A. Berradja, F. Bratu, L. Benea, G. Willems, J-P. Celis, Effect of sliding wear on tribocorrosion behaviour of stainless steels in a Ringer's solution, Wear, 261 (2006) 987-993.

[27] Michel Keddam, Pierre Ponthiaux, Vincent Vivier, Tribo-electrochemical impedance: A new technique for mechanistic study in tribocorrosion, 124 (2014) 3-8.

[28] P. Kar, K. Wang, and H. Liang, Force-Dominated Non-Equilibrium Oxidation Kinetics of Tantalum, Electrochim. Acta 53 (2008) 5084-5091.

[29] P. Kar, K. Wang, and H. Liang, Oxidation of Tantalum with Mechanical Force, Electrochem. & Solid-State Lett. 11 (2008) C13-C17.

[30]   F. Gao, S. Joo, and H. Liang, Ch. 4.2. Tribology and CMP and Case Studies on Tantalum in Tribocatalysis, Tribochemistry, and Tribocorrosion, Edied. K. Hiratsuka and C. Kajdas, Pan Stanford Publishing, 2015.

[31] S. Joo and H. Liang, Ch. 23, Tribology in Chemical-Mechanical Planarization, Tribology for Scientists and Engineers, Ed. P.L. Menezes, S. Ingole, M. Nosonovsky, S.V. Kailas, and M.R. Lovell, Springer Science+Business Media, NY, 2013.

[32] H. Liang, Chemical-Mechanical Polishing, Ed. Q. Wang and YW Chang, Springer, 2012.

[33] M. Kulkarni, F. Gao, and H. Liang, Chemical-mechanical Polishing (CMP): a Controlled Tribocorrosion Process, Tribocorrosion of Passive Metals and Coatings, Edi. Dieter & Mischler, Woodhead Publishing, 2011.

[34] M. Kulkarni, F. Gao, and H. Liang, Chapter 18, Chemical Mechaical Polishing, Tribocorrosion of Passive Metals and Coatings, ed. D. Landolt and S. Mischler, Woodhead Publishing, 2011.

[35] M. Azzi, J.A. Szpunar, Tribo-electrochemical technique for studying tribocorrosion behavior of biomaterials, Biomol. Eng. 24 (2007) 443-446.

[36] S. Guadalupe Maldonado, S. Mischler, M. Cantoni, W-J. Chitty, C. Falcand, D. Hertz, Mechanical and chemical mechanisms in the tribocorrosion of a Stellite type alloy, Wear 308 (2013) 213-221.

[37] É. Martin, M. Azzi, G.A. Salishchev, J. Szpunar, Influence of microstructure and texture on the corrosion and tribocorrosion behavior of Ti–6Al–4V, Tribol. Int. 43 (2010) 918-924.

[38] S.A. Naghibi, K. Raeissi, M.H. Fathi, Corrosion and tribocorrosion behavior of Ti/TiN PVD coating on 316L stainless steel substrate in Ringer's solution, Mater. Chem. and Phys. 148 (2014) 614-623.

[39] D. Siva Rama Krishna, Y. Brama, Y. Sun, Thick rutile layer on titanium for tribological applications, Tribol. Int. 40 (2007) 329-334.

[40] I. García, D. Drees, J.P. Celis, Corrosion-wear of passivating materials in sliding contacts based on a concept of active wear track area, Wear 249 (2001) 452-460.

[41] R. Pourzal, A. Fischer, Reciprocating Sliding Wear of Surface Modified Austenitic High Nitrogen Stainless Steel and CoCrMo-alloy, Friction, Wear and Wear Protection, Wiley-VCH, 2008.

[42] M. Salasi, G.B. Stachowiak, G.W. Stachowiak, Three-body tribocorrosion of high-chromium cast irons in neutral and alkaline environments, Wear 271 (2011) 1385-1396.

[43] S. Sharifi, M.M. Stack, L. Stephen, Wang-Long Li, Moo-Chin Wang, Micro-abrasion of Y-TZP in tea, Wear 297 (2013) 713-721.

[44] M.M. Stack, W. Huang, G. Wang, C. Hodge, Some views on the construction of bio-tribo-corrosion maps for Titanium alloys in Hank's solution: Particle concentration and applied loads effects, Tribol. Int. 44 (2011) 1827-1837.

[45] M.A. Wimmer, J. Loos, R. Nassutt, M. Heitkemper, A. Fischer, The acting wear mechanisms on metal-on-metal hip joint bearings: in vitro results, Wear 250 (2001) 129-139.

[46] F.G. Oliveira, A.R. Ribeiro, G. Perez, B.S. Archanjo, C.P. Gouvea, J.R. Araujo, A.P.C. Campos, A. Kuznetsov, C.M. Almeida, M.M. Maru, C.A. Achete, P. Ponthiaux, J.P. Celis, L.A. Rocha, Understanding growth mechanisms and tribocorrosion behaviour of porous TiO_2 anodic films containing calcium, phosphorous and magnesium, Appl. Surf. Sci. 341 (2015) 1-12.

[47] Andrew Emge, S. Karthikeyan, H.J. Kim, D.A. Rigney, The effect of sliding velocity on the tribological behavior of copper, Wear 263 (2007) 614-618.

[48] M.M. Stack, K. Chi, Mapping sliding wear of steels in aqueous conditions, Wear

255 (2003) 456-465.

[49] R. Ribeiro, S. Ingole, M. Usta, C. Bindal, A.H. Ucisik, H. Liang, Tribological characteristics of boronized niobium for biojoint applications, Vacuum 80 (2006) 1341-1345.

[50] J. Baxi, P. Kar, H. Liang, A. Polat, M. Usta, A. H. Ucisik, Tribological characterization of microarc oxidized alumina coatings for biological applications, Vacuum 83 (2009) 217-222.

[51] P. Jemmely, S. Mischler, D. Landolt, Tribocorrosion behaviour of Fe–17Cr stainless steel in acid and alkaline solutions, Tribol. Int. 32 (1999) 295-303.

[52] A. Stachowiak, W. Zwierzycki, Analysis of the tribocorrosion mechanisms in a pin-on-plate combination on the example of AISI304 steel, Wear 294–295 (2012) 277-285.

[53] I. Serre, N. Celati, R.M. Pradeilles-Duval, Tribological and corrosion wear of graphite ring against Ti6Al4V disk in artificial seawater, Wear 252 (2002) 711-718.

[54] E. Medvedovski, J. Jiang, M. Robertson, Tribological Properties of the Boride-Based Thermal Diffusion Coatings, Adv. Appl. Ceram. 113 (2014) 427-437.

[55] A.J. Gant, M.G. Gee, A.T. May, The evaluation of tribo-corrosion synergy for WC–Co hard metals in low stress abrasion, Wear 256 (2004) 500-516.

[56] S. Barril, N. Debaud, S. Mischler, D. Landolt, A tribo-electrochemical apparatus for in vitro investigation of fretting–corrosion of metallic implant materials, Wear 252 (2002) 744-754.

[57] D. Royhman, M. Patel, M.J. Runa, J.J. Jacobs, N.J. Hallab, M.A. Wimmer, M.T. Mathew, Fretting-corrosion in hip implant modular junctions: New experimental set-up and initial outcome, Tribol. Int. 91 (2015) 235-245.

[58] D. Sun, J.A. Wharton, R.J.K. Wood, Abrasive size and concentration effects on the

tribo-corrosion of cast CoCrMo alloy in simulated body fluids, Tribol. Int. 42 (2009) 1595-1604.

[59] M.M. Stack, N. Pungwiwat, Erosion–corrosion mapping of Fe in aqueous slurries: some views on a new rationale for defining the erosion–corrosion interaction, Wear 256 (2004) 565-576.

[60] A.C. Vieira, L.A. Rocha, N. Papageorgiou, S. Mischler, Mechanical and electrochemical deterioration mechanisms in the tribocorrosion of Al alloys in NaCl and in $NaNO_3$ solutions, 54 (2012), 26-35.

[61] P. Ponthiaux, F. Wenger, D. Drees, J.P. Celis, Electrochemical techniques for studying tribocorrosion processes, 256 (2004) 459-468.

[62] D.D. MacDonald, Journal of Electrochemical Society, 139 (1992) 3434.

[63] E. McCafferty, Introduction to Corrosion Science, Springer: New York, 2010.

[64] J. Jiang, M.M. Stack, A. Neville, Modelling the tribo-corrosion interaction in aqueous sliding conditions, Tribol. Int. 35 (2002) 669.

[65] P.C. Pistorius, G.T. Burstein, Growth of corrosion pits on stainless steel in chloride solution containing dilute sulphate, Corrosion Science 33 (1992) 1885.

CHAPTER 5

PAPER 2: Influence of nitride inclusions on the localized corrosion of a supermartensitic steel

Supermartensitic steel

Titanium carbonitride

Ti (C, N)

10 μm

SVET

μA/cm²
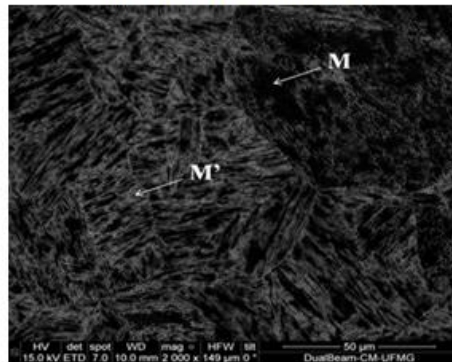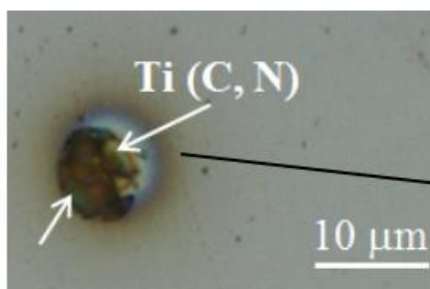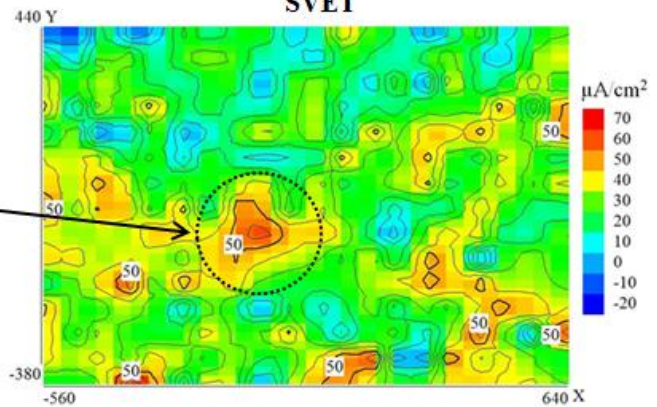
Abstract

The pitting corrosion of supermartensitic stainless steel was studied using the scanning electrode technique (SVET) in 0.1 mol/L NaCl was studied using the vibrating electrode technique (SVET). The supermartensitic steel was tempered for 30 min at a temperature of 600 and 640ºC and air cooled. The SMSS microstructure was characterized using scanning electron microscopy, optical microscopy, X-ray diffraction, Mössbauer spectroscopy and electron backscattering diffraction. The corrosion behavior of SMSS was studied using cyclic voltammetry in 0.1 mol/L NaCl aqueous solution. Coarse cuboidal TiN particles were identified on the steel surfaces. The TiN inclusions showed internal inclusions containing magnesium, aluminum and calcium oxides indicating that the magnesium, aluminum and calcium oxides act as nucleation sites for TiN. Mössbauer spectroscopy identified 0.7, 0.5 and 0.9% of retained austenite in SMSS samples as-quenched and tempered at 600°C and 640°C, respectively. The SMSS sample tempered at 600°C showed the lowest grain size, evaluated by using EBSD technique, and the highest localized corrosion resistance in a saline medium. The SMSS sample tempered at 640°C showed attack after 3600s of immersion in a saline solution was verified using a SVET technique, but after 86400s, pitting was detected. SVET analysis showed the association of a localized corrosion sites with the TiN inclusion on the steel surface.

Introduction

The supermartensitic stainless steels are widely used in the oil and gas industry due to their good mechanical properties, good weldability and a good corrosion resistance in environments containing chlorides, CO_2 and H_2S. Thus, supermartensitic steels have increasingly replaced the more expensive duplex stainless steels have in many onshore and offshore applications. In the oil and gas industry, supermatensitic steels have been used in the manufacture of seamless steel pipe for use in drilling oil and gas [1-6].

Compared to conventional martensitic stainless steels, on the supermartensitic ones contains up to 3% (wt.) molybdenum, added to improve corrosion resistance and up to 6% (wt.) more nickel, added to stabilize austenite (γ) at elevated temperatures while avoiding the formation of δ-ferrite and levels of carbon reduced to 0.01% (wt.) to improve the weldability [7, 8].

Corrosion behavior of supermartensitic steels is depends on the present metallurgical phases like retained austenite and delta ferrite, being demonstrated that the breakdown potential increases with the increase of retained austenite content [9]. Heat-treated microstructure of SMSS at room temperature is characterized by the tempered lath martensite and reverse austenite finely dispersed between martensite laths promoting a high strength, toughness, and corrosion resistance [10]. On the other hand, the precipitation of chromium nitrides or carbites promoted by the presence of delta ferrite is deleterious to the corrosion resistence of the alloy [9].

The scanning vibrating electrode technique have been used to elucidate corrosion mechanisms on alloy surfaces allowing the identification of preferential pit nucleation sites and the evaluation of pit currents at OCP conditions or under polarization [11-16]. In this context, the objective of this work is to evaluate the corrosion resistance of a supermartensitic steel produced for application in the oil and gas industries as an alternative to the duplex steels in chloride enviroments by using SVET technique.

Materials and Methods

The chemical composition of the investigated supermartensitic stainless steel is shown in Table 1. Supermartensitic steel was developed for application in oil and gas industry. The samples were extracted from seamless stainless steel tube and were water quenched after austenitizing at 1000°C for 30 min. In order to produce different microstructures, the samples were tempered at different temperatures and followed by air cooled as shown in Table 2. Vickers microhardness testing was performed in samples using a load of 2.94 N (300 gf) and the average hardness value of supermartensitic steel also is shown in Table 2.

Table 1: Chemical composition of the supermartensitic stainless steel from SENAI-CETEF/Itaúna.

Element	C	Cr	Ni	Mo	Si	Mn	P	S	N	Al	Ti
Content (wt%)	<0.01	12.2	5.63	1.86	0.21	0.52	0.023	0.004	0.026	0.015	0.17

Table 2: Sample identification and heat treatments conditions.

Sample identification	Heat treatments	Vickers Hardness (HV 300gf)
T (as-quenched)	1000°C 30 min, water quenched	275.43±2.36
T1	600°C 30 min, air cooled	274.57±10.22
T2	640°C 30 min, air cooled	260.77±9.43

The samples were subjected to the standard grinding and polishing techniques for microstructure characterization. The samples were grinded with sandpaper grain size of 240, 320, 400, 600, 1200 grid SiC paper and with a 1/4 μm diamond suspension, etching with Vilella's reagent (1 g picric acid + 4 mL HCl + 96 mL ethanol) immersed for 15s.

A Tecnai G2-20 - SuperTwin FEI - 200kV transmission electron microscope (TEM) was used for identification of the precipitates. The microstructure was characterized using different techniques. The phase transformation was investigated by image analysis using Olympus optical microscope and by using a Quanta FEG 3D FEI scanning electron microscope (SEM) with an Bruker XFlash 4.0 energy dispersive X-ray spectrometer (EDS) coupled.

The phases without heat treatment were identified by using X-Ray diffraction (XRD) and a SHIMADZU X-ray diffractometer with a copper tube at room temperature with an accelerating voltage of 30 kV. The interval between each acquisition was 0.05° and the step time was 3 s.

Mössbauer Spectroscopy (MS)

Conversion electron Mössbauer spectroscopy (CEMS) analyses were used to identify and quantify the martensite and the retained austenite phases. These analyses were performed with a constant acceleration in the CEMS setup mode, using a ~80 mCi ^{57}Co source in Rh matrix, at room temperature. The gamma ray-detector was a proportional counter with a flowing gas composed of a work mixture of 95% He and 5% CH_4. The collected data were numerically fitted with the NORMOS 90® computer program [17]. These results were analyzed basing mainly on the isomer shift (δ) values, which is a spectrometric parameter that reflects the s-electron density at the ^{57}Fe nucleus, providing clues about the: (i) oxidation state of iron composing the sample; (ii) electronegativity of the ligands and (iii) electronic configuration. These isomer shift values are relative to the natural Fe (αFe) [18]: The isomer shift is spectrometrically taken as the distance between the centroid of the spectrum for the sample and the zero velocity of the scale set from the αFe spectrum at the same experimental conditions; the positive velocity corresponds to the source moving toward the absorber [19]. The obtained 298 K-Mössbauer spectra are plotted as the relative transmission of gamma rays versus the Doppler velocity of the radioactive source.

Electron back-scatter diffraction (EBSD) measurements

The EBSD maps of representative samples were obtained using a FEI QUANTA 650 microscope coupled with the Nordlys HKL Fast Acquisition EBSD system operated at 20 kV and a 0.5 μm step size. For EBSD, a suspension of colloidal silica particles was used for final polishing.

Grain boundaries were determined as the boundaries with misorientation larger than 15°. A grain was defined as a region completely surround by the boundaries defined previously (>15°) [20, 21]. The data processing was carried out using the software HKL Channel 5. These measures were performed at the Brazilian Nanotechnology National Laboratory (LNNano/CNPEM).

Electrochemical SVET

The distribution of anodic and cathodic currents on the steel surface was evaluated with current density maps acquired on the supermartensitic stainless steel sample exposed to 0.1 mol/L NaCl aqueous solution at OCP using an Applicable Electronics SVET assembly. For this, a Pt/Ir microelectrode with a diameter of circa 10 µm vibrated with amplitude of 10 µm at a distance of 50 µm from the sample surface in an attached barnacle electrochemical cell with a volume of approximately 0.5 mL, as shown in Fig. 1.
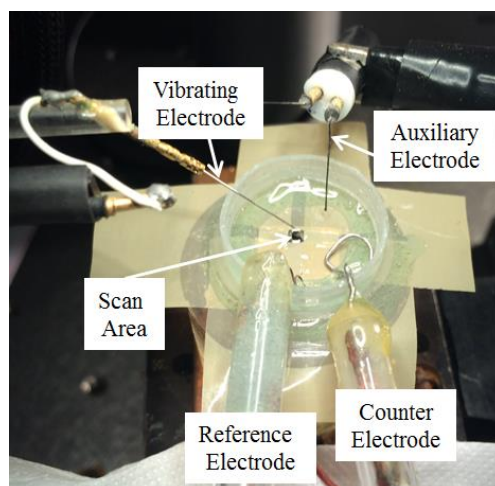
Fig. 1: Overview setup for acquisition of SVET i-maps.

Measuring window (active area) was delimited using a commercial scotch tape (3M) and plastic welding (Poxipol). Measurements of open circuit potential (OCP) were performed for the supermartensitic stainless steel samples with a conventional three-electrode cell, Ag/AgCl (saturated KCl) as a reference electrode and a Pt mesh was used as the counter electrode. The tests were performed at room temperature. The entire acquisition process of all i-maps took approximately 86400s.

Cyclic polarization

Cyclic polarization testing was performed using an Autolab PGSTAT 100N potentiostat. A conventional three-electrode cell was used. The working electrodes were the supermartensitic stainless steel samples with an exposed surface of approximately 1 cm^2. The reference electrode was Ag/AgCl (saturated KCl) and the counter electrode a Pt mesh. The electrochemical tests were performed at room temperature with three replicates.

The open circuit potential (OCP) measurements in a 0.1 mol/L NaCl aqueous solution was performed for 3600s. The cyclic polarization curves were obtained at a fixed scan rate (1 mV/s and 10mV/s) from -30 mV below the observed open circuit potential. The experiments stopped when the current reached $1mA/cm^2$. The measurements were performed in three replicates.

Results and discussion

Microstructure analysis

The microstructures of the supermartensitic stainless steel sample in the as-quenched condition and after tempering at 600°C and 640°C are shown in Fig. 2, Fig. 3, and Fig. 4, respectively. The lath martensite (M) formed in these steels. It is also possible to identify for all heat treated conditions coarse cuboidal TiN particles that form upon solidification of the steel as show in the Figs. 2, 3, 4.
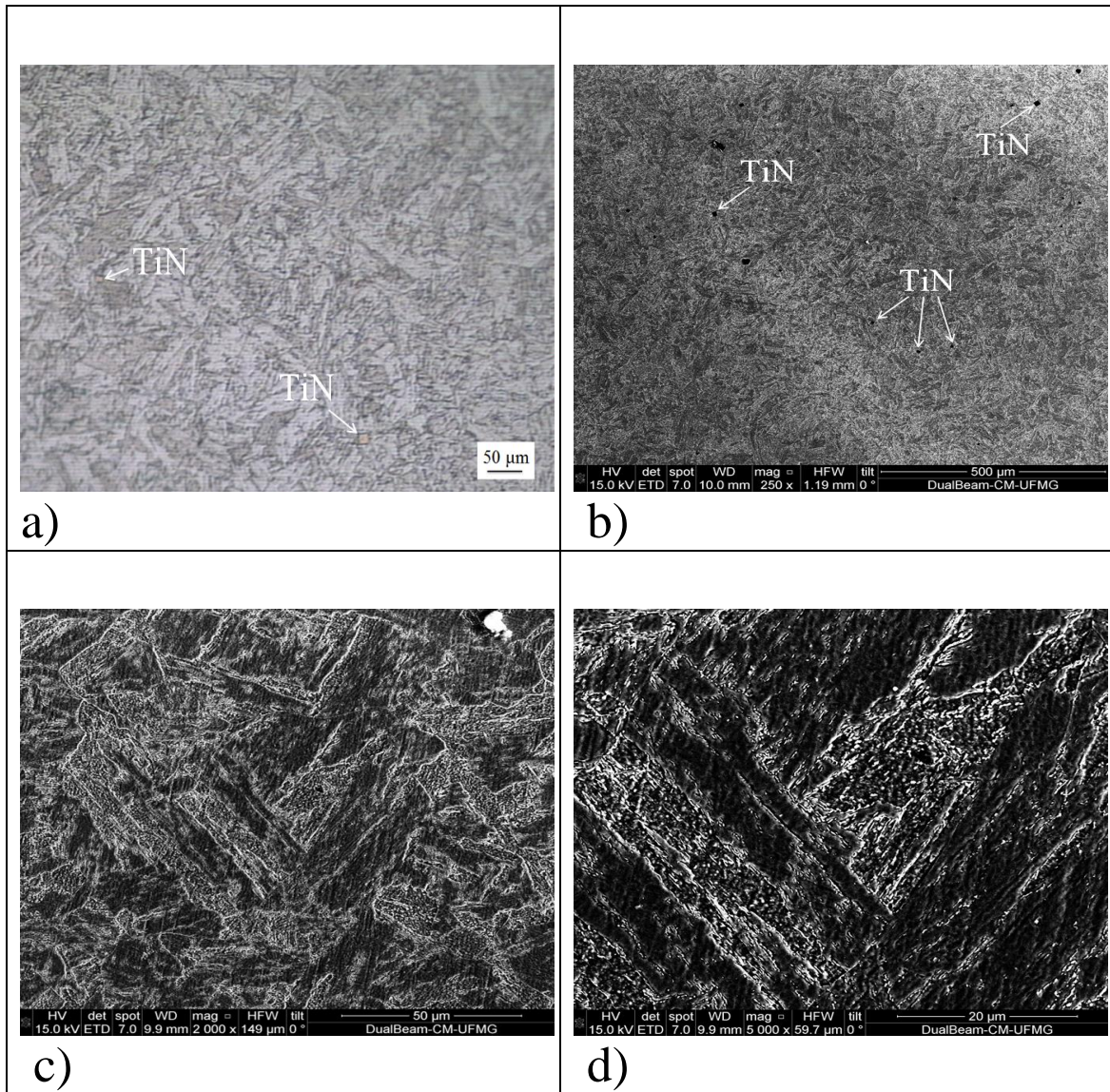
Fig. 2: Microstructure of the T sample: a) Optical micrograph with 200X magnification and b, c, d) SEM micrograph with 250X, 2000X and 5000X magnifications, respectively. TiN: titanium nitride.
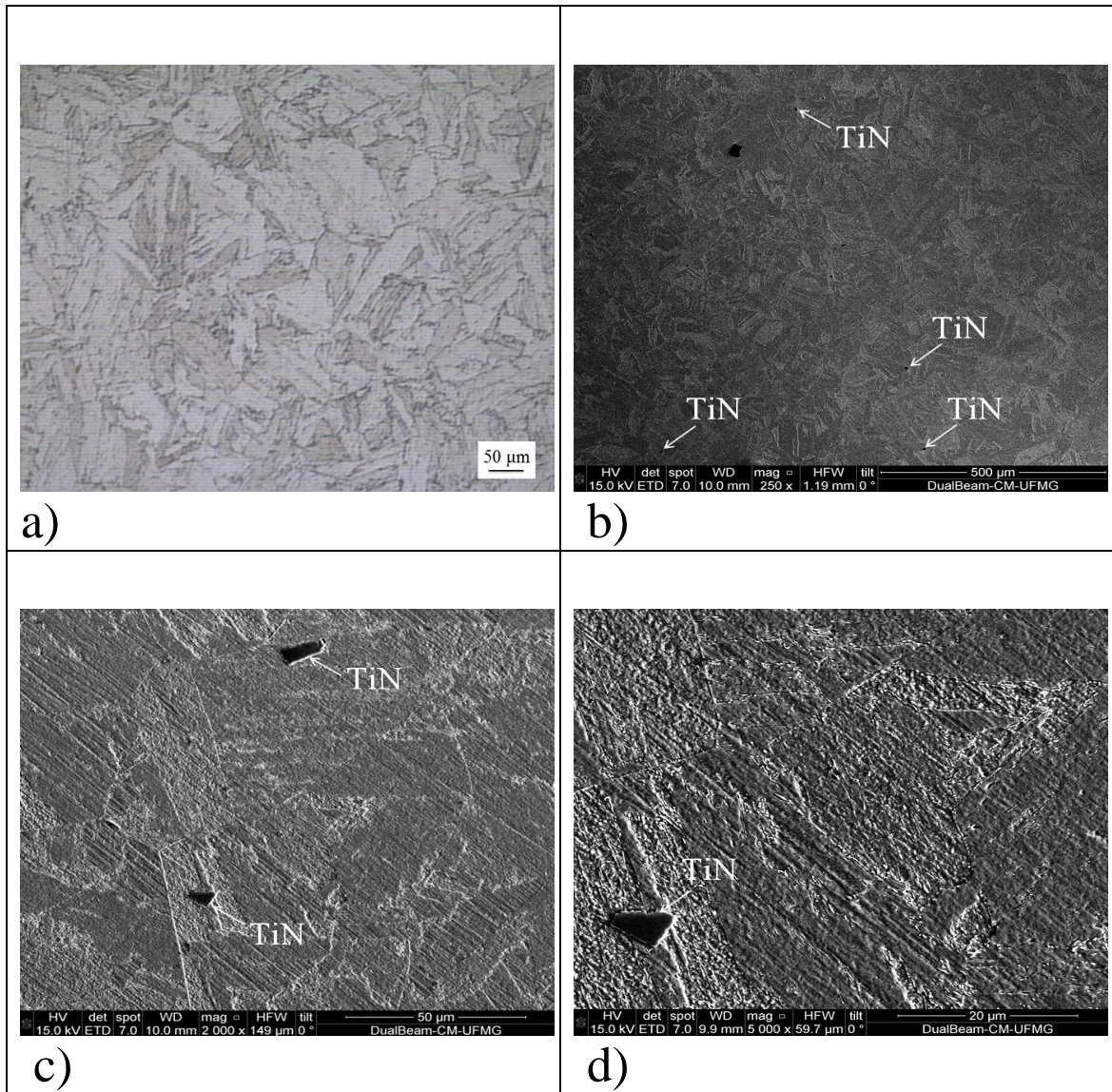
Fig. 3: Microstructure of the T1 sample: a) Optical micrograph with 200X magnification and b, c, d) SEM micrograph with 250X, 2000X and 5000X magnifications, respectively. TiN: titanium nitride.
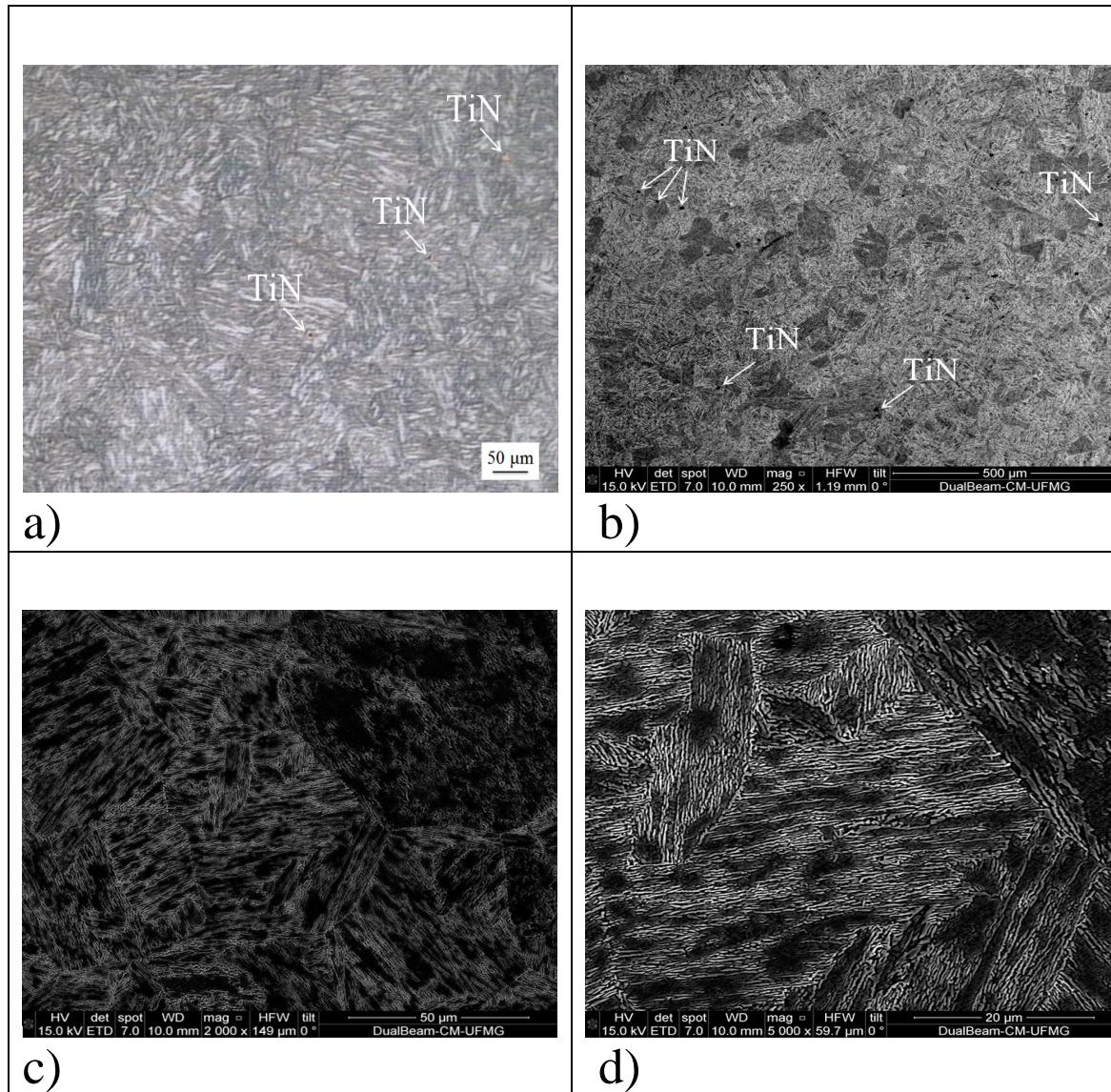
Fig. 4: Microstructure of the T2 sample: a) Optical micrograph with 200X magnifications and b, c, d) SEM micrograph with 250X, 2000X and 5000X magnifications, respectively. TiN: titanium nitride.

Fig. 5 shows the SEM micrographs (Fig. 5 (a, c, e)) of three different TiN inclusions for the supermartensitic steel and the respective EDS mapping (Fig. 5 (b, d, f)).

In this steel containing about 0.15 wt.% Ti (Table 1). The EDS analysis (Fig. 5 (b, d, f)) detected simultaneously titanium, nitrogen and carbon in inclusions which were thus identified as TiN. The formation of TiN type inclusions in Cr–Ni–Fe based alloys is inevitable because of the addition of Ti [22, 23].
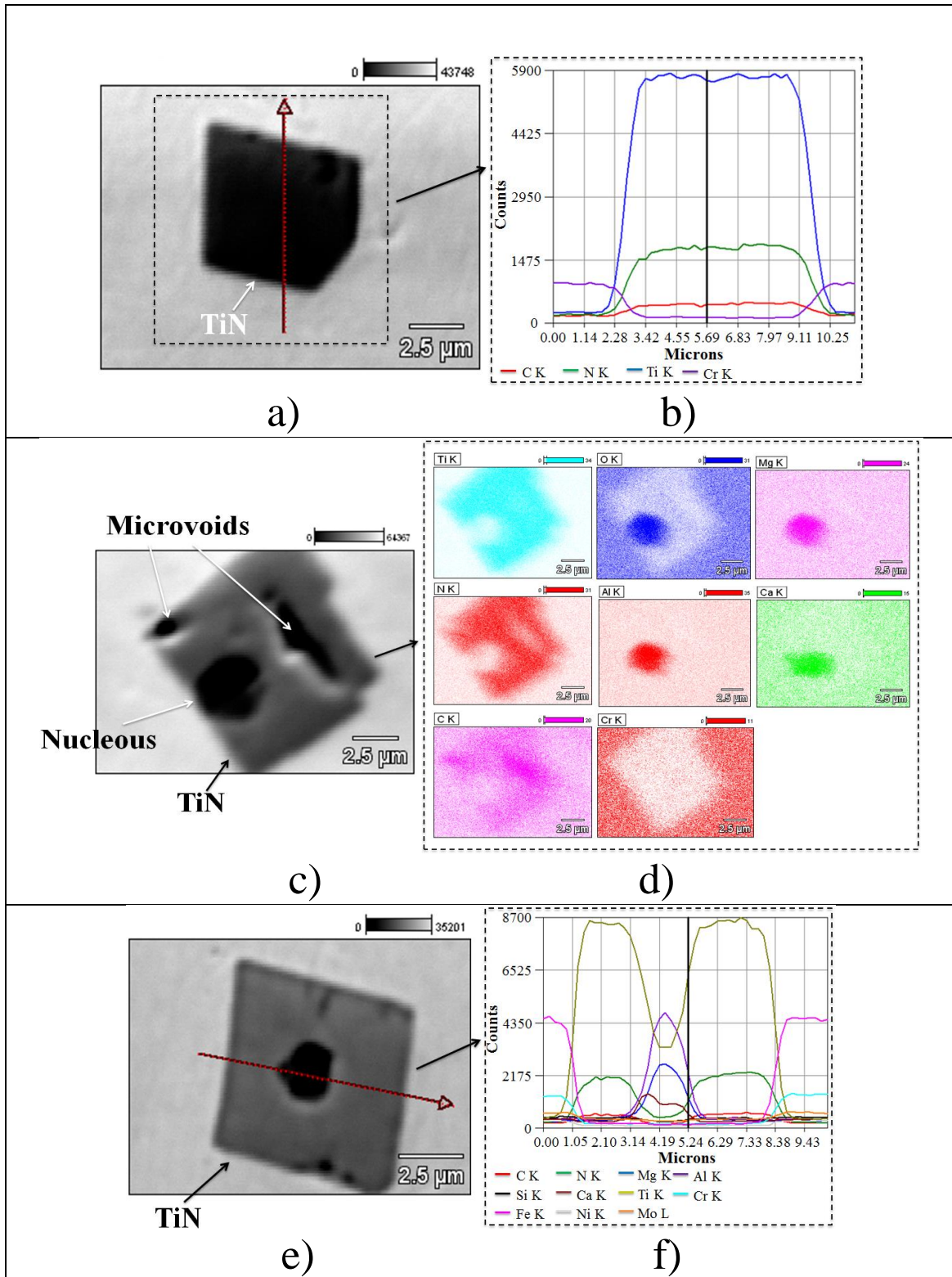
Fig. 5: SEM micrographs (a, c, e) of TiN inclusion for supermartensitic steel and EDS mapping (b, d, f).

These TiN inclusions are observed to have a cubic or rectangular shape as shown in Fig. 5 (a, c, e). Some TiN inclusions contained a nucleous (Fig. 5 (c, e)). The EDS analysis of the inclusion nucleus (Fig. 5 (d, f)) showed a high concentration of magnesium, calcium and aluminum inside the nucleous. The nucleus of the TiN type inclusion is a mixture of magnesium oxide (MgO) calcium oxide (CaO) and aluminum oxide (Al_2O_3). According literature [23, 24], the MgO and Al_2O_3 refractory material are picked up during melting of the 690 alloy and acted as seeds for the formation of TiN type inclusions during the solidification process.

Some TiN inclusions contained microvoids or fractures as shown in Fig. 5 (c). Hur et al. [24] have shown that microvoids between Ti precipitates decrease the corrosion resistance of Ni–Cr–Fe alloys.

Lian et al. [25] studied the effect of titanium content on the microstructure and mechanical properties of supermartensitic stainless steel. They reported that the Ti addition to a supermartensitic stainless steel promotes a microstructural refinement, with a decrease of the prior austenite grain size and lath martensite width.

According Lian et al. [25] Ti possesses a higher carbon and nitride affinity than Cr, therefore, for a given titanium content, all of the carbon and nitrogen can precipitate as titanium carbonitrides to prevent chromium carbide precipitation. The authors also described that the microaddition of 0.2 Ti (wt.%) suppressed the formation of Cr-rich carbides by forming stable Ti(C, N) which retards the formation of the reversed austenite and enhances strength without severe decrease in toughness. And the microaddition of 0.5 Ti (wt.%) leads to the nano-intermetallic precipitation of Ni_3Ti

instead of titanium carbonitrides in supermartensitic stainless steels after tempering at 600°C for 4 h. The Ni_3Ti precipitate has a hexagonal crystal structure and averaged approximately 5 nm in diameter and 20 nm long. These nano-precipitates produced a hardening that increased the tensile strength and decreased the toughness of steel.

According Carrouge [26], the excessive Ti additions lead to the precipitation of intermetallic compounds such as TiNi instead of Ti (C, N). Rodrigues et al. [6], evaluated the effect of addition of 0.13 Ti (wt.%) in a 12.5 Cr-5.4 Ni-2.09 Mo (wt.%) supermartensitic stainless steel. According Carrouge [26] the addition of 0.13 Ti (wt.%) after a selected heat treatment produced a very fine refined microstructure composed of martensite matrix with nanometer size particles of titanium carbonitride (Ti (C, N) - 70 nm), which was responsible for the improved mechanical property.

After heat-treatment all samples had similar hardness (as-quenched - 275.43±2.36 HV, 600°C - 274.57±10.22 HV and 640°C - 260.77±9.43 HV).

X-ray diffraction

Fig. 6 shows the X-ray diffraction patterns for the as-quenched and tempered conditions of the investigated supermartensitic stainless steel. The Miller indices corresponding to martensite and retained austenite are indicated in Fig. 6. Low intensity austenite peaks and high intensity martensite peaks were observed for all conditions, as shown in Fig. 6. The (111), (200), (220), and (311) austenite diffraction peaks had low intensity when compared to the martensite peaks for all conditions. The amount of the retained austenite phase was too low, so the technique was not sensitive enough to quantify the volume fraction of retained austenite in this steel samples.
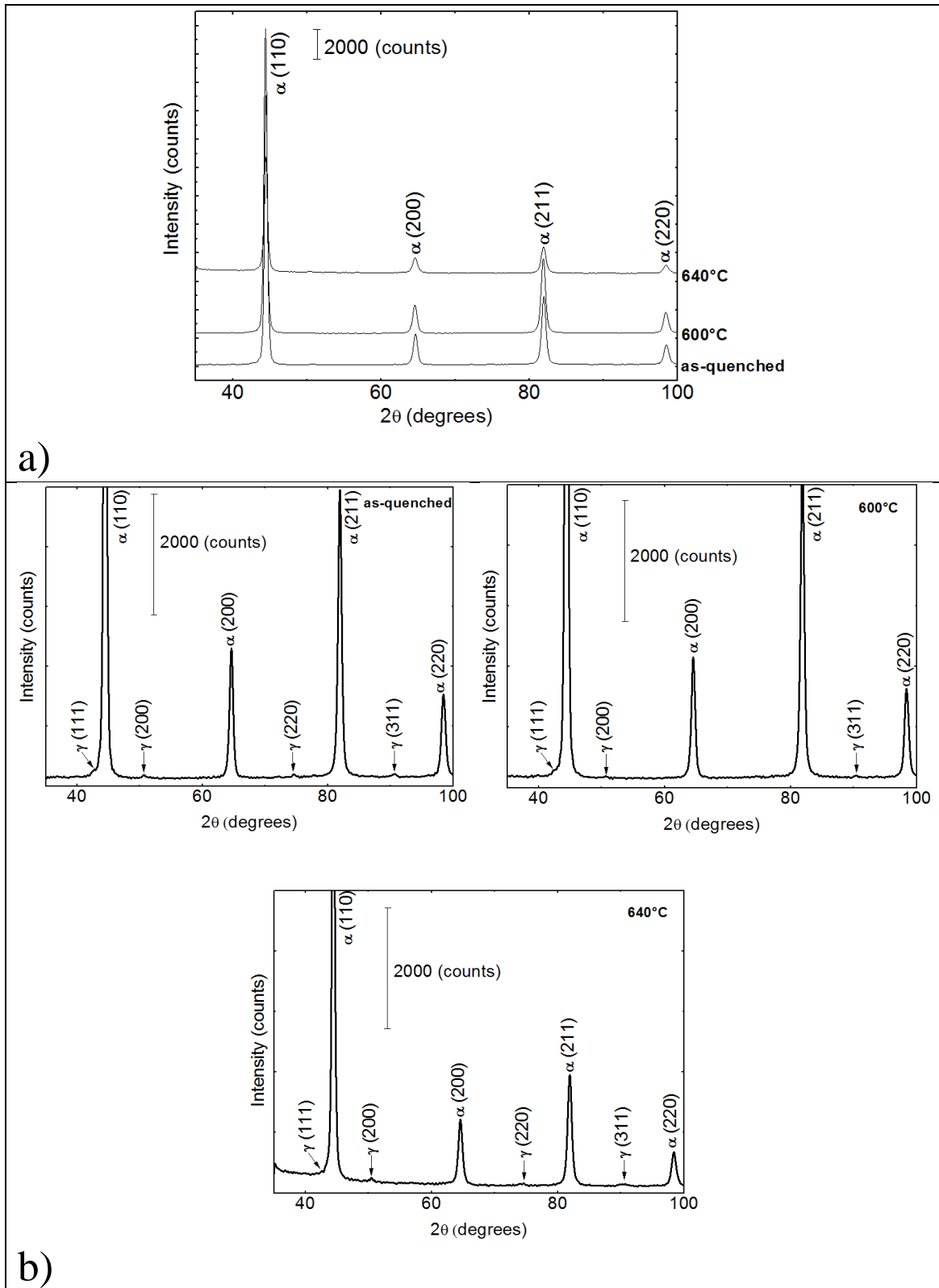
Fig. 6: X-Ray diffraction of the supermartensitic steel: a) as-quenched (T), tempering at 600°C during 30 min (T1) and tempering at 640°C at 30 min (T2). b) Magnification of T, T1 and T2 sample results.

Mössbauer Spectroscopy (MS)

According to Solomon and Levinson [19] a Mössbauer spectrum results from the resonant absorption of 14.4 keV γ-rays by the ^{57}Fe iron nuclei. When these nuclei are in a ferromagnetic arrangement, as in the case of the αFe below the Curie point, a six-line absorption pattern is observed. However, if the ^{57}Fe nucleus in the αFe is in a paramagnetic state, then a single paramagnetic resonant line will be observed. For any sample, if a paramagnetic ^{57}Fe occurs in the sample along with the magnetically ordered αFe phase, the corresponding spectrum will be the superposition of six-peak ferromagnetic spectrum with the single-line paramagnetic spectrum.

The Mössbauer spectroscopy results for the T, T1 and T2 samples are shown in Table 3 and Fig. 7. The Mössbauer spectra showed the existence of at least two chemical environments which are associated with iron site with different neighborhoods. The chemical environment where the ^{57}Fe atoms are surrounded mostly by other ^{57}Fe atoms have higher hyperfine fields, characterized in the figure by the set of sextet (gray lines), with hyperfine parameters typical of the alpha phase (α) magnetic (martensitic) with 99.1% of the spectral areas. And another chemical environment was identified, characterized by a singlet (red line), with a range of parameters typical of the hyperfine phase (γ) (austenitic) non-magnetic, with less than 1% of the spectral area.

The Mössbauer spectroscopy results for the T, T1 and T2 samples showed that less than 1% of the iron present in the material is in the form of austenitic phase.

Table 3: Mössbauer Spectroscopy results for T, T1 and T2 samples.

Samples	Phase Identification	Isomeric shift δ ($\pm0{,}05$) mm/s	H_{HF} ($\pm0{,}5$) Tesla	Phase (±0.5) %
T	α	-0.01	<28.0>	99.3
	γ	-0.09	-	0.7
T1	α	-0.01	<27.9>	99.5
	γ	-0.09	-	0.5
T2	α	-0.01	<27.1>	99.1
	γ	-0.09	-	0.9

Fig. 7: Mössbauer Spectroscopy results of as-quenched (T), tempering at 600°C during 30 min (T1), and tempering at 640°C during 30 min (T2) samples.

Electron back-scatter diffraction (EBSD) measurements

84

The microstructure of the supermartensitic steel samples in the as-quenched, tempered for 30 min at 600°C and tempered for 30 min at 640°C conditions was also evaluated by EBSD technique. Fig. 8 shows the misotexture of samples quenched and tempered at 600°C and 640°C. After different heat-treatments, grains showed a similar plate-like shape. According to Bilmes et al. [27], retained austenite has a plate shape when found within the martensite matrix and at prior austenite grain boundaries after tempering. The black line indicates the grain boundaries with misorientation above 15°. The prior austenite grain boundaries were found with misorientation above 15°.
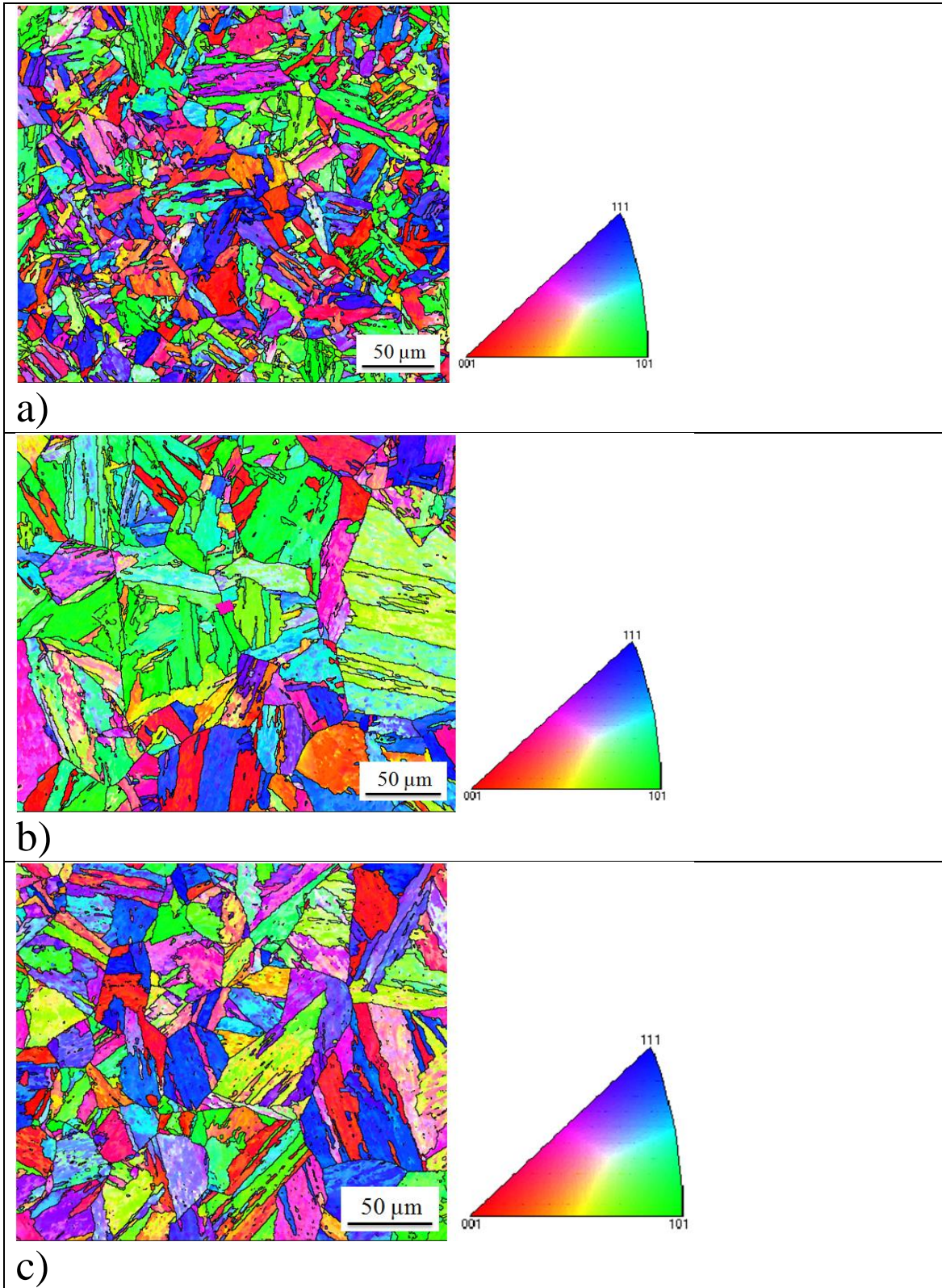
Fig. 8: Orientation image maps for the supermartensitic steel samples: a) as-quenched,

b) after tempering for 30 min at 600°C and c) after tempering for 30 min at 640°C.

Phases were identified from EBSD data for the T, T1 and T2 samples. Fig. 9 shows the phase map, where martensite grains are in red, austenite in blue, and high angle grain boundaries are marked by black lines. As expected, the martensite covered almost the entire examined surface, which means that there is no extend austenite in this microstructure. In this figures it can be observed that that retained austenite has a globular morphology and it can be most found at high angle boundaries in the martensitic matrix.
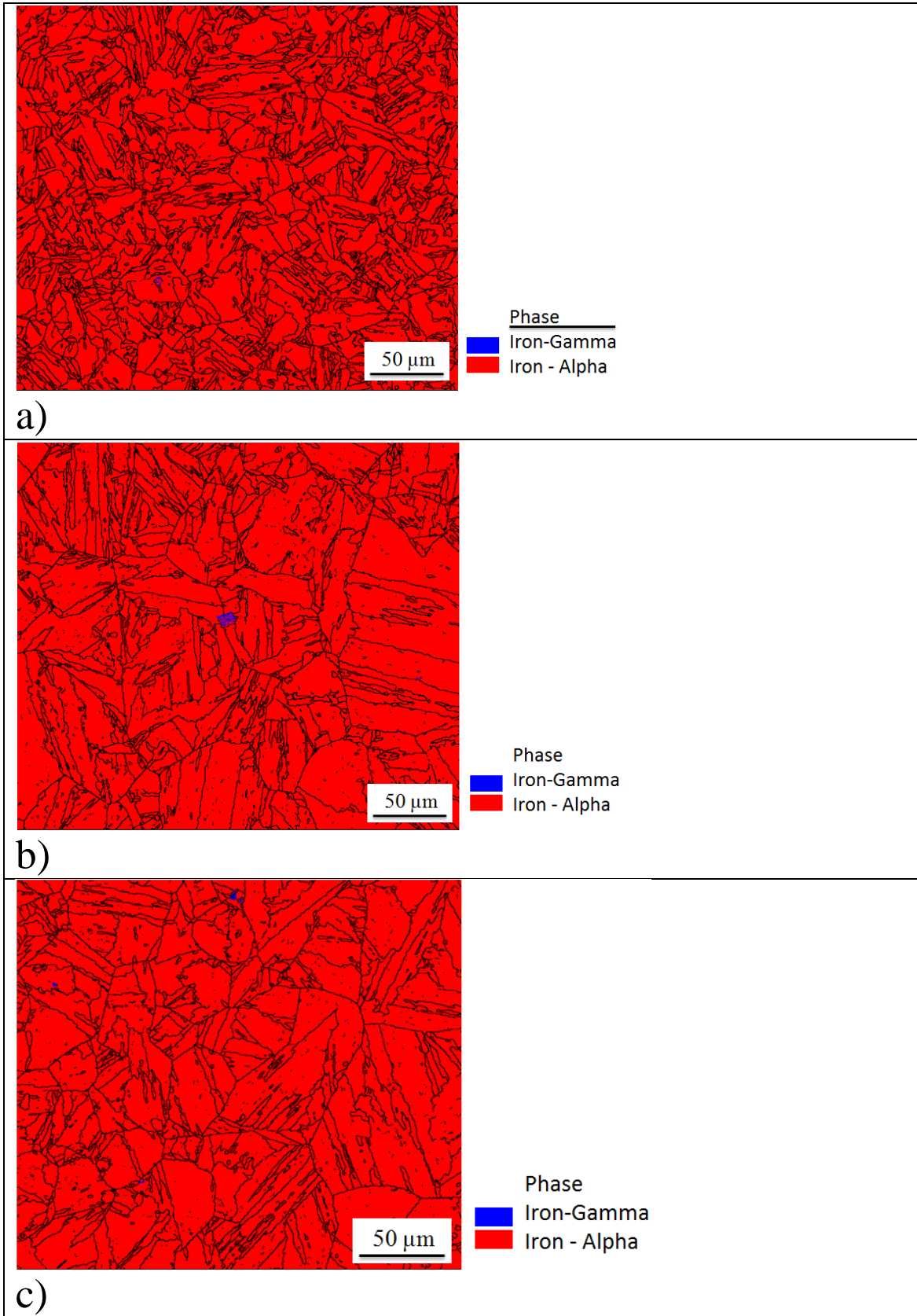
Fig. 9: EBSD phase map for the supermartensitic steel samples: a) as-quenched, b) after tempering for 30 min at 600°C and c) after tempering for 30 min at 640°C.

The grain size data collected from EBSD data for the T, T1 and T2 samples are described by the histograms shown in Figs. 10 (a, b, c), respectively. The three samples showed a marked asymmetrically behavior. This indicates that the most appropriate measurement of central tendency to evaluate the groups is the median. The descriptive data shown in Table 4, the superimposed graph of Fig. 11 (a) and Dotplot of the three groups illustrated in Fig. 11 (b) indicate that the grain size of T sample is higher that of the T1 and T2 samples and the average grain size of T2 samples appears larger than that of the T1 sample.

A statistical hypothesis testing was performed to increase the security of the decision that the T, T1 and T2 samples have different average grain sizes. The traditional ANOVA test (Test F) should not be used since the data are not normal and ANOVA is more appropriate to compare mean than median values. The appropriate test is the non-parametric method of Kruskal-Wallis (KW) assessing whether the medians of the three groups are equal. Because it is a nonparametric procedure we do not need the data normality assumption for each group. Applying the KW test, a p-value <0.001 was obtained and with a significance level of 5% (α), the hypothesis that the medians of the three groups are equal must be rejected. Complementing the evaluation with the multiple comparison test, described in literature [28], with a 5% significance level, the T group is different from T1 and T2; and the group T1 is different from T2. In this sense we can conclude, with a 5% significance level, that the average grain size of T sample > T2 median grain size > T1 median grain size.
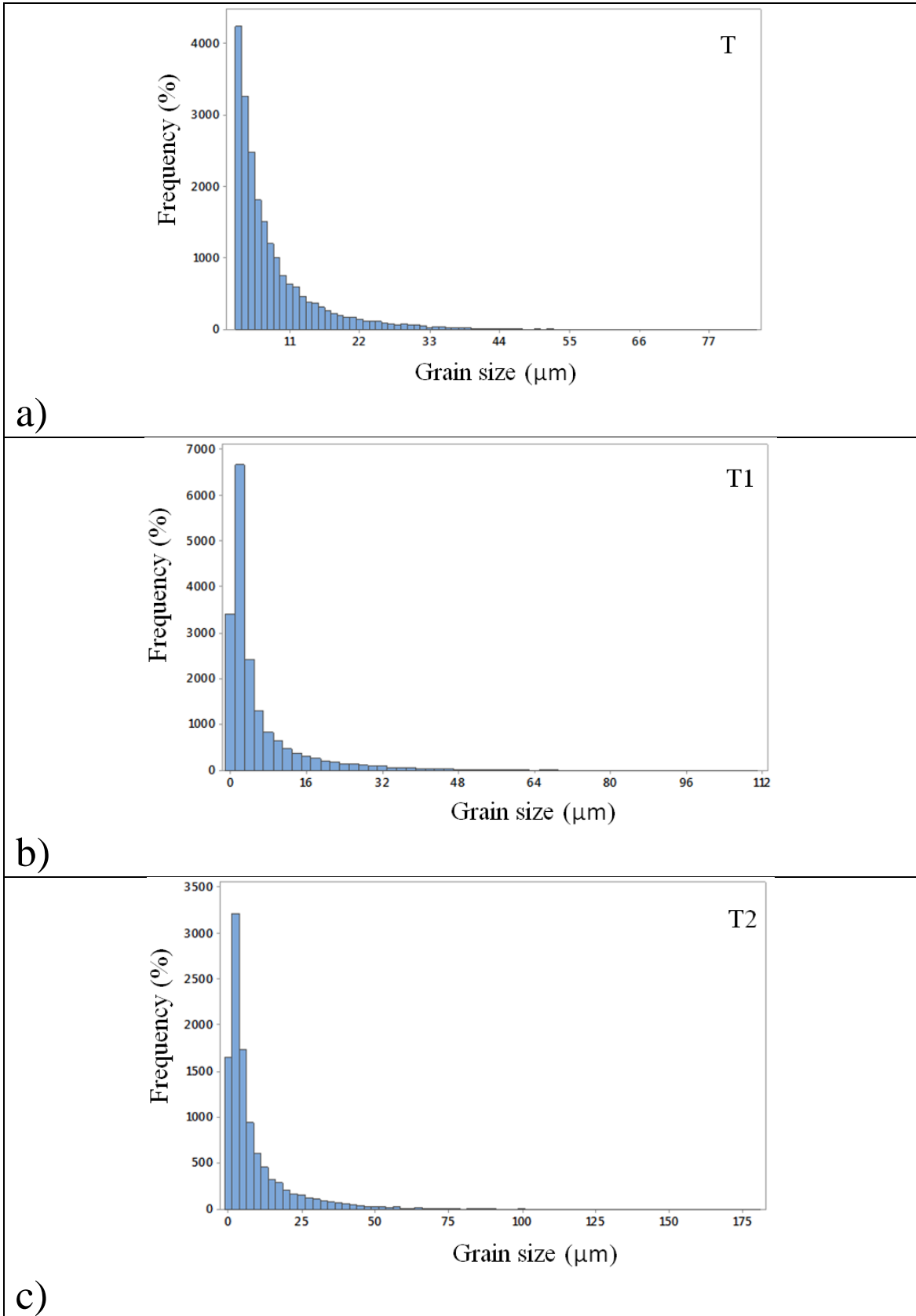
Fig. 10: Histograms of grain size distribution (µm) for the supermartensitic steel

samples: a) T, b) T1 and c) T2.
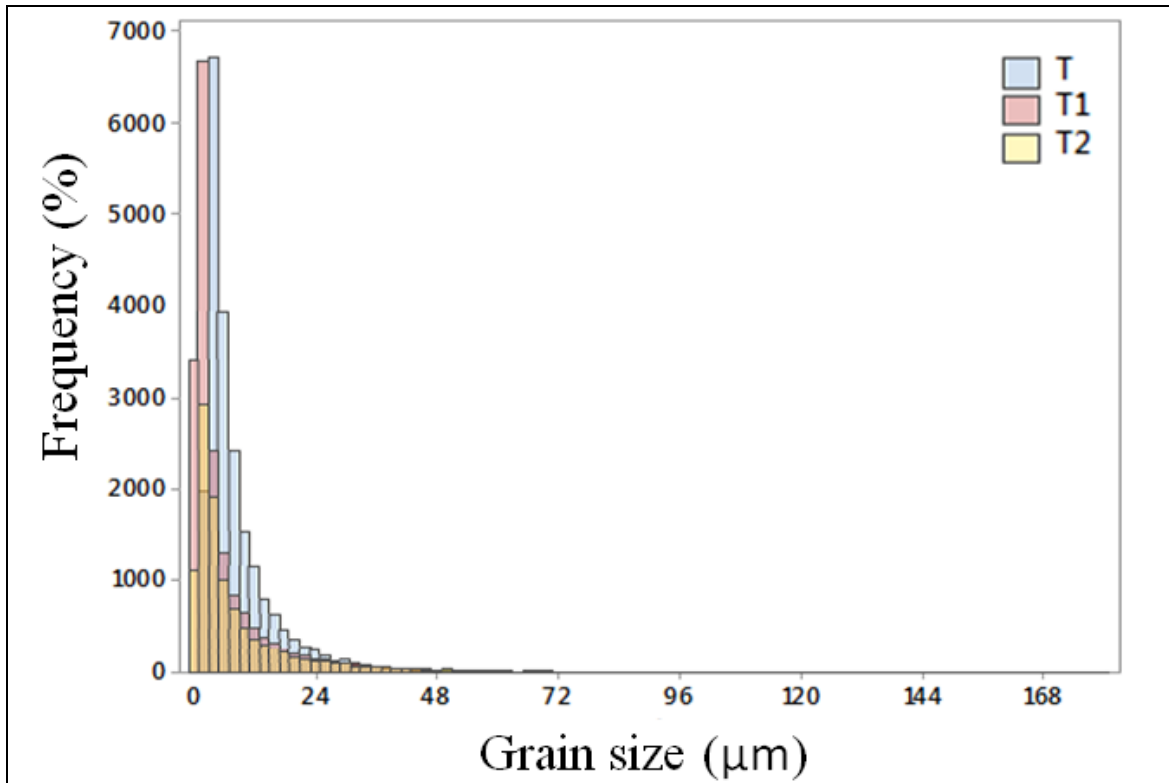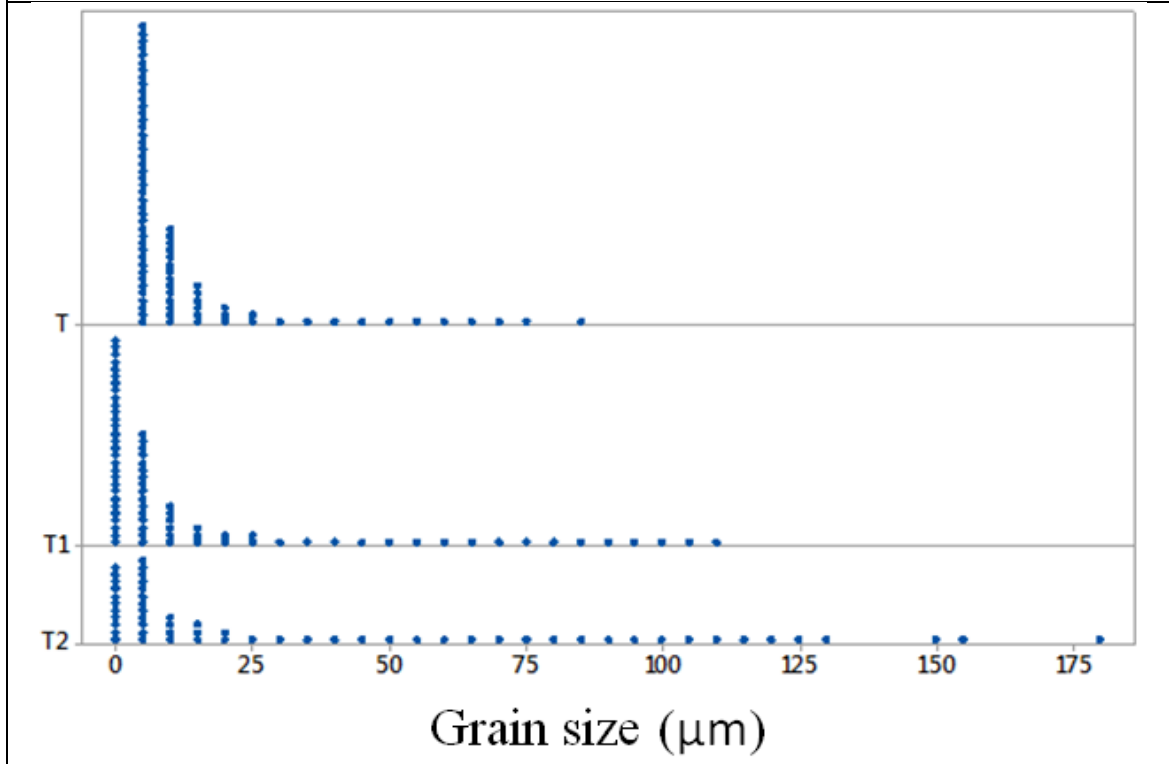
Fig. 11: Grain size distribution (µm) of the T, T1 and T2 samples: a) superimposed

graph and Dotplot.

Table 4: Descriptive statistics of grain size data collected from EBSD data for T, T1 and T2 samples.

Samples	Mean	Median	Minimun	Maximum
T	8.485±7.318	5.863	2.676	83.538
T1	6.508±10.210	2.539	0.846	110.980
T2	9.174±13.154	4.231	0.846	179.440

Cyclic polarization and OCP measurement

Fig. 12 shows typical cyclic polarization curves of supermartensitic stainless steel samples that showed the initiation and propagation of pitting corrosion during the forward scan and a repassivation during the reverse scan. Anodic dissolution and oxide formation prior to pitting process corresponds basically to dissolution in the passive state and can also be observed in Fig. 12. Table 5 shows the electrochemical parameters obtained using cyclic polarization tests.

Cyclic polarization curves also show that the T1 sample is more resistant to initiation and propagation of localized corrosion than T and T2 samples, since T1 sample exhibited nobler breakdown potential (E_b) values (Table 5). Moreover, T1 sample reveals enhanced repassivation ability, as compared with T and T2 samples, resulting in repassivation potential (E_R) shifted in the noble direction.

Representative curves of the OCP evolution with the immersion time for the T2 sample are presented in Fig. 13. Transient currents may be observed for the T2 sample, which are indicative of a pitting process.
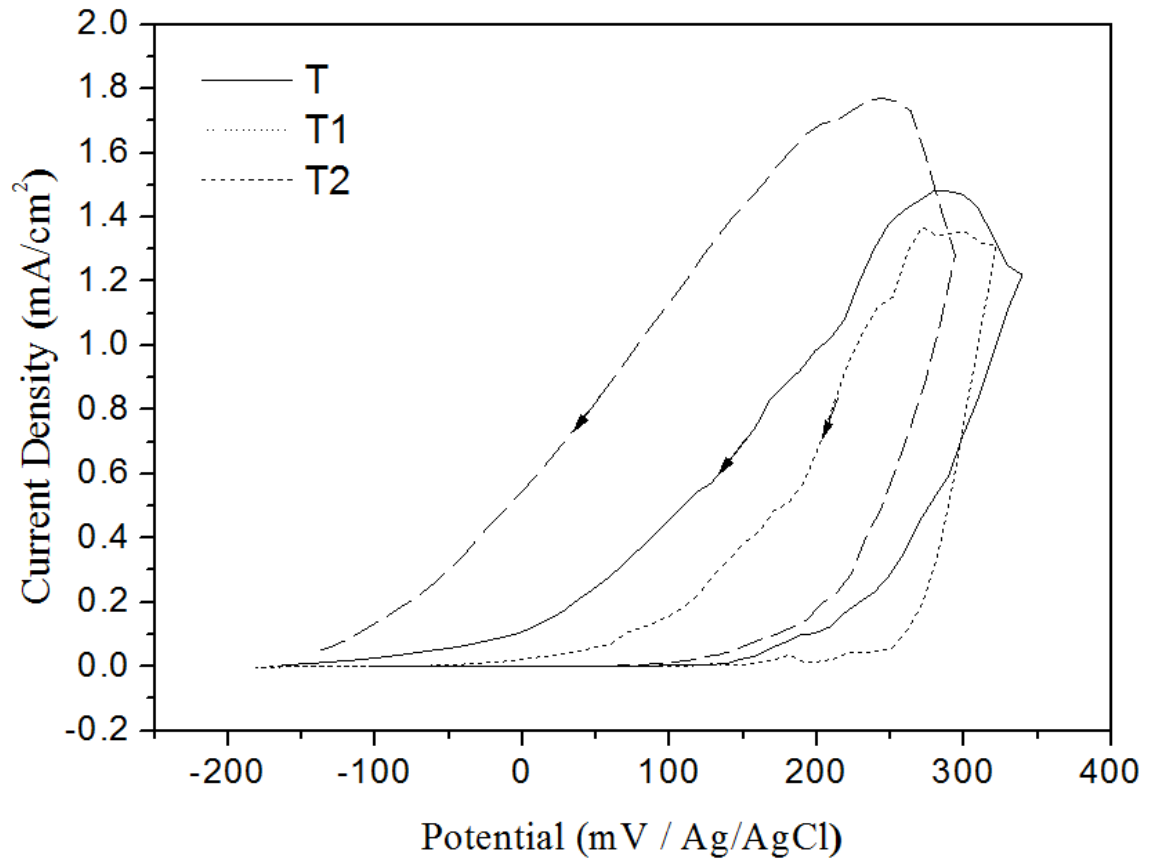
Fig. 12: Cyclic polarization curves of T, T1 and T2 samples in 0.1 mol/L NaCl aqueous solution at 1 mV/s.

Table 5: Electrochemical parameters obtained using cyclic polarization in 0.1 mol/L NaCl aqueous solution.

Samples	E_b mV(Ag/AgCl)	E_R mV(Ag/AgCl)
T	134.29±11.30	-153.96±8.37
T1	255.10±18.55	-54.82±0.46
T2	93.31±3.86	-
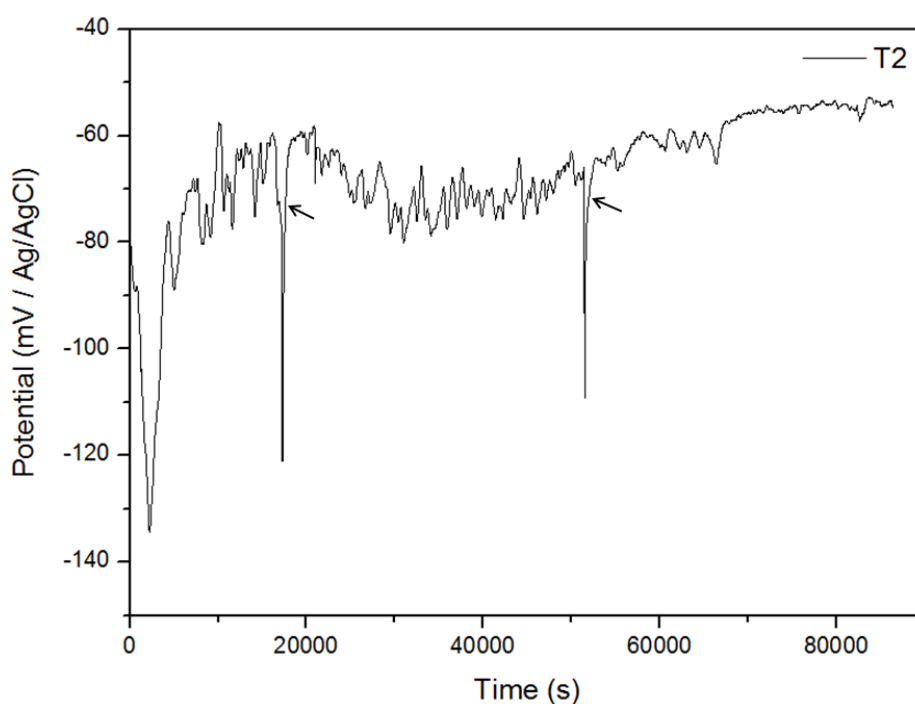
Fig. 13: OCP of T2 sample acquired during 86400s in 0.1 mol/L NaCl aqueous solution.

Electrochemical SVET

The SVET maps obtained for the T2 sample after 3600s and after 86400s of immersion in a 0.1M NaCl solution, as well as the optical image of the respective surface after the immersion are shown in Figs. 14.

The T2 sample showed no activity after immersion in a 0.1M NaCl solution, after 3600s. However, after the 86400s of immersion in a saline solution, a pit has developed. The optical image of T2 sample showed that the anodic sites on the steel surface have developed around the TiN particles (Figs. 15, 16).

The SEM micrograph and EDS concentration maps of the T2 sample after SVET measurement are shown in Fig. 16, where a localized corrosion around the TiN particles may be observed, as those recorded in the SVET experiments. The EDS concentration maps showed that these precipitates are enriched in Ti, C and N, compared to the steel matrix.

The TiN inclusions, as non metallic particles, hardly dissolve in high-temperature water due to their excellent electrochemical stability and usually behave as cathodes under corrosive environments [29, 30]. In contrast, Al_2O_3 and/or MgO are not thermodynamically stable because their free potentials are lower than that of the matrix [31]. It has been observed that large, faceted titanium nitride inclusions, which have a hexagonal crystal structure, can act as passive film breakdown sites in the alloy 690, and that they can also provide preferential sites for pit initiation in an acidic chloride environment [23].

Hur et al. [24] showed that the microvoids between the fragments of broken Ti-carbonitrides accelerated pitting corrosion around the inclusion. Even the exposed TiN stringer without microvoids still acts as a cathode to benefit the localized corrosion at the inclusion/matrix interface.

According to Dutta et al [22], faceted titanium nitride particles in Alloy 800 may provide preferred sites for pit initiation in the chloride environments. The presence of large, faceted titanium nitride particles in Alloy 800 has been found to be more detrimental than the small, spherical-shaped titanium carbide particles as far as the surface-related localized corrosion resistance of the alloy in the chloride environments. Theories for passive film breakdown and pit initiation have been summarized in threemain mechanisms that focus on passive film penetration, film breaking, or adsorption [32]. These three mechanisms of pit initiation are not necessarily mutually exclusive. In this study, a combination of these mechanisms is possible. According to Marcus et al. [33], the presence of microstructural defects on the samples such as metal grain boundaries or interfaces between the matrix and inclusions or second phase particles can promote local breakdown of the passive film. In this work, the breakdown of the passive film was found to be associated with the TiN.

According to Tan [34] the electrode inhomogeneity such as material impurities, metallurgical defects, inclusions, different phases, grain boundaries appears to determine the pitting nucleation stage while the electrochemical heterogeneity, that is believed to initiate from pre-existing active electrode inhomogeneity sites, appears to control the propagation stage.

It has been proposed by some authors [33, 35-37] that adsorption of aggressive anions(Cl^-) reduces the surface tension of the passive film leading to cracks, allowing anionsto reach the metal surface. Marcus et al. [33] have shown evidence for both chloride adsorption and penetration for the pitting corrosion in chloride solutions. If Cl^- ions are present in the electrolyte, they will compete with OH^- for adsorption on the

oxide surface [34, 37, 38]. Cl^- can penetrates through intergranular boundaries and migrate to the metal/oxide interface, resulting in the formation of Cl^- containing particles that will cause stress-induced fracture of the passive film due to the growth of these particles [33].
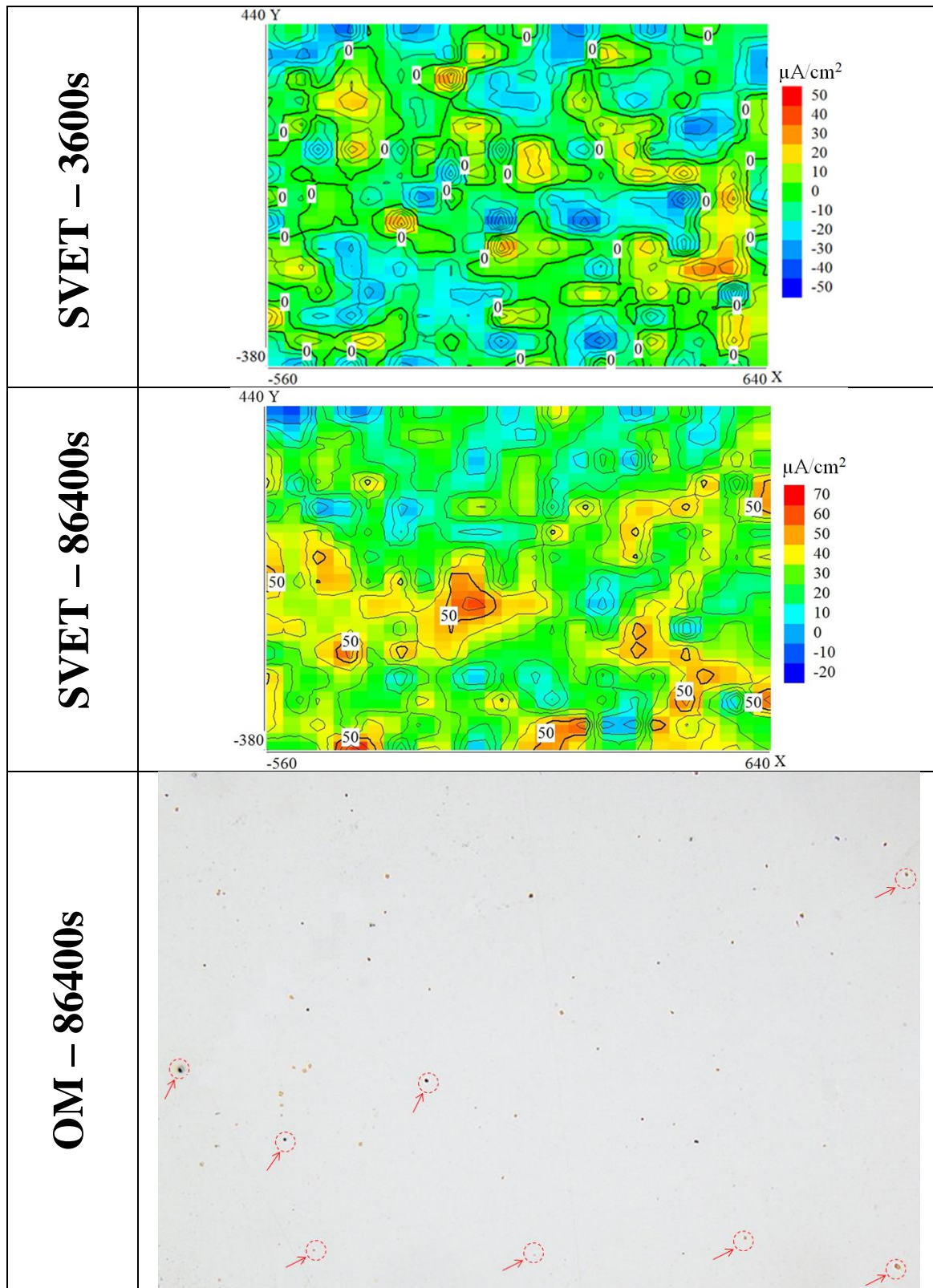
Fig. 14: SVET images and optical micrographs (OM) of T2 sample surface immersed in

0.1 mol/L NaCl. Pit locations are indicated by red circles and arrows in the

micrographs.
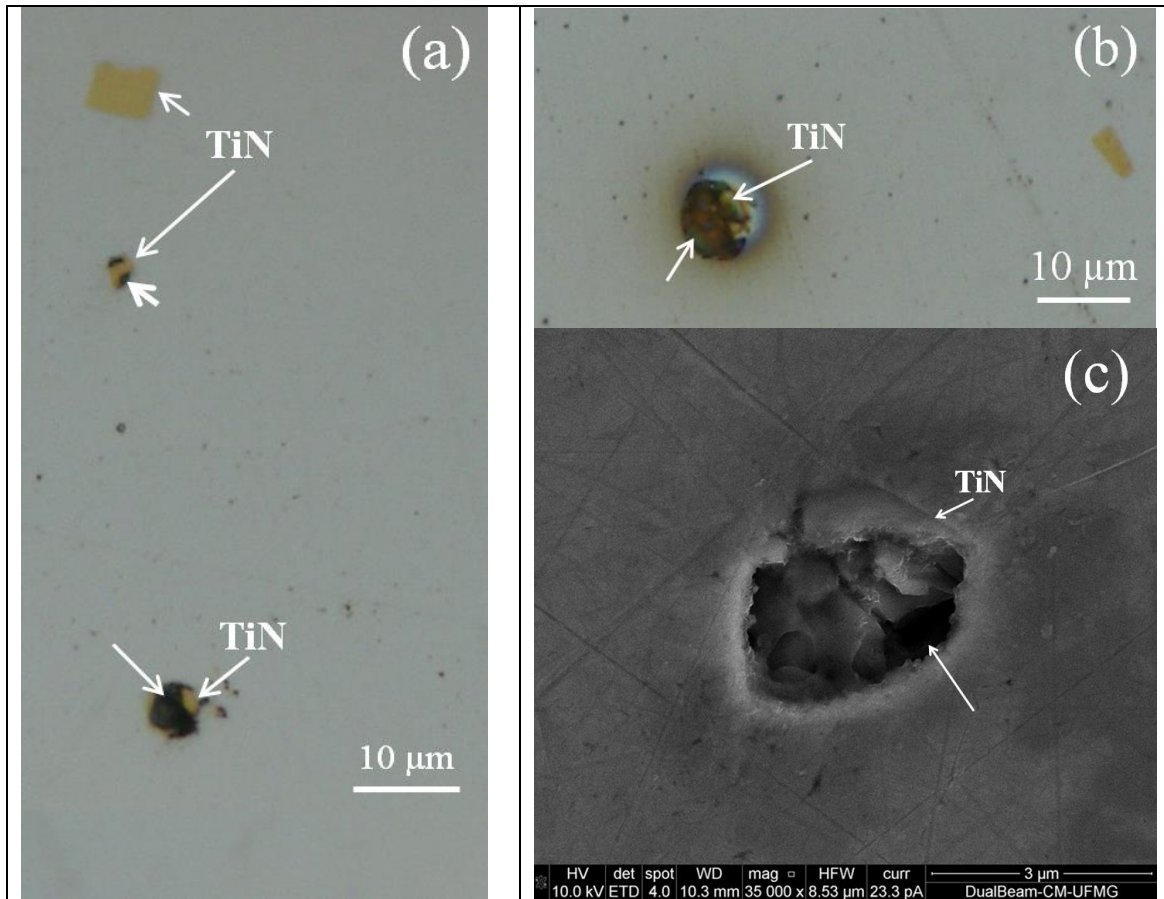
Fig. 15: Optical micrographs (a, b) and SEM images (c) of T2 sample surface immersed

in 0.1 mol/L NaCl during 86400s. Pit locations are indicated by white arrows in the

micrographs.
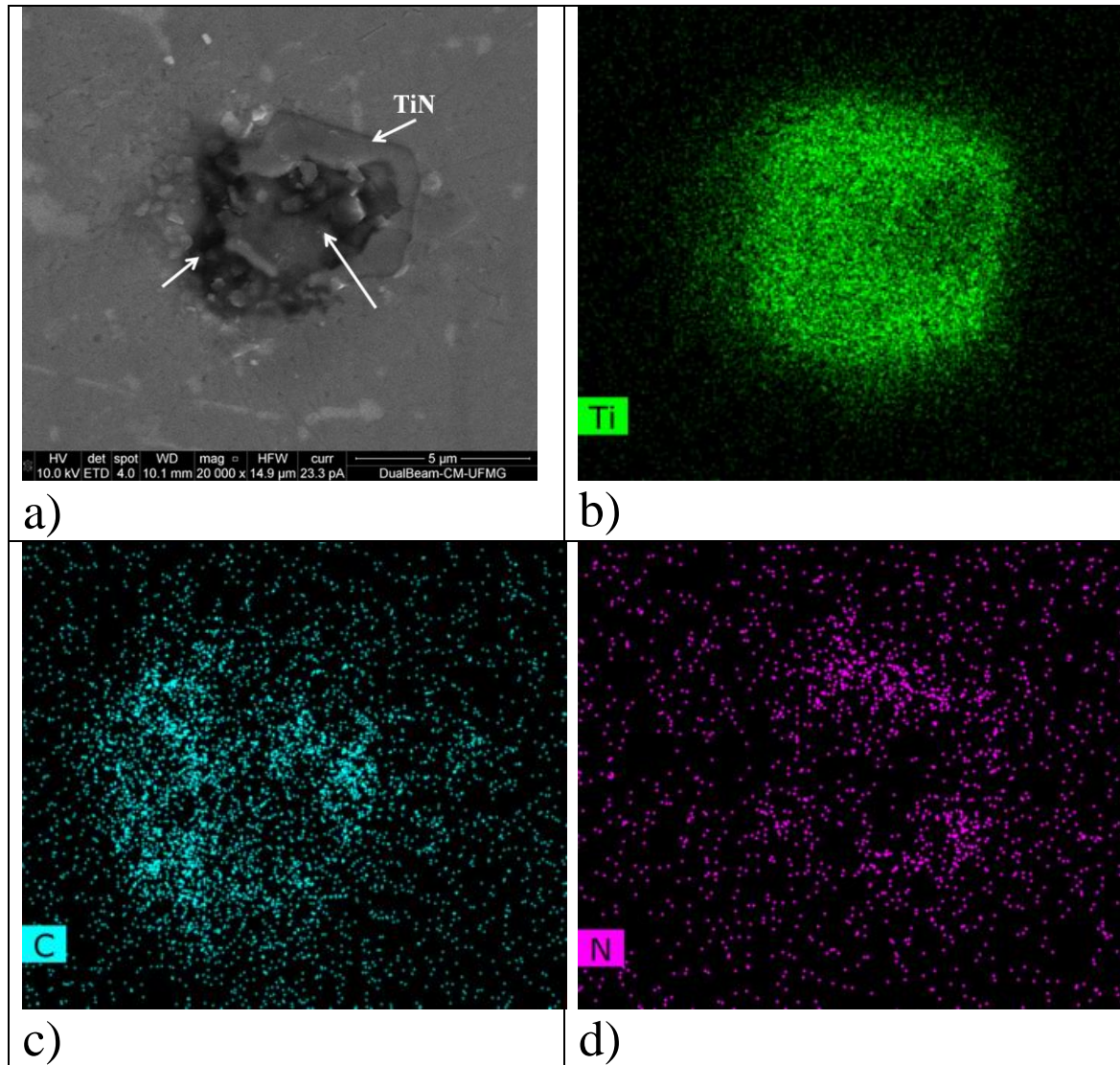
Fig. 16: SEM micrograph (a) and EDS concentration maps of the T2 sample after

SVET measurement during 86400s (b, c, d).

Conclusions

A microstructural and electrochemical analyses of SMSS submitted to austenitizing at 1000°C, water quenching, and tempering at 600°C and at 640°C and air cooled were performed. The techniques used were Mössbauer, SEM and OM, EDS, XRD, EDSD, SVET and cyclic polarization.

Coarse cuboidal TiN particles were identified on the steel surfaces of all samples. The TiN inclusions showed microvoids and a nucleous containing magnesium, aluminum and calcium oxides.

Mössbauer spectroscopy identified 0.7, 0.5 and 0.9% of retained austenite in SMSS samples as-quenched and tempered at $600^{o}C$ and $640^{o}C$, respectively.

The sample tempered at $600^{o}C$ showed the lowest grain size, evaluated by using EBSD technique, and the highest localized corrosion resistance in a saline medium. The SMSS tempered at $600^{o}C$ showed the highest breakdown and repassivation potentials among the samples studied.

The SMSS sample tempered at $640^{o}C$ showed no electrochemical activity after 3600s of immersion in a saline solution by using a SVET technique, but after 86400s, a pit was detected. SVET analysis showed the association of a localized corrosion sites with the TiN inclusion on the steel surface.

Acknowledgments

References

[1] LIU, Yu-rong, YE, Dong, YONG, Qi-long, SU, Jie, ZHAO, Kun-yu, JIANG, Wen, Effect of Cu addition on microstructure and mechanical properties of 15%Cr super martensitic stainless steel, Mater. Des. 41 (2012) 16-22.

[2] ZOU, De-ningl, HAN, Ying, ZHANG, Wei, FANG, Xu-dong, Influence of Tempering Process on Mechanical Properties of 00Cr13Ni4Mo Supermartensitic Stainless Steel, J. Iron Steel Res. Int. 17 (2010) 50-54.

[3] C.A. Della Rovere, C.R. Ribeiro, R. Silva, L.F.S. Baroni, N.G. Alcântara, S.E. Kuri, Microstructural and mechanical characterization of radial friction welded supermartensitic stainless steel joints, Mater. Sci. Eng. A 586 (2013) 86-92.

[4] X.P. Ma, L.J. Wang, C.M. Liu, S.V. Subramanian, Role of Nb in low interstitial 13Cr super martensitic stainless steel, Mater. Sci. Eng. A 528 (2011) 6812-6818.

[5] X.P. Ma, L.J. Wang, C.M. Liu, S.V. Subramanian, Microstructure and properties of 13Cr5Ni1Mo0.025Nb0.09V0.06N supermartensitic stainless steel, Mater. Sci. Eng. A 539 (2012) 271-279.

[6] C.A.D. Rodrigues, P.L.D. Lorenzo, A. Sokolowski, C.A. Barbosa, J.M.D.A. Rollo, Titanium and molybdenum content in supermartensitic stainless steel, Mater. Sci. Eng. A 460-461 (2007) 149-152.

[7] I. Calliari, M. Zanesco, M. Dabala, K. Brunelli, E. Ramous, Investigation of microstructure and properties of a Ni-Mo martensitic stainless steel, Mater. Des. 29 (2008) 246-250.

[8] T.J. Mesquita, E. Chauveau, M. Mantel, N. Bouvier, D. Kosche, Corrosion and metallurgical investigation of two supermartensitic stainless steels for oil and gas environments, Corr. Sci. 81 (2014) 152-161.

[9] M.D. Pereda, C.A. Gervasi, C.L. Llorente, P.D. Bilmes, Microelectrochemical corrosion study of super martensitic welds in chloride-containing media, Corr. Sci. 53 (2011) 3934–3941.

[10] D.-N. Zou, X.-H. Liu, Y. Han, W. Zhang, J. Li, K. Wu, Influence of Heat Treatment Temperature on Microstructure and Property of 00Crl3Ni5Mo2 Supermartensitic Stainless Steel, J. Iron. Steel Res. Int. 21 (2014) 364-368.

[11] J.A. Moreto, C.E.B. Marino, W.W. Bose Filho, L.A. Rocha, J.C.S. Fernandes, SVET, SKP and EIS study of the corrosion behaviour of high strength Al and Al–Li alloys used in aircraft fabrication, Corr. Sci. 84 (2014) 30-41.

[12] A. Pritzel dos Santos, S.M. Manhabosco, J.S. Rodrigues, L.F.P. Dick, Comparative study of the corrosion behavior of galvanized, galvannealed and Zn55Al coated interstitial free steels, Surf. Coat. Technol. 279 (2015) 150-160.

[13] S.M. Manhabosco, A.P. dos Santos, M.L. Marcolin, E.F. Pieretti, M.D.M. Neves, L.F.P. Dick, Localized corrosion of laser marked M340 martensitic stainless steel for biomedical applications studied by the scanning vibrating electrode technique under polarization, Electrochim. Acta 200 (2016) 189-196.

[14] E.F. Pieretti, S.M. Manhabosco, L.F.P. Dick, S. Hinder, I. Costa, Localized corrosion evaluation of the ASTM F139 stainless steel marked by laser using scanning vibrating electrode technique, X-ray photoelectron spectroscopy and Mott–Schottky techniques, Electrochim. Acta 124 (2014) 150-155.

[15] S.M. Manhabosco, R.J.C. Batista, S. Neves da Silva, L.F.P. Dick, Determination of current maps by svet of hot-dip galvanized steel under simultaneous straining, Electrochim. Acta 168 (2015) 89-96.

[16] J.C.B. Bertoncello, S.M. Manhabosco, L.F.P. Dick, Corrosion study of the friction stir lap joint of AA7050-T76511 on AA2024-T3 using the scanning vibrating electrode technique, Corr. Sci. 94 (2015) 359-363.

[17] R. A. Brand, Improving the validity of hyperfine field distributions from magnetic alloys: Part I: Unpolarized source. Nuclear Instruments and Methods in Physics Research Section B 1987, 28: 398-14.

[18] C. Lemoine, A. Fnidiki, F. Danoix, M. Hédin, J. Teillet, Mössbauer and atom probe studies on the ferrite decomposition in duplex stainless steels caused by the quenching rate. J. Phys. 1999, Condens. Matter. 11 1105. http://iopscience.iop.org/0953-8984/11/4/018.

[19] H. D. Solomon, L. M. Levinson, Mössbauer effect study of 475°C embrittlement of duplex and ferritic stainless steel. Acta Metall., 26 (1978) 429-42.

[20] T. J. Mesquita, E. Chauveau, M. Mantel, N. Bouvier, D. Koschel, Corrosion and metallurgical investigation of two supermartensitic stainless steels for oil and gas environments. Corros. Sci. 81 (2014) 152-161.

[21] V. Vignala, D. Baa, H. Zhanga, F. Herbsta, S. Le Manchetb, Influence of the grain orientation spread on the pitting corrosion resistance of duplex stainless steels using electron backscatter diffraction and critical pitting temperature test at the microscale. Corros. Sci. 68 (2013) 275-278.

[22] R. S. Dutta, R. Purandare, A. Lobo, S. K. Kulkarni, G. K. Dey, Microstructural aspects of the corrosion of alloy 800, Corros. Sci. 46 (2004) 2937–2953.

[23] Meng F., Wang J., Han E-H, Ke W., The role of TiN inclusions in stress corrosion crack initiation for Alloy 690TT in high-temperature and high-pressure water, Corros. Sci. 52 (2010) 927-932.

[24] D. H. Hur, J. H. Han, U. C. Lee, Y. S. Park, Microchemistry of Ti-carbonitrides and their role in the early stage of pit initiation of alloy 600, Corros. 62 (2006) 591-597.

[25] Y. Lian, J. Huang, J. Zhang, C. Zhang, W. Gao, C. Zhao, Effect of 0.2 and 0.5% Ti on the microstructure and mechanical properties of 13Cr supermartensitic stainless steel. J. Mater. Eng. and Perform. 24 (2015) 4253-4259.

[26] D. Carrouge, Transformations in Supermartensitic Stainless Steels, Thesis (PHD), Department of Materials Science and Metallurgy, University of Cambridge, 2002.

[27] P. D. Bilmes, M. Solari, C.L. Llorente, Characteristics and effects of austenite resulting from tempering of l3CrNiMo martensitic steel weld metals, Mater. Charact. 46 (4) (2001) 285-296.

[28] Sidney Siegel and N John Castellan. Nonparametric statistics for the behavioral sciences, 1988.

[29] C. L. Briant, A. M. Ritter, The effects of deformation induced martensite on the sensitization of austenitic stainless steels, Metall. Trans. A 11A (1980) 2009–17.

[30] C. L. Briant, A. M. Ritter, The effect of gold work on the sensitization of 304 stainless steel, Scripta. Met. 13 (1979) 177-181.

[31] K. Jha Abhay, D. Sivakumar, K. Sreekumar, M. C. Mittal, Role of transformed martensite in the cracking of stainless steel plumbing lines, Eng. Fail. Anal. 15 (2008) 1042–51.

[32] G. S. Frankel, Pitting Corrosion of Metals, J. Electrochem. Soc. 6 (1998) 2186-2198.

[33] P. Marcus, V. Maurice, H. H. Strehblow, Localized corrosion (pitting): A model of passivity breakdown including the role of the oxide layer nanostructure, Corros. Sci. 50 (2008) 2698-2704.

[34] Y. Tan, Understanding the effects of electrode inhomogeneity and electrochemical heterogeneity on pitting corrosion initiation on bare electrode surfaces, Corros. Sci. 53 (2011) 1845-1864.

[35] M. A. Baker, Castle J. E., The initiation of pitting corrosion of stainless steels at oxide inclusions, Corros. Sci. 33 (1992) 1295-1312.

[36] T. P. Hoar, The production and breakdown of the passivity of metals, Corros. Sci. 7 (1967) 341-355.

[37] N. Sato, An overview on the passivity of metals, Corros. Sci. 3 (1990)1-19.

[38] J. Soltis., Passivity breakdown, pit initiation and propagation of pits in metallic materials – Review, Corros. Sci. 90 (2015) 5-22.

PAPER 3: Electrochemical and electronic properties of passive film

formed on supermartensitic stainless steel in a chloride medium

Supermartensitic steel

EIE

Mott-Schottky
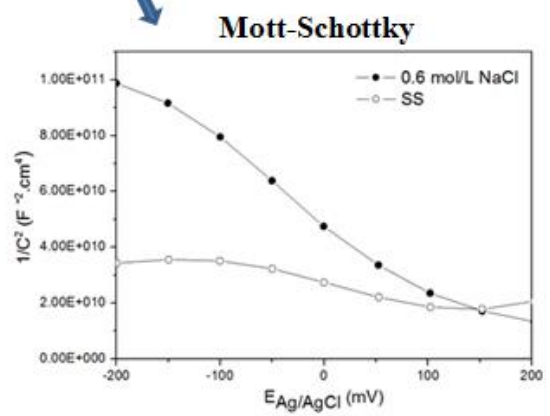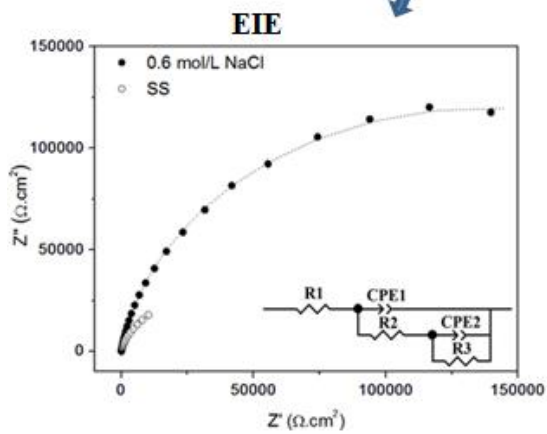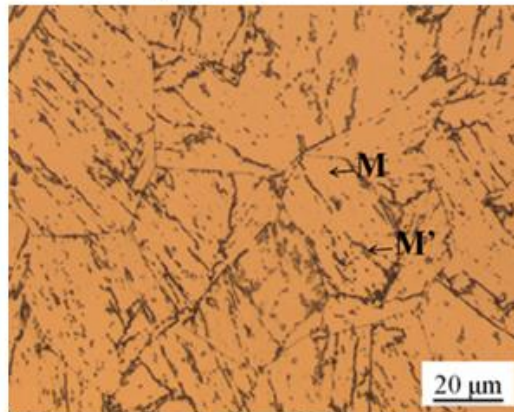
Abstract

In this study, the electrochemical behavior and the semiconducting properties of the passive film on a supermartensitic steel produced for application in the oil and gas industries as an alternative to the duplex steels was investigated in 0.6 mol/L NaCl and 2.1 mol/L NaCl, 0.005 mol/L sodium acetate, with pH 4.5 (adjusted by CH3COOH) aqueous solutions. For this evaluation, measurements of the open circuit potential, electrochemical impedance spectroscopy, cyclic polarization and Mott-Schottky analysis were performed. The steel samples were austenitized at $1000^{o}C$, water quenched, and tempered at $600^{o}C$ and $640^{o}C$ for 30 minutes. The 0.6 mol/L NaCl aqueous solution was the less aggressive electrolyte to the supermartensitic stainless steel (SMSS). The SMSS tempered at $600°C$ exhibited the highest corrosion resistance in two electrolytes. Furthermore, the capacitance study shows that the passive films formed on supermartensitic steel behave as p-type semiconductors below the flat band potential.

Introduction

The corrosion resistance of stainless steel is due to the presence of a protective oxide film formed on the surface and is associated with the semiconducting properties of the film [1, 7]. However, it is important to study the electronic properties of the passive films to understand the mechanisms behind passivity and localized corrosion.

Recently, increasing research of the electronic properties of the passive films formed on stainless steels has been an important contribution to the understanding of the protective behavior against corrosion of these alloys [3, 6, 12]. The passive films behave as extrinsic semiconductors due to the presence of defects when exposed to an aqueous solution. These defects can be electron acceptors in the case of p-type doping, or electron donors, resulting in n-type doping [3]. The passive film with a deficiency in metal ions or excess of cationic vacancies generally behaves as p-type, while a passive film with excess of anionic vacancies or interstitials cations behave as n-type semiconductor [4]. Fattah and Vafaeian [3] studied the electrochemical behavior of coarse-grained and fine-grained AISI 430 ferritic stainless steel in 0.1 M HNO_3 solution. Potentiodynamic polarization curves and electrochemical impedance spectroscopy (EIE) measurements showed that grain refinement operation offer better condition for forming the passive films [3]. Mott–Schottky analysis revealed that the passive films behave as n-type and p-type semiconductors and the calculated donor and acceptor densities were smaller for the refined grain, indicating that the passivation behavior improved with decreasing the grain size [3].

The aim of the present work is to study the electrochemical and electronic properties of passive films formed on supermartensitic stainless steels in a chloride environment.

Mott-Schottky analysis was used to study the eletronic properties of passive film. Moreover, cyclic voltammetry and Electrochemical Impedance Spectroscopy (EIS) were used to investigate the corrosion resistance of the supermartensitic stainless steel in 0.6 mol/L NaCl and 2.1 mol/L NaCl, 0.005 mol/L sodium acetate, with pH 4.5 (adjusted by CH3COOH) aqueous solutions.

Materials and Methods

The chemical composition of the investigate supermartensitic stainless steel is shown in Table 1. Supermartensitic steel was developed for application in oil and gas industry. The samples were extracted from seamless stainless steel tube water quenched after re-austenitizing at 1000°C for 30 min. In order to produce different microstructures, the samples were tempered at different temperatures and followed by air cooled as shown in Table 2. Vickers microhardness testing was performed in samples using a load of 2.94 N (300 gf) and the average hardness value of supermartensitic steel also is shown in Table 2.

Table 1: Chemical composition of the supermartensitic stainless steel from SENAI-CETEF/Itaúna.

Element	C	Cr	Ni	Mo	Si	Mn	P	S	N	Al	Ti
Content (wt%)	<0.01	12.2	5.63	1.86	0.21	0.52	0.023	0.004	0.026	0.015	0.17

Table 2: Sample identification and heat treatments conditions.

Sample identification	Heat treatments	Vickers Hardness (HV 300gf)
T (as-quenched)	1000°C 30 min, water quenched	275.43±2.36
T1	600°C 30 min, air cooled	274.57±10.22
T2	640°C 30 min, air cooled	260.77±9.43

The sample surface was subjected to a standard procedure to remove surface irregularities. The samples were polished with sandpaper grain size of 240, 320, 400, 600, 1200 mesh and with a 1/4 μm diamond suspension for metallographic characterization.

The microstructure of each sample was characterized by image analysis using Olympus optical microscopy after electrochemical attack in 10% (v/v) HNO_3 solution. The T1 and T2 samples was immersed for 120 s and attack using 1.5 V and the T sample was immersed for 60 s and attack using 1.5 V.

Cyclic polarization

Cyclic polarization testing was performed using a Autolab PGSTAT 100N potentiostat. A conventional three-electrode cell was used, the working electrodes being prepared from the supermartensitic stainless steel samples with an exposed surface of approximately 1 cm^2. The reference electrode was a Ag/AgCl (saturated KCl) and a Pt mesh was used as the counter electrode. The tests were performed at room temperature.

The open circuit potential (OCP) measurements was performed for 3600s in 0.6 mol/L NaCl and 2.1 mol/L NaCl, 0.005 mol/L sodium acetate, with pH 4.5 (adjusted by CH3COOH). The cyclic polarization curves were obtained at a fixed scan rate (1 mV/s) from −30 mV below the observed open circuit potential. The experiments stopped when the current reached 1mA/cm^2. The measurements were performed with three replicates.

Electrochemical impedance analysis

A conventional three-electrode cell was used, the working electrodes being prepared from the supermartensitic stainless steel samples with an exposed surface of approximately 1 cm^2. The reference electrode was a Ag/AgCl (saturated KCl and a Pt mesh was used as the counter electrode. The tests were performed at room temperature.

EIS was performed in 0.6 mol/L NaCl and 2.1 mol/L NaCl, 0.005 mol/L sodium acetate, with pH 4.5 (adjusted by CH3COOH) aqueous solutions. A Autolab PGSTAT 100N potentiostat applied sinusoidal signals in the frequency range of 10 kHz - 5 mHz with amplitude of 10 mV. Before the measurements, the open circuit potential in 0.6 mol/L NaCl and 2.1 mol/L NaCl, 0.005 mol/L sodium acetate, with pH 4.5 (adjusted by CH3COOH) was measured for 3600s. The acquired impedance spectra are presented as Nyquist plots and interpreted in terms of equivalent electrical circuits. All tests were performed in triplicate.

Mott–Schottky analysis

Mott–Schottky analysis was performed using a Autolab PGSTAT 100N potentiostat. A conventional three-electrode cell was used, the working electrodes were the

supermartensitic stainless steel samples with an exposed surface of approximately 1 cm^2. The reference electrode was a Ag/AgCl (saturated KCl) and a Pt mesh was used as the counter electrode. The tests were performed at room temperature. The Mott–Schottky measurements was performed in 0.6 mol/L NaCl and 2.1 mol/L NaCl, 0.005 mol/L sodium acetate, with pH 4.5 (adjusted by CH3COOH) aqueous solutions.

Mott–Schottky analysis was carried out on the passive films at a frequency of 1 kHz using a 10 mV sinusoidal signal and steps of 50 mV, in the anodic direction, from the initial potential of -0.2 V Ag/AgCl to the final potential of 0.2 V Ag/AgCl. All tests were performed in triplicate.

Results and discussion

Microstructure analysis

The microstructures of the supermartensitic stainless steel sample in the as- quenched condition and after tempering at 600°C and 640°C are shown in Fig. 1 (a, b), Fig. 1 (c, d), and Fig. 1 (e, f), respectively. In this figures it is possible to identify lath martensite (M) formed in these steels, and the prior austenite grains were subdivided into packets of laths. It is also possible to identify for all heat treated conditions orange coarse cuboidal TiN particles that form upon solidification of the steel as show in the Fig. 1.
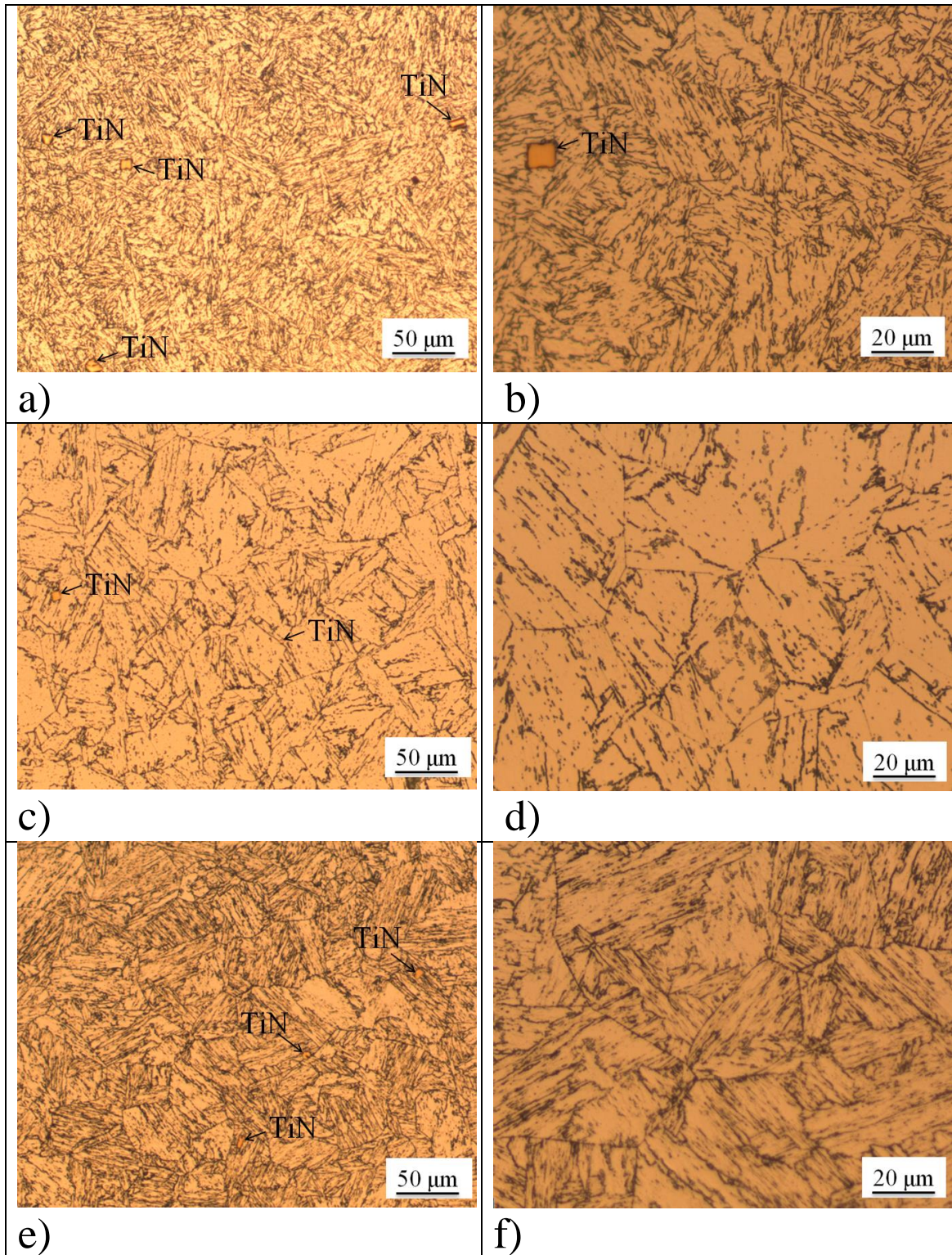
Fig. 1: Optical micrographs of the microstructure of the supermartensitic steel samples: a, b) as-quenched, c, d) after tempering for 30 min at 600°C and e, f) after tempering for 30 min at 640°C, respectively. TiN: titanium nitride.

Electrochemical impedance spectroscopy and Cyclic polarization

The impedance spectra (Figs. 3, 5, 7) for all supermartencitic steel samples show two time constants. The impedance data were analyzed using equivalent electrical circuits and using the ZView program (Scribner Assoc.) to fit the experimental data. The Fig. 2 shows the equivalent circuit used to model the experimental data. In the simulation of equivalent circuit, constant phase element (CPE) instead of pure capacitance element was used. The CPE impedance (Z_{CPE}) can be expressed by Eq. (1) [13-15]:

$$Z_{CPE} = \frac{1}{Q(j\omega)^n} \quad \text{Eq. (1)}$$

in which Q is the CPE magnitude ($\Omega^{-1}cm^{-2}s^n$), j^2=-1, n is the CPE exponent, and ω is the angular frequency. The magnitude of n is $0 \leq n \leq 1$ but is often close to 1 and the CPE behaves as a capacitor when n=1. The plot of the imaginary part of the impedance as a function of frequency gives a straight line with a slope equal to n [13-15].

The data in Figs. 3, 5, 7, 9 can be fitted well by the two time constant equivalent circuit represented in Fig. 2:
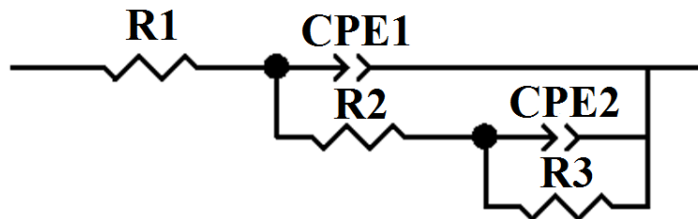
Fig. 2: Equivalent circuits used to model the experimental EIE data.

The fitted parameters are listed in Tables 3, 4. R1 is the electrolyte solution resistance, R2 is the resistance of the passive film, CPE1 corresponds to the pseudocapacitance of the film. R3 is a charge transfer resistance of the pitting hole, and CPE2 corresponds to a charge transfer capacitance of the pitting hole. Equivalent circuit model shows that passive film does not completely cover the metal surface, due to surface roughness and other reasons that can cause the dispersion effect.

The passive film is not a uniform layer, but a porous film of a semiconductor characteristic [16-18].

When simulating equivalent circuit, the polarization resistance (Rp) is represented by the R2 and R3, namely Rp＝ R2＋R3. Rp is the polarization resistance associated with the corrosive process between the metal and the solution, which occurs through the protective passive film. The diameter of the semi-circle impedance loop corresponds to Rp. The CPEs parameters obtained are in the range of usual values reported for passive film on stainless steel in chloride-containing solutions [19, 20].

The Nyquist and Bode diagrams of impedance modulus and of phase angle versus frequency of T, T1 and T2 samples in 0.6 mol/L NaCl and 2.1 mol/L NaCl, 0.005 mol/L sodium acetate, with pH 4.5 (adjusted with CH3COOH) aqueous solutions are shown in Figs. 3, 5, 7. Bode diagrams of impedance modulus (Fig. 3, 5, 7 (b)) showed the highest impedance of steel in solution of 0.6 mol/L of NaCl. Bode diagrams of phase angle versus frequency (Fig. 3, 5, 7 (c)) showed one large maximum peak indicating the possibility of the two time constants for all steel samples studied. Phase angles associated with maxima were 80° for both media, and the difference between the

steel behavior in the two electrolytes was not identified. The phase angle is close to the capacitive behavior, characterized by a phase angle of 90°.

The results of cyclic potentiodynamic polarization tests of T, T1 and T2 samples in media of in 0.6 mol/L NaCl and 2.1 mol/L NaCl, 0.005 mol/L sodium acetate, with pH 4.5 (adjusted by CH3COOH) aqueous solutions are shown in Fig. 4, Fig. 6 and Fig. 8, respectively. Table 5 shows the electrochemical parameters obtained using cyclic polarization tests.

Considering the corrosion resistance of the samples in the two electrolytes, the aqueous solution of 0.6 mol/L NaCl was less aggressive to the studied stainless samples. All samples showed a higher polarization resistance value, and higher breakdown potential values in a 0.6 mol/L NaCl aqueous solution than in 2.1 mol/L NaCl, 0.005 mol/L sodium acetate, with pH 4.5 (adjusted by CH3COOH).

Fig. 3: Nyquist diagrams (a), bode diagrams of impedance modulus (b) and phase angle

(c) of T sample in 0.6 mol/L NaCl and SS aqueous solutions. SS: 2.1 mol/L NaCl, 0.005

mol/L sodium acetate, with pH 4.5 (adjusted by CH3COOH). Dotted lines are fitting

results.

Fig. 4: Cyclic polarization tests of T sample in 0.6 mol/L NaCl and 2.1 mol/L NaCl,

0.005 mol/L sodium acetate, with pH 4.5 (adjusted by CH3COOH) aqueous solutions.
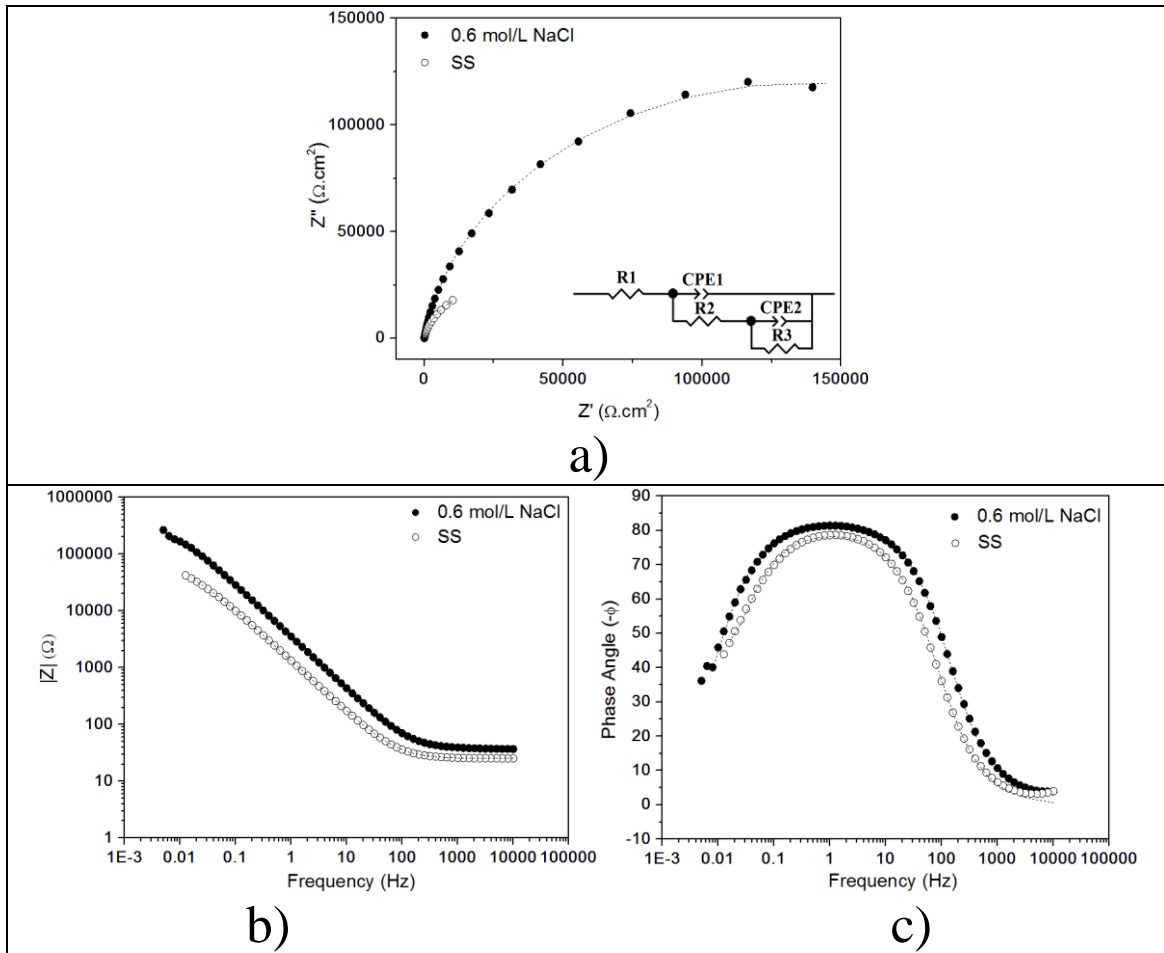
Fig. 5: Nyquist diagrams (a), bode diagrams of impedance modulus (b) and phase angle

(c) of T1 sample in 0.6 mol/L NaCl and SS aqueous solutions. SS: 2.1 mol/L NaCl,

0.005 mol/L sodium acetate, with pH 4.5 (adjusted by CH3COOH). Dotted lines are

fitting results.
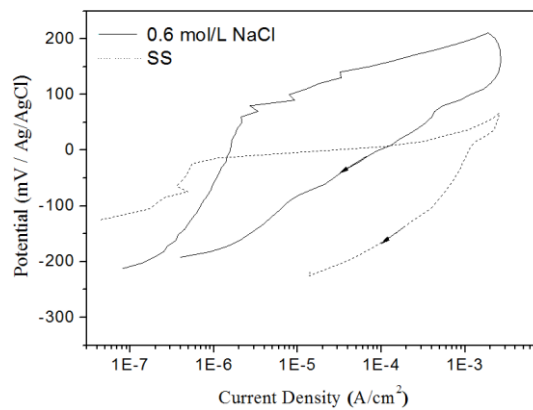
Fig. 6: Cyclic polarization tests of T1 sample in 0.6 mol/L NaCl and 2.1 mol/L NaCl,

0.005 mol/L sodium acetate, with pH 4.5 (adjusted by CH3COOH) aqueous solutions.

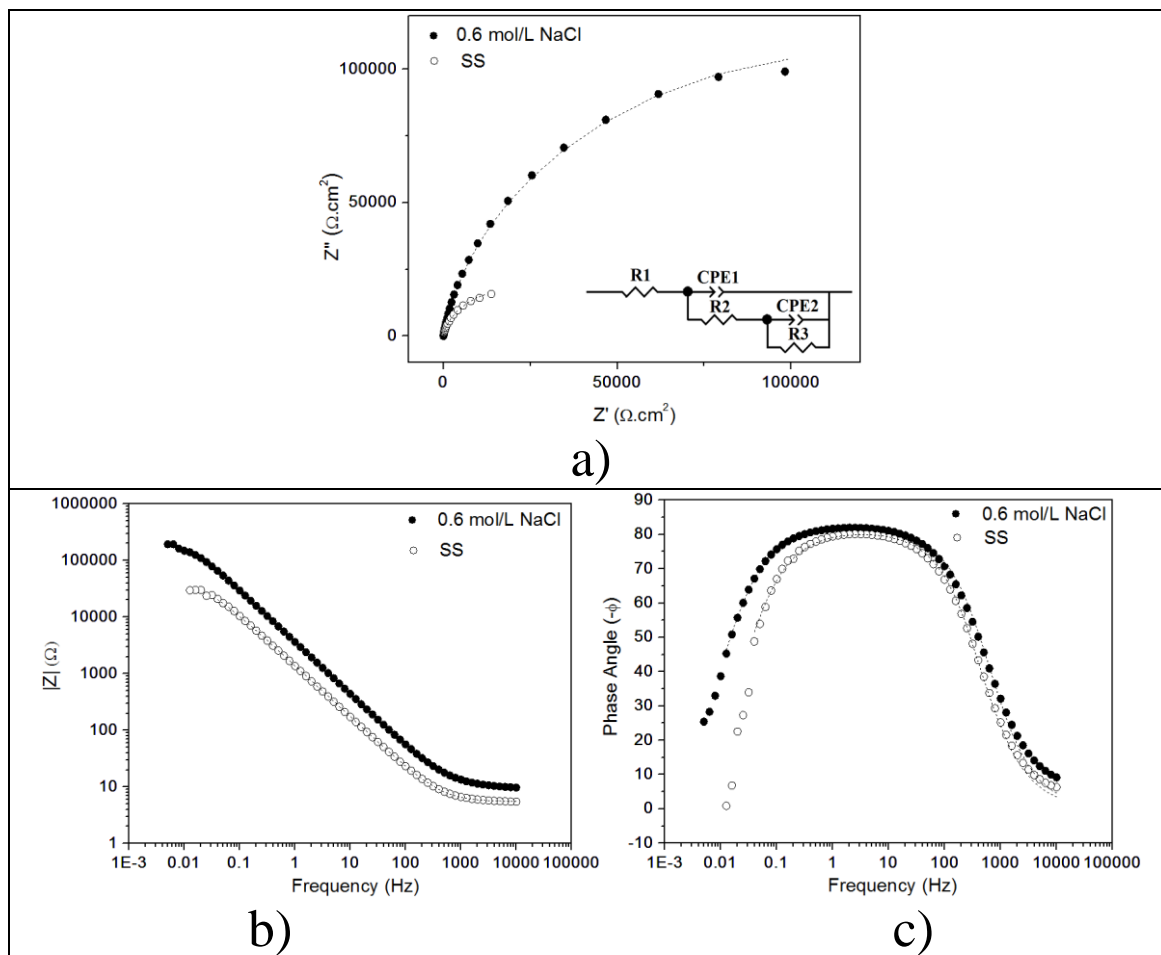**Fig. 7:** Nyquist diagrams (a), bode diagrams of impedance modulus (b) and phase angle (c) of T2 sample in 0.6 mol/L NaCl and SS aqueous solutions. SS: 2.1 mol/L NaCl, 0.005 mol/L sodium acetate, with pH 4.5 (adjusted by CH3COOH). Dotted lines are fitting results.
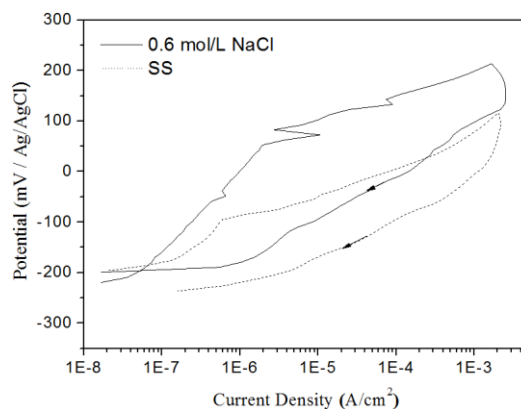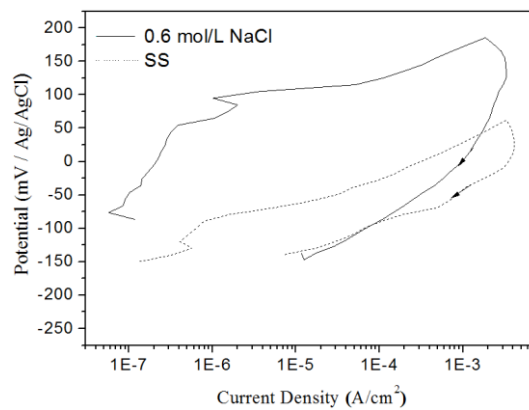

Fig. 8: Cyclic polarization tests of T2 sample in 0.6 mol/L NaCl and 2.1 mol/L NaCl, 0.005 mol/L sodium acetate, with pH 4.5 (adjusted by CH3COOH) aqueous solutions.
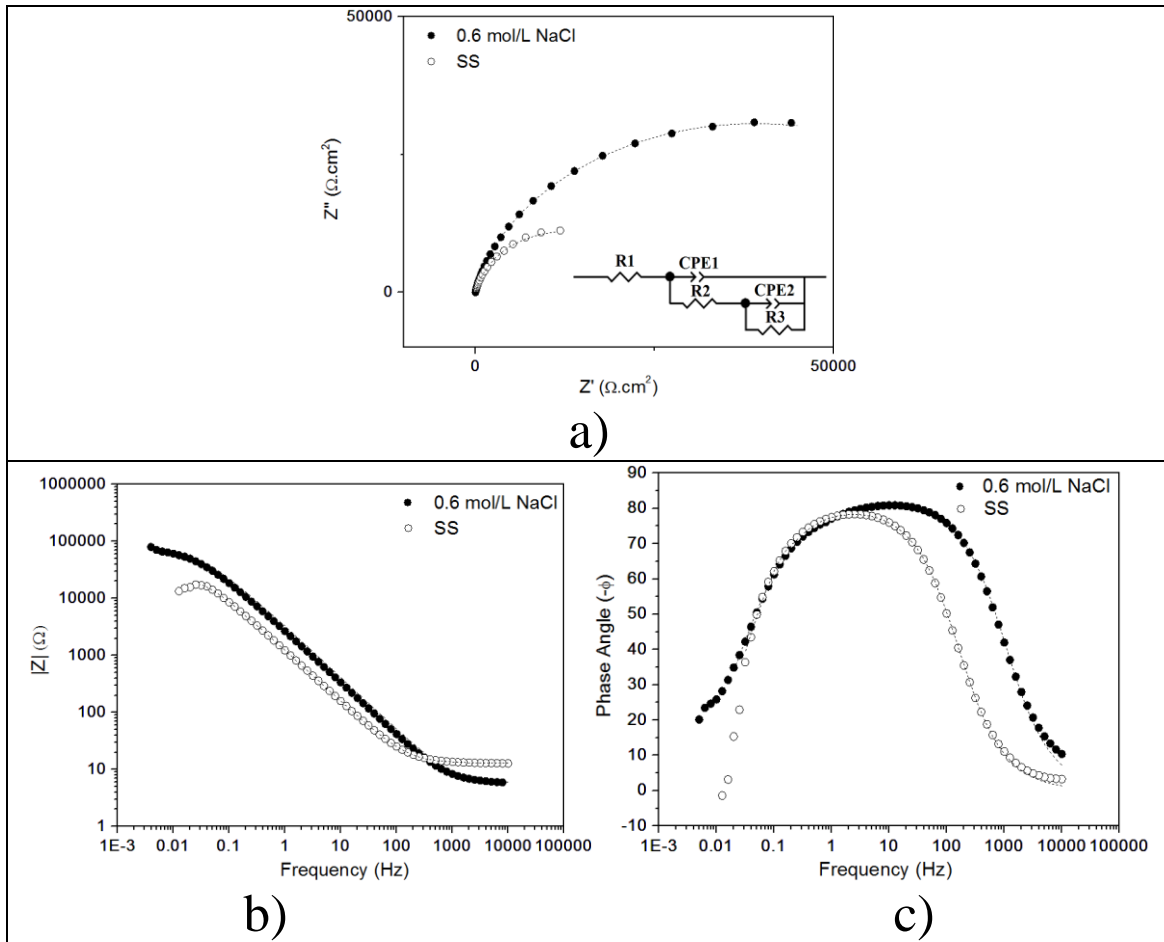
Table 3: Electrochemical parameters obtained using electrochemical impedance spectroscopy in 0.6 mol/L NaCl aqueous solution.

Samples	R1 ($\Omega . cm^2$)	R2 (k $\Omega . cm^2$)	R3 (k $\Omega . cm^2$)	CPE1 (F.cm-2)	CPE2 (F.cm-2)	Rp (k $\Omega . cm^2$)
T	21.97 ± 11.89	129.11 ± 3.18	117.45 ± 6.27	$(4.57\pm0.56)x10^{-5}$	$(3.15\pm3.15)x10^{-9}$	246.56 ± 3.10
T1	21.25 ± 14.25	0.06 ± 0.06	280.76 ± 5.60	$(2.54\pm1.02)x10^{-5}$	$(2.53\pm1.23)x10^{-5}$	280.76 ± 5.60
T2	7.02 ± 1.19	22.60 ± 7.83	56.05 ± 4.83	$(4.50\pm1.09)x10^{-5}$	$(2.17\pm0.34)x10^{-5}$	78.64 ± 3.00

Table 4: Electrochemical parameters obtained using electrochemical impedance spectroscopy in SS aqueous solution.

Samples	R1 ($\Omega . cm^2$)	R2 (k $\Omega . cm^2$)	R3 (k $\Omega . cm^2$)	CPE1 (F.cm-2)	CPE2 (F.cm-2)	Rp (k $\Omega . cm^2$)
T	5.97 ± 0.47	0.36 ± 0.24	42.22 ± 2.12	$(1.45\pm0.05)x10^{-4}$	$(3.59\pm3.48)x10^{-14}$	42.59 ± 2.36
T1	23.84 ± 1.53	59.78 ± 2.24	14.38 ± 0.50	$(1.47\pm0.01)x10^{-4}$	2.24 ± 0.03	74.16 ± 2.74
T2	13.22 ± 0.35	23.18 ± 2.15	3.68 ± 2.17	$(1.55\pm0.05)x10^{-4}$	$(6.95\pm0.35)x10^{-4}$	26.86 ± 0.02

SS: 2.1 mol/L NaCl, 0.005 mol/L sodium acetate, with pH 4.5 (adjusted by CH3COOH).

Table 5: Electrochemical parameters obtained using cyclic polarization in 0.6 mol/L NaCl and SS aqueous solutions.

Electrolyte	E_b mV(Ag/AgCl) T	E_b mV(Ag/AgCl) T1	E_b mV(Ag/AgCl) T2	Ipass A/cm^2 T	Ipass A/cm^2 T1	Ipass A/cm^2 T2
0.6 mol/L NaCl	99.23 ± 21.59	94.84 ± 7.36	102.37 ± 9.02	$6.27.10^{-7}$	$9.61.10^{-7}$	$2.35.10^{-7}$
SS	-108.85 ± 24.31	15.20 ± 5.08	-89.15 ± 22.09	$3.68.10^{-7}$	$3.76.10^{-7}$	$5.80.10^{-7}$

SS: 2.1 mol/L NaCl, 0.005 mol/L sodium acetate, with pH 4.5 (adjusted by CH3COOH).

Comparing the all samples in both media (Fig. 9), the T2 sample showed lower values of polarization resistance and the T1 sample showed the highest values of polarization resistance in the two electrolytes. In the SS electrolyte, according to the Tables 3, 4, all samples showed Rp values of a same magnitude order. But in the 0.6 mol/L NaCl electrolyte the T2 sample showed Rp value one magnitude order lower than the others samples. The polarization resistance (Rp) values from EIS tests are summarized in Fig. 11.

Fig. 10 shows the cyclic polarization curves obtained for all supermartensitic steel samples in the two electrolytes. The OCP values and breakdown potentials (Eb) are summarized in Fig. 12. Considering the polarization results, all cyclic polarization curves of the supermartensitic steel samples in both electrolytes exhibits spontaneous passivity above the OCP followed by a breakdown potential at which point the current increases rapidly. Upon reversal of the scan direction, each curve also shows a large positive hysteresis loop, with repassivation occurring near or even below the original OCP, indicating a severity of localized corrosion attack. The existence of a large hysteresis loop and low repassivation potential indicated that pit repassivation was difficult and that these materials have a high likelihood of forming pits during long time exposure to the solution containing chloride. All samples showed a similar value of passivation current density for the two electrolytes. In general, the OCP values for all sample were approximately -150 mV (Ag/AgCl) in both electrolytes (Fig. 12).

A similar corrosion resistance of all samples in 0.6 mol/L NaCl electrolyte was observed, according to the polarization results (Table 5). But in the 2.1 mol/L NaCl, 0.005 mol/L sodium acetate, with pH 4.5 electrolyte, the T1 sample showed a high

value of breakdown potential, indicating a superior localized corrosion resistance. These results are consistent with EIS measurements that revealed high values of polarization resistance (Rp) for T1 sample. Pitting of stainless steels is always associated with the breakdown of the passive film. The protective role of the passive film depends on its composition and structure, so it is expected that the changes in microstructure and composition due to heat treatment will affect the pitting corrosion behavior. After cyclic polarization testing, the localized corrosion morphology was found in all cases to be globular pits in both electrolytes (Fig. 13). No significant difference in microstructure was detected among the steel samples austenitized and water quenched, and tempered at $600^{o}C$ and at $640^{o}C$ and air cooled. However, in a previous work, the sample tempered at $600^{o}C$ and air cooled showed the smallest grain size, evaluated by using EBSD.
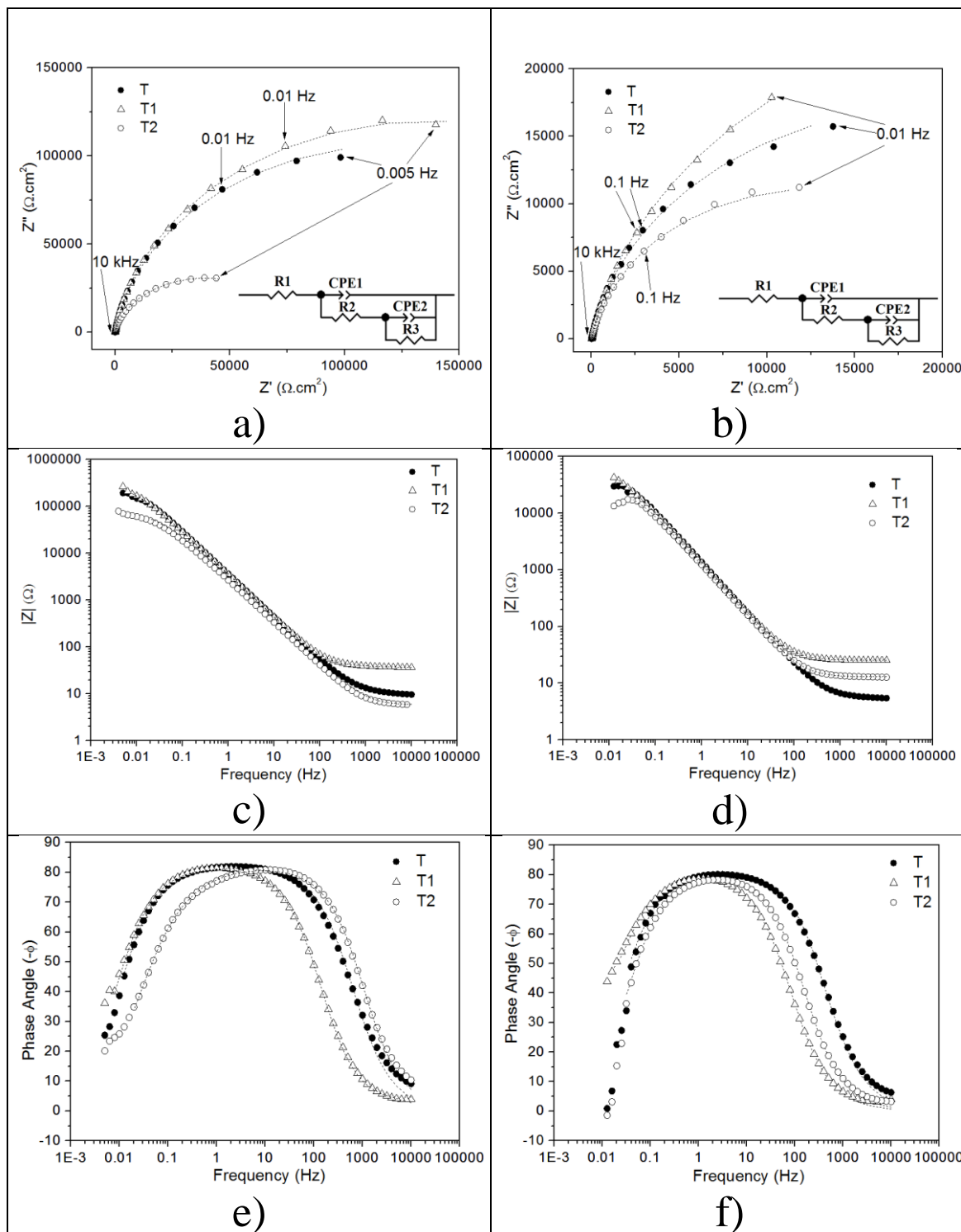
Fig. 9: Nyquist diagrams (a, b), bode diagrams of impedance modulus (c, d) and phase

angle (e, f) of T, T1 and T2 samples in 0.6 mol/L NaCl and 2.1 mol/L NaCl, 0.005

mol/L sodium acetate, with pH 4.5 (adjusted by CH3COOH) aqueous solutions,

respectively. Dotted lines are fitting results.
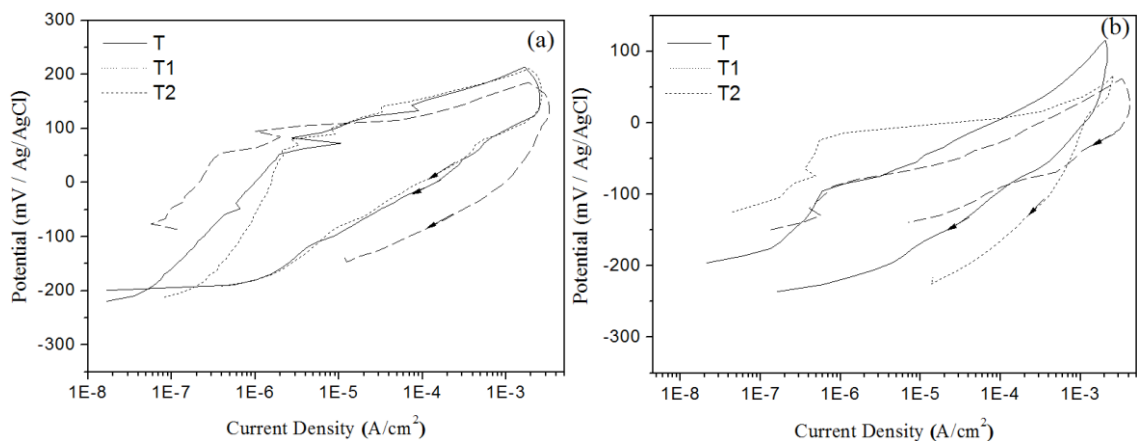
Fig. 10: Cyclic polarization tests of T, T1 and T2 samples in (a) 0.6 mol/L NaCl and

(b) 2.1 mol/L NaCl, 0.005 mol/L sodium acetate, with pH 4.5 (adjusted by CH3COOH)

aqueous solutions.

Fig. 11: Rp values of EIS experimental data for T, T1 and T2 samples in 0.6 mol/L

NaCl and SS aqueous solutions. SS: 2.1 mol/L NaCl, 0.005 mol/L sodium acetate, with

pH 4.5 (adjusted by CH3COOH).

124

Fig. 12: Eb and OCP values of cyclic polarization experimental data for T T1 and T2 samples in 0.6 mol/L NaCl and SS aqueous solutions. SS: 2.1 mol/L NaCl, 0.005 mol/L sodium acetate, with pH 4.5 (adjusted by CH3COOH).
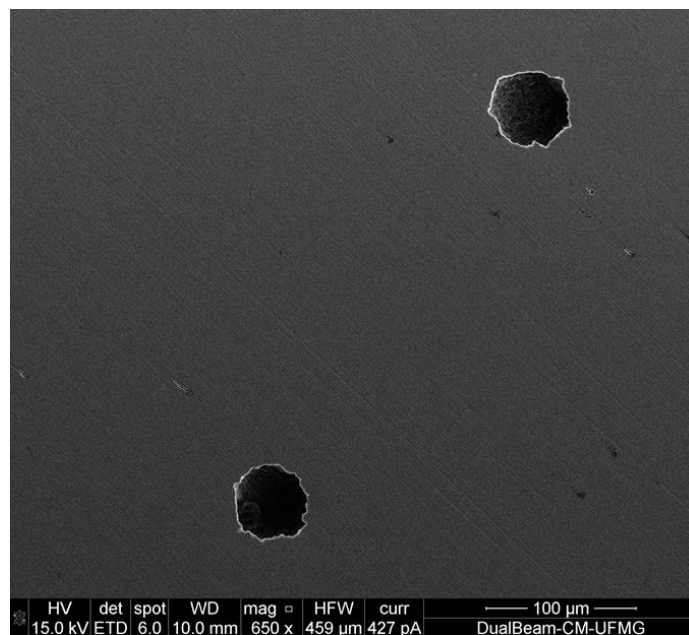
Fig. 13: Pit morphology for T 2 sample. Similar results were obtained for the others samples in samples in 0.6 mol/L NaCl and 2.1 mol/L NaCl, 0.005 mol/L sodium acetate, with pH 4.5 (adjusted by CH3COOH) aqueous solutions.

Mott–Schottky analysis

It has been proved in the literature that the corrosion resistance, film breakdown and pit initiation of stainless steels and passive metals and alloys are connected with the semiconducting properties of the passive films [1, 2]. Consequently, it is very important to study the electronic properties of the passive films to understand the electrochemical corrosion behavior.

The presence of point defects in passive films makes them behave as extrinsic semiconductors when exposed to an aqueous solution [3]. According the point defect model (PDM) these point defects in the passive film are cation vacancies, oxygen vacancies, and cation interstitials. Based on PDM, cation vacancies are electron acceptors in the case of p-type doping, while oxygen vacancies and metal interstitials are electron donors, resulting in n-type doping [3, 4].

The semiconducting properties of the passive film can be studied by Mott- Schottky analysis. According to the Mott–Schottky theory, the space charge capacitances of p-type semiconductors were given by Eq. (2) [4-6]:

$$\frac{1}{C^2} = -\frac{2}{\varepsilon\varepsilon_0 eN_A}\left(E_{FB} - E + \frac{kT}{e}\right) \quad \text{Eq. (2)}$$

where C is the capacitance of the film/electrolyte interface, e is the electron charge (1.6029*10^{-19} C), N_A is the density of electron acceptors for doping an p-type semiconductor (cm^{-3}), ε is the dielectric constant of the passive film, (usually taken as 15.6 for stainless steel [3]), ε_0 is denotes the vacuum permittivity (8.8542*10^{-14} F/cm),

E is the applied potential, k is the Boltzmann constant, T is the absolute temperature and E_{FB} is the flat-band potential. The flat band potential can be determined from the extrapolation of the linear portion to $C^{-2} = 0$ [3].

Fig. 14 shows the Mott–Schottky plots of the passive films formed on T1 sample in 0.6 mol/L NaCl and 2.1 mol/L NaCl, 0.005 mol/L sodium acetate, with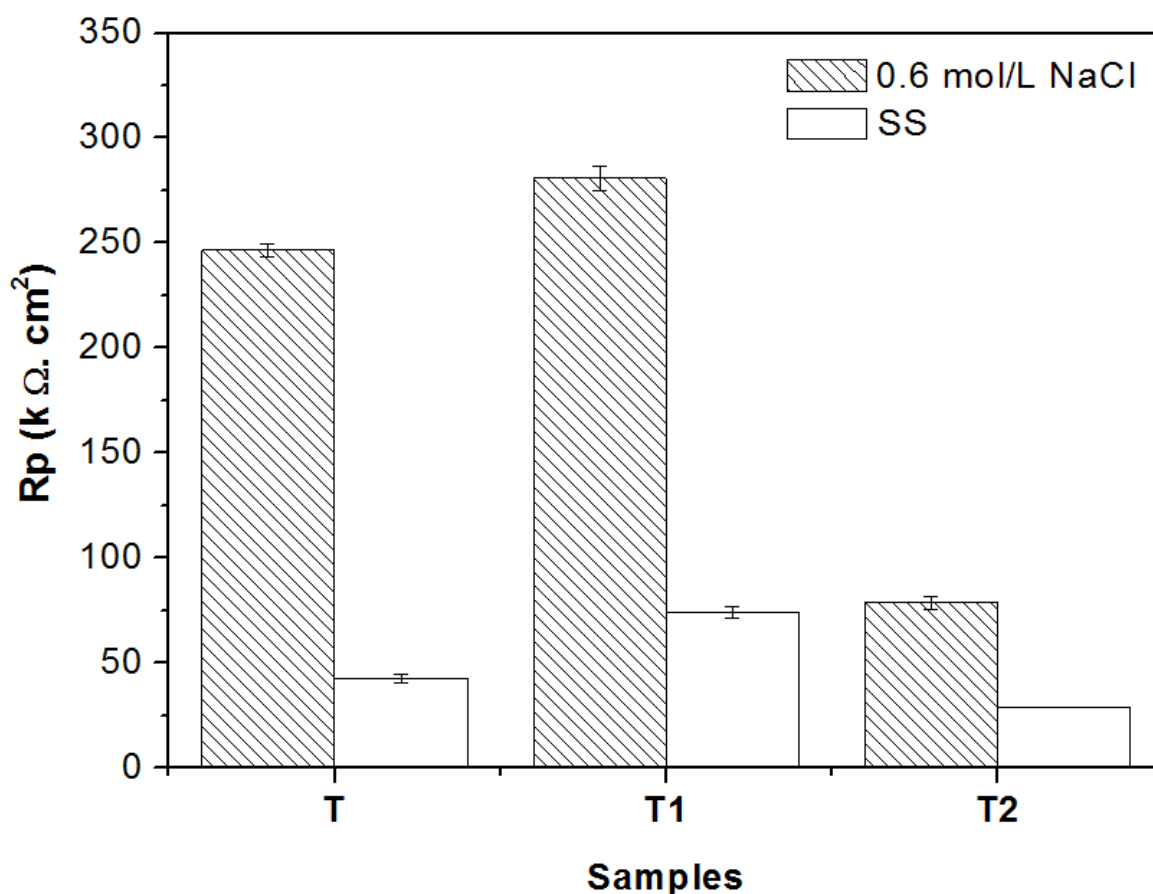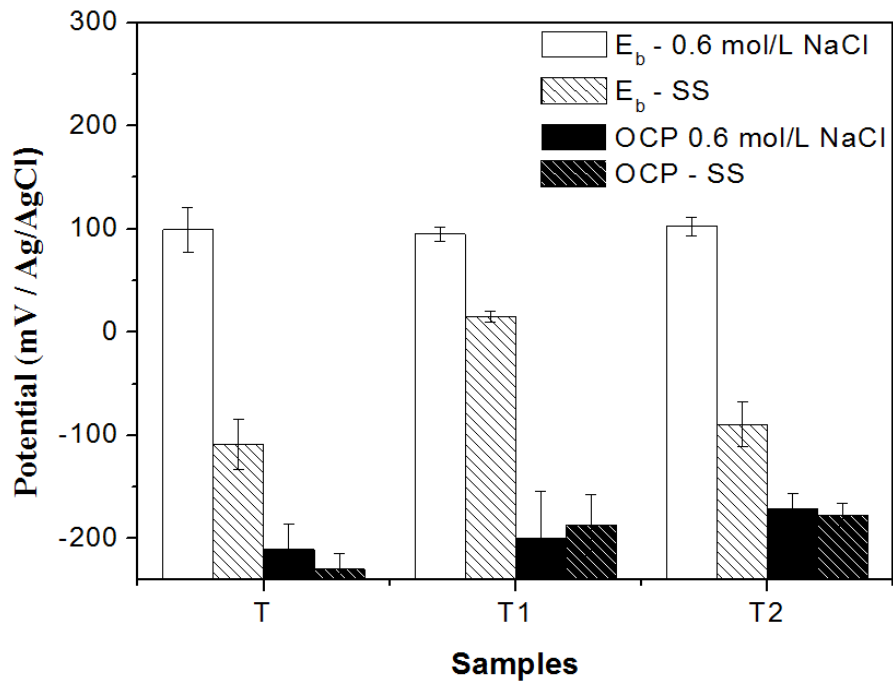 pH 4.5 (adjusted by CH3COOH) aqueous solutions. Similar response was exhibited for the passive films (Fig. 14) in all supermartensitic stainless steel samples. The negative slopes observed in C^{2-} versus E plot are attributed of a p-type semiconductor behavior. These behaviors are in reasonable agreement with the results obtained in other works in chloride solutions and is related to the semiconducting properties of the chromium oxide present in the passive films [2, 7]. According Virtanen et al. [8] the chromium vacancies or excess oxygen can be correlated to this p-type semiconductor behavior of chromium oxide in passive films. The p-type semiconducting behavior can be correlated to an increase in the conductivity of the passive film due to the solid state oxidation of Cr^{3+} to Cr^{6+}. Moreover, this behavior can be explained by the generation of cation vacancies (electronic acceptors and p-type dopants) at the passive film/solution interface [3].
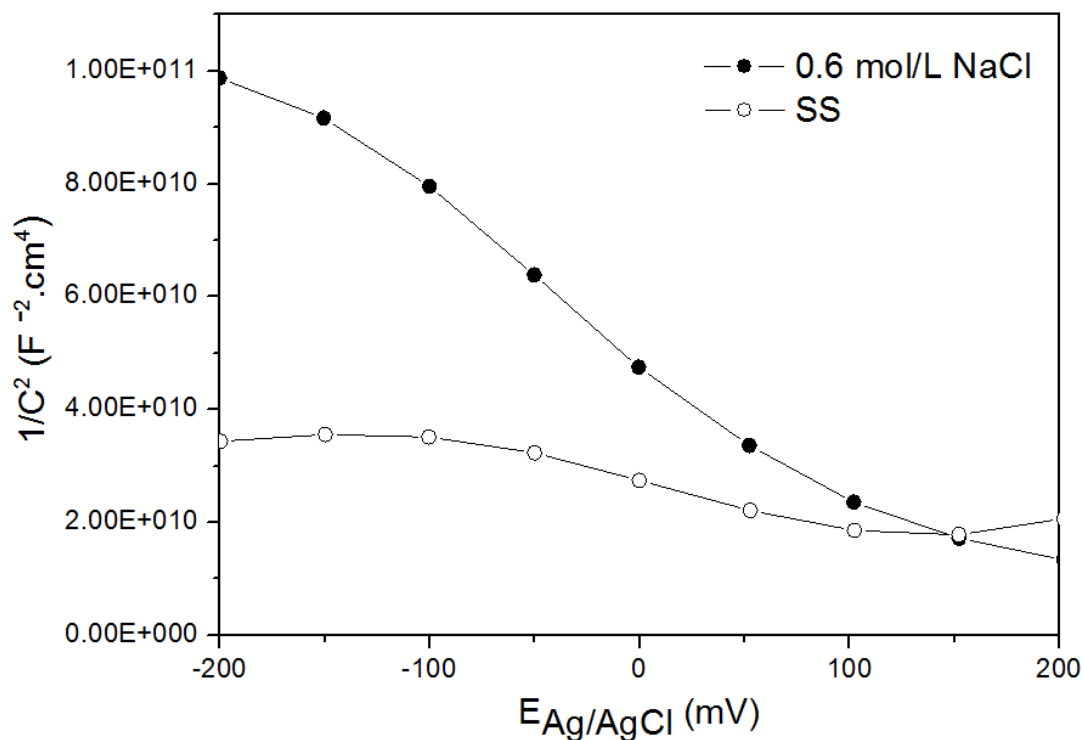
Fig. 14: Mott-Schottky plots of T1 sample. Similar results were obtained for the others samples in samples in 0.6 mol/L NaCl and SS aqueous solutions. SS: 2.1 mol/L NaCl, 0.005 mol/L sodium acetate, with pH 4.5 (adjusted by CH3COOH).

According to Bensalah et al. [6], the type of defects, i.e. donors or acceptors, depends on the composition of the oxide film. Thus a Cr-rich layer, Cr_2O_3 or $FeCr_2O_4$, but also MoO_2 and NiO exhibit p-type semiconductor behavior, while a Fe rich layer, Fe_2O_3, MoO_3, and Fe(OOH) exhibit n-type behavior. Therefore the semi conductive properties of the passive film depend on the contribution of each oxide and the concentration of the cationic or anionic vacancies inside these oxides.

According to Eq. 1, the acceptor densities have been determined from the negative slopes in the main passive region. Table 1 shows the calculated acceptor densities for the passive films formed in T1 sample in 0.6 mol/L NaCl and 2.1 mol/L NaCl, 0.005 mol/L sodium acetate, with pH 4.5 (adjusted by CH3COOH) aqueous solutions. The

order of magnitude is 10^{22} cm^{-3} and is comparable to those reported for other stainless steels in chloride solutions [2, 7, 9]. The high doping densities indicated the characteristic of highly disordered passive films. According Macdonald et al. [10], the disordered of the passive film resulted from the point defect that doped in the film, such as oxygen vacancies and metal cation vacancies. Consequently, the lower doing densities may be associated with more stable and compact passive films [7, 9].

The acceptor densities of the passive film formed on the T1 samples in 2.1 mol/L NaCl, 0.005 mol/L sodium acetate, with pH 4.5 (adjusted by CH3COOH) aqueous solution were higher than those formed in 0.6 mol/L NaCl aqueous solution, reflecting the better passive behavior of the T1 sample in 0.6 mol/L NaCl aqueous solution. Heuer et al. [11] reported that the Cl$^-$ ions were incorporated into the Cr_2O_3-rich passive film and Cl$^-$ dependent defect structures deeply inside the passive film were formed. The increase of the acceptor densities can be explained by the hypothesis about oxygen substituted by chloride ion, i. e., the valence of anion partly changed from - 2 to - 1, equivalent to the reduction of charge carriers based on the charge balance in the film, and cause capacitance to decrease. The decrease of donor densities can be explained due a quantity of cation vacancies are emerged due to cation extraction by induction reaction of chloride ion in the growth process of the passive film in chloride containing solution [2]. These results are consistent with EIS and cyclic polarization measurements that revealed an increase of the polarization resistance (Rp) and the pitting potential respectively, for the T1 sample in 0.6 mol/L aqueous solution than in 2.1 mol/L NaCl, 0.005 mol/L sodium acetate, with pH 4.5 (adjusted by CH3COOH).

Furthermore, for an p-type semiconductor, the thickness of the space charge layer W can also be calculated by Eq. (3) [9, 21]:

$$W = \left[\frac{2\varepsilon\varepsilon_0}{eN_A}\left(E - E_{FB} - \frac{kT}{e}\right)\right]^{1/2} \quad \text{Eq. (3)}$$

Table 6 shows the thickness of the space charge layer for the passive films in in 0.6 mol/L NaCl and SS aqueous solutions. A thick space charge layer indicated a thick passive film, which leads to higher resistance to pitting corrosion [21]. In addition, the space charge layer is also an effective barrier to slow down the carriers flow (i. e., electrons and holes) from semiconductor to electrolyte. As shown in Table 6, in the region of p-type semiconductor, the space charge layer of T1 sample in 0.6 mol/L NaCl aqueous solution was thicker than in 2.1 mol/L NaCl, 0.005 mol/L sodium acetate, with pH 4.5 (adjusted by CH3COOH), indicating more protective film.

Table 6: Calculated values of doping densities and thicknesses of space charge layers of T1 sample in 0.6 mol/L NaCl and SS aqueous solutions.

Solution	Acceptor densities (N_A / 10^{22}. cm^{-3})	W / nm
0.6 mol/L NaCl	2.81±0.43	0.24
SS	8.24±1.18	0.15

SS: 2.1 mol/L NaCl, 0.005 mol/L sodium acetate, with pH 4.5 (adjusted by CH3COOH).

Conclusions

The supermartensitic steel tempered at 600^oC and air cooled showed the highest corrosion resistance in electrolytes containing chloride and in acidic electrolyte containing chlorides and acetate.

Comparing values of Rp, E_b and acceptor densities in the two electrolytes, the supermartensitic steel in 0.6 mol/L NaCl aqueous solution showed higher values of polarization resistance, high values of breakdown potential and lower values of acceptor density than in 2.1 mol/L NaCl, 0.005 mol/L sodium acetate, with pH 4.5 (adjusted by CH3COOH).

EIS analysis showed the porous structure of passive film.

The capacitance study shows that the passive films formed on supermartensitic steel behave as and p-type semiconductors below the flat band potential.

Acknowledgments

References

[1] N.E. Hakiki, Comparative study of structural and semiconducting properties of

passive films and thermally grown oxides on AISI 304 stainless steel, Corros. Sci. 53 (2011) 2688.

[2] J. Soltis, Passivity breakdown, pit initiation and propagation of pits in metallic materials – Review, Corros. Sci. 90 (2015) 5.

[3] A. Fattah-alhosseini, S. Vafaeian, Comparison of electrochemical behavior between coarse-grained and fine-grained AISI 430 ferritic stainless steel by Mott–Schottky analysis and EIS measurements, J. Alloys Compd. 639 (2015) 301.

[4] E.F. Pieretti, S.M. Manhabosco, L.F.P. Dick, S. Hinder, I. Costa, Localized corrosion evaluation of the ASTM F139 stainless steel marked by laser using scanning vibrating electrode technique, X-ray photoelectron spectroscopy and Mott–Schottky techniques, Electrochim. Acta 124 (2014) 150.

[5] A. Di Paola, Photoelectrochemical study of the amorphous-WO_3-semiconductor–electrolyte junction, Electrochim. Acta 34 (1989) 203.

[6] M. BenSalah, R. Sabot, E. Triki, L. Dhouibi, Ph. Refait, M. Jeannin, Passivity of Sanicro28 (UNS N-08028) stainless steel in polluted phosphoric acid at different temperatures studied by electrochemical impedance spectroscopy and Mott–Schottky analysis, Corros. Sci. 86 (2014) 61.

[7] X. Han, J. Li, K. Zhao, W. Zhang, J. Su, Effect of Chloride on Semiconducting Properties of Passive Films Formed on Supermartensitic Stainless Steel in NaHCO3 Solution, J. Iron. Steel Res. Int. 20 (2013) 74–79.

[8] S. Virtanen, P. Schmuki, H. Bohni, P. Vuoristo, T. Mantyla, Artificial Cr- and Fe-oxide passive layers prepared by sputter deposition, J. Electrochem. Soc. 142 (1995) 3067–3072.

[9] D.N. Zou, R. Liu, J. Li, W. Zhang, D. Wang, Y. Han, Corrosion Resistance and Semiconducting Properties of Passive Films Formed on 00Cr13Ni5Mo2

Supermartensitic Stainless Steel in Cl⁻ Environment, J. Iron. Steel Res. Int. 21 (2014) 630-636.

[10] D.D. MacDonald, The Point Defect Model for the Passive State, Journal of Electrochemical Society, 139 (1992) 3434-3449.

[11] Heuer A H, Kahn H, Natishan P M. Electrostrictive Stresses and Breakdown of Thin Passive Films on Stainless Steel, J. Electrochim. Acta 58 (2011) 157.

[12] I.M. Gadala, A. Alfantazi, A study of X100 pipeline steel passivation in mildly alkaline bicarbonate solutions using electrochemical impedance spectroscopy under potentiodynamic conditions and Mott-Schottky, Appl. Surf. Sci. 357 (2015) 356.

[13] J.-B. Jorcin, M. E. Orazem, N. Pébère, CPE analysis by local electrochemical impedance spectroscopy, B. Tribollet, Electrochim. Acta 51 (2006) 1473.

 [14] M.E. Orazem, B. Tribollet, Electrochemical impedance spectroscopy, Hoboken, Wiley, New Jersey 2008.

[15] S. Belkaid, M.A. Ladjouzi, S. Hamdani, Effect of biofilm on naval steel corrosion in natural seawater. Journal of Solid State Electrochemistry., J. Solid State Electrochem. 15 (2011) 525.

[16] A.K. Iversen, Stainless steels in bipolar plates - Surface resistive properties of corrosion resistant steel grades during current loads, Corros. Sci. 48 (2006) 1036-1058.

[17] Z.J. Zheng, Y. Gao, Y. Gui, M. Zhu, Studying the fine microstructure of the passive film on nanocrystalline 304 stainless steel by EIS, XPS, and AFM, J. Solid State Electr. 18 (2014) 2201-2210.

[18] L.A.S. Ries, M. Da Cunha Belo, M.G.S. Ferreira, I.L. Muller, Chemical composition and electronic structure of passive films formed on Alloy 600 in acidic solution, Corros. Sci. 50 (2008) 676-686.

[19] M. Hoseinpoor, M. Momeni, M.H. Moayed, A. Davoodi, EIS assessment of critical pitting temperature of 2205 duplex stainless steel in acidified ferric chloride solution, Corros. Sci. 80 (2014) 197.

[20] M. Azzi, M. Benkahoul, J.E. Klemberg-Sapieha, L. Martinu, Corrosion and mechanical properties of duplex-treated 301 stainless steel, Surf. Coat. Technol. 205 (2010) 1557.

[21] J.B. Lee, S.W. Kim, Semiconducting properties of passive films formed on Fe-Cr alloys using capacitance measurements and cyclic voltammetry techniques, Mater. Chem. Phys. 104(2007) 98-104.

CHAPTER 6 - Final Considerations and Suggestions for future studies

Final Considerations

Supermatensitic stainless steel samples austenitized at 1000°C, water quenched, and tempered at 600°C and 640°C for 30 minutes, were received to studied the effect of the retained austenite on corrosion and tribocorrosion behavior but the amount of retained austenite was similar for all heat treated conditions.

A tribocorrosion setup was configured in order to study the triboelectrochemical behavior of supermartensitic steel. In this setup, the tribological contact was comprised a pin (vertical) in contact with a ball joint connected to sample, which underwent oscillatory linear motion. The configuration allowed synchronizing data of corrosion and tribology. The open circuit potential of supermartensitic steel in a saline solution is shifted to a lower value due to wear. The passivation current density increased as the abrasive particle size decreased. There is a trend to increase the breakdown potential as the particle size decreases. Different shapes of pits were observed after polarization measurements under corrosion and under tribocorrosion conditions. The pit size on the steel surface submitting to a tribocorrosion mechanism was smaller and the pit concentration was higher than in the corrosion condition. The smallest abrasive particles (10-20 μm) promoted the highest pit growth inhibition. The scars produced after testing indicating that three-body abrasion is the dominant wear mechanism. The friction coefficient of supermartensitic steel was similar in the passive and transpassive regions. The breakdown potential occurred after 53 wear cycles. Higher values of friction coefficient were obtained by using diamond particles of smaller sizes due to a higher contact area inside the wear track, compared to the friction coefficient values produced by diamond particles of larger sizes.

A microstructural and electrochemical analyses of SMSS submitted to austenitizing at 1000°C, water quenching, and tempering at 600°C and at 640°C and air cooled were performed. The techiniques used were Mössbauer spectroscopy, SEM and OM, EDS, XRD, EDSD, SVET and cyclic polarization. Coarse cuboidal TiN particles were identified on the steel surfaces of all samples. The TiN inclusions showed microvoids and a nucleous containing magnesium, aluminum and calcium oxides. Mössbauer analysis identified 0.7, 0.5 and 0.9% of retained austenite in SMSS samples as-quenched and tempered at 600°C and 640°C, respectively. The sample tempered at 600°C showed the lowest grain size, evaluated by using EBSD technique, and the highest localized corrosion resistance in a saline medium. The SMSS tempered at 600°C showed the highest breakdown and repassivation potentials among the samples studied. The SMSS sample tempered at 640°C showed no electrochemical activity after 3600s of immersion in a saline solution by using a SVET technique, but after 86400s, a pit was detected. SVET analysis showed the association of a localized corrosion sites with the TiN inclusion on the steel surface.

The supermartensitic steel tempered at 600°C and air cooled showed the highest corrosion resistance in electrolytes containing chloride and in acidic electrolyte containing chloride and acetate. Comparing values of Rp, E$_b$ and acceptor densities in the two electrolytes, the supermartensitic steel in a 0.6 mol/L NaCl aqueous solution showed higher values of polarization resistance, high values of breakdown potential and lower values of acceptor density than in 2.1 mol/L NaCl, 0.005 mol/L sodium acetate, with pH 4.5 (adjusted by CH3COOH). EIS analysis showed the porous structure of passive film. The capacitance study shows that the passive films formed on

supermartensitic steel behave as and p-type semiconductors below the flat band potential.

Suggestions for future studies

Perform steel surface characterization using transmission electron microscopy (TEM) to check the presence of other inclusions and cracks in the steel samples;

Evaluate the effect of texture on corrosion through the construction of the pole figures using EBSD results;

To perform the analyses of SVET in a less measuring window (active area) to observed the variation of the current on the TiN inclusion during the time.

To perform the XPS analysis on the steel surface to evaluate the composition of the passive film;

To perform Mott-Schottky analysis in different electrolytes that enhances the passive behavior.